arXiv:2311.07512v2 [astro-ph.CO] 8 Feb 2024

GALAXY CLUSTERS DISCOVERED VIA THE THERMAL SUNYAEV-ZEL'DOVICH EFFECT IN THE 500-SQUARE-DEGREE SPTPOL SURVEY

L. E. BLEEM[1,2], M. KLEIN[3,4], T. M. C. ABBOTT[5], P. A. R. ADE[6], M. AGUENA[7], O. ALVES[8], A. J. ANDERSON[9], F. ANDRADE-OLIVEIRA[8], B. ANSARINEJAD[10], M. ARCHIPLEY[11,12], M. L. N. ASHBY[13], J. E. AUSTERMANN[14,15], D. BACON[16], J. A. BEALL[14], A. N. BENDER[1,2,17], B. A. BENSON[9,2,17], F. BIANCHINI[18,19,20], S. BOCQUET[3], D. BROOKS[21], D. L. BURKE[18,20], M. CALZADILLA[22], J. E. CARLSTROM[2,23,1,17,24], A. CARNERO ROSELL[25,7,26], J. CARRETERO[27], C. L. CHANG[2,1,17], P. CHAUBAL[10], H. C. CHIANG[28,29], T-L. CHOU[2,23], R. CITRON[30], C. CORBETT MORAN[31], M. COSTANZI[32,33,34], T. M. CRAWFORD[2,17], A. T. CRITES[35], L. N. DA COSTA[7], T. DE HAAN[36,37], J. DE VICENTE[38], S. DESAI[39], M. A. DOBBS[28,40], P. DOEL[21], W. EVERETT[41], I. FERRERO[42], B. FLAUGHER[9], B. FLOYD[43], D. FRIEDEL[12], J. FRIEMAN[9,2], J. GALLICCHIO[2,44], J. GARC'IA-BELLIDO[45], M. GATTI[46], E. M. GEORGE[47], G. GIANNINI[27,2], S. GRANDIS[48], D. GRUEN[3], R. A. GRUENDL[12,11], N. GUPTA[10], G. GUTIERREZ[9], N. W. HALVERSON[41,15], S. R. HINTON[49], G. P. HOLDER[11,50,40], D. L. HOLLOWOOD[51], W. L. HOLZAPFEL[52], K. HONSCHEID[53,54], J. D. HRUBES[30], N. HUANG[52], J. HUBMAYR[14], K. D. IRWIN[20,19], J. MENA-FERN'ANDEZ[55], D. J. JAMES[56], F. KÉRUZORÉ[1], L. KNOX[57], K. KUEHN[58,59], O. LAHAV[21], A. T. LEE[52,60], S. LEE[31], D. LI[14,20], A. LOWITZ[17], J. L. MARSHAL[61], M. MCDONALD[22], J. J. MCMAHON[2,23,17], F. MENANTEAU[12,11], S. S. MEYER[2,23,17,24], R. MIQUEL[62,27], J. J. MOHR[3,4,63], J. MONTGOMERY[28], J. MYLES[64], T. NATOLI[17,2], J. P. NIBARGER[14], G. I. NOBLE[65,66], V. NOVOSAD[67], R. L. C. OGANDO[68], S. PADIN[69], S. PATIL[10], M. E. S. PEREIRA[70], A. PIERES[7,68], A. A. PLAZAS MALAG'ON[18,20], C. PRYKE[71], C. L. REICHARDT[10], M. RODR'IGUEZ-MONROY[72], A. K. ROMER[73], J. E. RUHL[74], B. R. SALIWANCHIK[75], L. SALVATI[76], E. SANCHEZ[38], A. SARO[32,34], K. K. SCHAFFER[2,24,77], T. SCHRABBACK[48,78], I. SEVILLA-NOARBE[38], C. SIEVERS[30], G. SMECHER[28,79], M. SMITH[80], T. SOMBOONPANYAKUL[18,81], B. STALDER[82], A. A. STARK[56], E. SUCHYTA[83], M. E. C. SWANSON[12], G. TARLE[8], C. TO[53], C. TUCKER[6], T. VEACH[84], J. D. VIEIRA[11,50], M. VINCENZI[16,80], G. WANG[1], J. WELLER[4,3], N. WHITEHORN[85], P. WISEMAN[80], W. L. WU[20], V. YEFREMENKO[1], J. A. ZEBROWSKI[2,17,9], AND Y. ZHANG[5]

Version February 9, 2024

ABSTRACT

We present a catalog of 689 galaxy cluster candidates detected at significance $\xi > 4$ via their thermal Sunyaev-Zel'dovich (SZ) effect signature in 95 and 150 GHz data from the 500-square-degree SPTpol survey. We use optical and infrared data from the Dark Energy Camera and the Wide-field Infrared Survey Explorer (WISE) and *Spitzer* satellites, to confirm 544 of these candidates as clusters with $\sim 94\%$ purity. The sample has an approximately redshift-independent mass threshold at redshift $z > 0.25$. The confirmed sample spans $1.5 \times 10^{14} < M_{500c} < 9 \times 10^{14} M_{\odot}/h_{70}$ and $0.03 < z \lesssim 1.6$ in mass and redshift, respectively, with a median mass of $2.5 \times 10^{14} M_{\odot}/h_{70}$ and median redshift $z = 0.7$; 21% of the confirmed clusters are at $z > 1$. We use external radio data from the Sydney University Molonglo Sky Survey (SUMSS) to estimate contamination to the SZ signal from synchrotron sources. The contamination reduces the recovered ξ by a median value of 0.032, or $\sim 0.8\%$ of the $\xi = 4$ threshold value, and $\sim 7\%$ of candidates have a predicted contamination greater than $\Delta\xi = 1$. With the exception of a small number of systems ($< 1\%$), an analysis of clusters detected in single-frequency 95 and 150 GHz data shows no significant contamination of the SZ signal by emission from dusty or synchrotron sources. This cluster sample, representing the deepest SZ-selected cluster sample to-date, will be a key component in upcoming astrophysical and cosmological analyses of clusters. In addition to the cluster catalog, we also release the millimeter-wave maps and associated data products used to produce this sample. These maps have depths of 5.3 (11.7) μK_{CMB}-arcmin at 150 (95) GHz and an effective angular resolution of $1'.2$ ($1'.7$). The SPTpol products are available at https://pole.uchicago.edu/public/data/sptpol_500d_clusters/index.html, and the NASA LAMBDA website. An interactive sky server with the SPTpol maps and Dark Energy Survey data release 2 images is also available at NCSA https://skyviewer.ncsa.illinois.edu.

Keywords: Large-Scale Structure of the Universe, Galaxy Clusters

*E-mail:lbleem@anl.gov

[1] High-Energy Physics Division, Argonne National Laboratory, 9700 South Cass Avenue., Lemont, IL, 60439, USA
[2] Kavli Institute for Cosmological Physics, University of Chicago, 5640 South Ellis Avenue, Chicago, IL, 60637, USA
[3] University Observatory, Faculty of Physics, Ludwig-Maximilians-Universität, Scheinerstr. 1, 81679 Munich, Germany
[4] Max-Planck-Institut für extraterrestrische Physik,Giessenbachstr. 85748 Garching, Germany
[5] Cerro Tololo Inter-American Observatory, NSF's National Optical-Infrared Astronomy Research Laboratory, Casilla 603, La Serena, Chile
[6] School of Physics and Astronomy, Cardiff University, Cardiff CF24 3YB, United Kingdom
[7] Laboratório Interinstitucional de e-Astronomia - LIneA, Rua Gal. José Cristino 77, Rio de Janeiro, RJ - 20921-400, Brazil
[8] Department of Physics, University of Michigan, 450 Church Street, Ann Arbor, MI, 48109, USA
[9] Fermi National Accelerator Laboratory, MS209, P.O. Box 500, Batavia, IL, 60510, USA
[10] School of Physics, University of Melbourne, Parkville, VIC 3010, Australia

[11] Department of Astronomy, University of Illinois Urbana-Champaign, 1002 West Green Street, Urbana, IL, 61801, USA

[12] Center for AstroPhysical Surveys, National Center for Supercomputing Applications, Urbana, IL, 61801, USA

[13] Center for Astrophysics | Harvard & Smithsonian, Optical and Infrared Astronomy Division, Cambridge, MA 01238, USA

[14] NIST Quantum Devices Group, 325 Broadway Mailcode 817.03, Boulder, CO, 80305, USA

[15] Department of Physics, University of Colorado, Boulder, CO, 80309, USA

[16] Institute of Cosmology and Gravitation, University of Portsmouth, Portsmouth, PO1 3FX, UK

[17] Department of Astronomy and Astrophysics, University of Chicago, 5640 South Ellis Avenue, Chicago, IL, 60637, USA

[18] Kavli Institute for Particle Astrophysics and Cosmology, Stanford University, 452 Lomita Mall, Stanford, CA, 94305, USA

[19] Department of Physics, Stanford University, 382 Via Pueblo Mall, Stanford, CA, 94305, USA

[20] SLAC National Accelerator Laboratory, 2575 Sand Hill Road, Menlo Park, CA, 94025, USA

[21] Department of Physics & Astronomy, University College London, Gower Street, London, WC1E 6BT, UK

[22] Kavli Institute for Astrophysics and Space Research, Massachusetts Institute of Technology, 77 Massachusetts Avenue, Cambridge, MA 02139, USA

[23] Department of Physics, University of Chicago, 5640 South Ellis Avenue, Chicago, IL, 60637, USA

[24] Enrico Fermi Institute, University of Chicago, 5640 South Ellis Avenue, Chicago, IL, 60637, USA

[25] Instituto de Astrofisica de Canarias, E-38205 La Laguna, Tenerife, Spain

[26] Universidad de La Laguna, Dpto. Astrofísica, E-38206 La Laguna, Tenerife, Spain

[27] Institut de Física d'Altes Energies (IFAE), The Barcelona Institute of Science and Technology, Campus UAB, 08193 Bellaterra (Barcelona) Spain

[28] Department of Physics and McGill Space Institute, McGill University, 3600 Rue University, Montreal, Quebec H3A 2T8, Canada

[29] School of Mathematics, Statistics & Computer Science, University of KwaZulu-Natal, Durban, South Africa

[30] University of Chicago, 5640 South Ellis Avenue, Chicago, IL, 60637, USA

[31] Jet Propulsion Laboratory, California Institute of Technology, Pasadena, CA 91011, USA

[32] Astronomy Unit, Department of Physics, University of Trieste, via Tiepolo 11, I-34131 Trieste, Italy

[33] INAF-Osservatorio Astronomico di Trieste, via G. B. Tiepolo 11, I-34143 Trieste, Italy

[34] Institute for Fundamental Physics of the Universe, Via Beirut 2, 34014 Trieste, Italy

[35] Cornell University, Ithaca, NY 14853, USA

[36] Institute of Particle and Nuclear Studies (IPNS), High Energy Accelerator Research Organization (KEK), Tsukuba, Ibaraki 305-0801, Japan

[37] International Center for Quantum-field Measurement Systems for Studies of the Universe and Particles (QUP-WPI), High Energy Accelerator Research Organization (KEK), Tsukuba, Ibaraki 305-0801, Japann

[38] Centro de Investigaciones Energéticas, Medioambientales y Tecnológicas (CIEMAT), Madrid, Spain

[39] Department of Physics, IIT Hyderabad, Kandi, Telangana 502285, India

[40] Canadian Institute for Advanced Research, CIFAR Program in Gravity and the Extreme Universe, Toronto, ON, M5G 1Z8, Canada

[41] Department of Astrophysical and Planetary Sciences, University of Colorado, Boulder, CO, 80309, USA

[42] Institute of Theoretical Astrophysics, University of Oslo. P.O. Box 1029 Blindern, NO-0315 Oslo, Norway

[43] Faculty of Physics and Astronomy, University of Missouri–Kansas City, 5110 Rockhill Road, Kansas City, MO 64110, USA

[44] Harvey Mudd College, 301 Platt Boulevard, Claremont, CA, 91711, USA

[45] Instituto de Fisica Teorica UAM/CSIC, Universidad Autonoma de Madrid, 28049 Madrid, Spain

[46] Department of Physics and Astronomy, University of Pennsylvania, Philadelphia, PA 19104, USA

[47] European Southern Observatory, Karl-Schwarzschild-Str.,DE-85748 Garching b. Munchen, Germany

[48] Universität Innsbruck, Institut für Astro- und Teilchenphysik, Technikerstr. 25/8, 6020 Innsbruck, Austria

[49] School of Mathematics and Physics, University of Queensland, Brisbane, QLD 4072, Australia

[50] Department of Physics, University of Illinois Urbana-Champaign, 1110 West Green Street, Urbana, IL, 61801, USA

[51] Santa Cruz Institute for Particle Physics, Santa Cruz, CA 95064, USA

[52] Department of Physics, University of California, Berkeley, CA, 94720, USA

[53] Center for Cosmology and Astro-Particle Physics, The Ohio State University, Columbus, OH 43210, USA

[54] Department of Physics, The Ohio State University, Columbus, OH 43210, USA

[55] LPSC Grenoble - 53, Avenue des Martyrs 38026 Grenoble, France

[56] Harvard-Smithsonian Center for Astrophysics, 60 Garden Street, Cambridge, MA, 02138, USA

[57] Department of Physics, University of California, One Shields Avenue, Davis, CA, 95616, USA

[58] Australian Astronomical Optics, Macquarie University, North Ryde, NSW 2113, Australia

[59] Lowell Observatory, 1400 Mars Hill Rd, Flagstaff, AZ 86001, USA

[60] Physics Division, Lawrence Berkeley National Laboratory, Berkeley, CA, 94720, USA

[61] George P. and Cynthia Woods Mitchell Institute for Fundamental Physics and Astronomy, and Department of Physics and Astronomy, Texas A&M University, College Station, TX 77843, USA

[62] Institució Catalana de Recerca i Estudis Avançats, E-08010 Barcelona, Spain

[63] Excellence Cluster Universe, Boltzmannstr. 2, 85748 Garching, Germany

[64] Department of Astrophysical Sciences, Princeton University, Peyton Hall, Princeton, NJ 08544, USA

[65] Dunlap Institute for Astronomy & Astrophysics, University of Toronto, 50 St. George Street, Toronto, ON, M5S 3H4, Canada

[66] David A. Dunlap Department of Astronomy & Astrophysics, University of Toronto, 50 St. George Street, Toronto, ON, M5S 3H4, Canada

[67] Materials Sciences Division, Argonne National Laboratory, 9700 South Cass Avenue, Lemont, IL, 60439, USA

[68] Observatório Nacional, Rua Gal. José Cristino 77, Rio de Janeiro, RJ - 20921-400, Brazil

[69] California Institute of Technology, 1200 East California Boulevard., Pasadena, CA, 91125, USA

[70] Hamburger Sternwarte, Universität Hamburg, Gojenbergsweg 112, 21029 Hamburg, Germany

[71] School of Physics and Astronomy, University of Minnesota, 116 Church Street SE Minneapolis, MN, 55455, USA

[72] Laboratoire de physique des 2 infinis Irène Joliot-Curie, CNRS Université Paris-Saclay, Bât. 100, Faculté des sciences, F-91405 Orsay Cedex, France

1. INTRODUCTION

The advent of high-resolution cosmic microwave background (CMB) surveys has revolutionized the field of galaxy cluster science by enabling the identification of approximately mass-limited samples of massive galaxy clusters (Vanderlinde et al. 2010; Bleem et al. 2015; Planck Collaboration et al. 2016b; Hilton et al. 2018; Bleem et al. 2020) via the thermal Sunyaev-Zel'dovich (SZ) effect (Sunyaev & Zel'dovich 1972). These SZ samples have been used to place stringent constraints on cosmological models (Planck Collaboration et al. 2016a; Bocquet et al. 2019; Zubeldia & Challinor 2019; Salvati et al. 2022), the evolution of the intracluster medium (McDonald et al. 2017; Ghirardini et al. 2021; Flores et al. 2021; CHEX-MATE Collaboration et al. 2021; Anbajagane et al. 2022; Ruppin et al. 2023; Olivares et al. 2022) and the evolution of galaxies residing in clusters (Hennig et al. 2017; Chiu et al. 2018; Strazzullo et al. 2019; Khullar et al. 2022; Kim et al. 2023; Somboonpanyakul et al. 2022). The next generation of CMB surveys, with significantly increased sensitivity, is continuing this revolution by probing lower-mass and correspondingly higher-redshift systems (Huang et al. 2020; Hilton et al. 2021).

With this increased sensitivity comes both new opportunities (Simons Observatory Collaboration 2019; Chaubal et al. 2022) and challenges (Melin et al. 2018; Zubeldia et al. 2023) for cosmological and astrophysical analyses with SZ clusters. The enlarged sample sizes will also strengthen cross-wavelength analyses, for which comparisons of cluster samples selected via different techniques provide powerful ways to validate the robustness of analysis inferences and can signal the presence of unmitigated systematic errors (Grandis et al. 2021; Costanzi et al. 2021; Orlowski-Scherer et al. 2021).

In this work we continue the push to discover SZ clusters in low-noise and high-resolution CMB survey data by presenting a galaxy cluster sample constructed using the 500-square-degree SPTpol survey. This survey, which covers five times the area used in the 100-square-degree SPTpol field (hereafter SPTpol 100d) cluster analysis (Huang et al. 2020), benefits from approximately two-to-three times lower noise than the survey data used

to construct the published cluster samples from SPT-SZ (Bleem et al. 2015) and ACTpol (Hilton et al. 2021). The new cluster sample is composed of 689 cluster candidates detected at significance $\xi > 4$, and we have confirmed 544 of these candidates as galaxy clusters using optical and infrared imaging data. Here we provide the complete cluster candidate list and—where available—redshifts, estimated masses, and select optical properties.

We organize our description of the identification and characterization of this new sample as follows. In Section 2 we describe the collection of the millimeter-wave data and its processing into the maps used for cluster identification. We detail the procedure by which we identify SZ cluster candidates in these maps in Section 3. In Section 4 we describe the optical and infrared data sets we use to confirm candidates as galaxy clusters by the techniques described in Section 5. In Section 6 we describe how we estimate cluster masses and estimate the purity of our cluster sample. In Section 7 we describe a number of systematic checks to explore possible astrophysical contamination of the SZ signal. In Section 8 we present the properties of the resulting SZ cluster catalog and compare select properties of this catalog to other SZ- and optically selected cluster samples. Finally, we summarize our results and conclusions in Section 9.

In addition to the cluster sample we also release the SPTpol maps and associated data products used in the construction of this catalog. These products can be found on both the NASA Legacy Archive for Microwave Background Data (LAMBDA)[1] and the South Pole Telescope (SPT) collaboration's website[2]. Sky maps for the 500d region from SPTpol single-frequency data as well as images from the Dark Energy Survey (DES)-DR2 (Abbott et al. 2021) dataset can be accessed for exploration at the National Center for Supercomputing Applications (NCSA) Skyviewer.[3]

Finally we note that, where applicable, we assume a fiducial ΛCDM cosmology with $\sigma_8 = 0.80$, $\Omega_b = 0.046$, $\Omega_m = 0.30$, $h = 0.70$, $n_s(k_s = 0.002) = 0.972$, and $\Sigma m_\nu = 0.06$ eV. Magnitudes are reported in the AB system (Oke 1974). Cluster masses are reported in terms of M_{500c}, which is defined as the mass enclosed within a radius, r_{500c}, at which the average enclosed density is $500\times$ the critical density at the cluster redshift.

2. OBSERVATIONS AND DATA REDUCTION

The cluster catalog presented in this work was constructed via an analysis of 95 and 150 GHz data from the primary SPTpol (Austermann et al. 2012) survey field. This 500-square-degree field is centered at right ascension and declination ($\alpha=0^h$, $\delta= -57.5°$) and is hereafter referred to as the SPTpol 500d field; see Figure 1. The maps have depths of 11.7 and 5.3 μK-arcmin at 95 and 150 GHz, respectively, and effective resolutions of $1'.7$ and $1'.2$ set by the instrumental response (i.e., telescope beam). The SPTpol data in this field have been the focus of a number of previous analyses including characterizations of low- and high-ℓ CMB temperature and polarization power spectra (Henning et al. 2018; Sayre

[73] Department of Physics and Astronomy, Pevensey Building, University of Sussex, Brighton, BN1 9QH, UK
[74] Department of Physics, Case Western Reserve University, Cleveland, OH, 44106, USA
[75] Brookhaven National Laboratory, Upton, NY 11973, USA
[76] Université Paris-Saclay, CNRS, Institut d'Astrophysique Spatiale, 91405, Orsay, France
[77] Liberal Arts Department, School of the Art Institute of Chicago, 112 South Michigan Avenue, Chicago, IL,60603, USA
[78] Argelander-Institut für Astronomie, Auf dem Hügel 71, D-53121 Bonn, Germany
[79] Three-Speed Logic, Inc., Victoria, B.C., V8S 3Z5, Canada
[80] School of Physics and Astronomy, University of Southampton, Southampton, SO17 1BJ, UK
[81] Department of Physics, Faculty of Science, Chulalongkorn University, 254 Phayathai Road, Pathumwan, Bangkok Thailand. 10330
[82] Vera C. Rubin Observatory Project Office, 933 North Cherry Avenue, Tucson, AZ 85721, USA
[83] Computer Science and Mathematics Division, Oak Ridge National Laboratory, Oak Ridge, TN 37831
[84] Space Science and Engineering Division, Southwest Research Institute, San Antonio, TX 78238
[85] Department of Physics and Astronomy, Michigan State University, East Lansing, MI 48824, USA
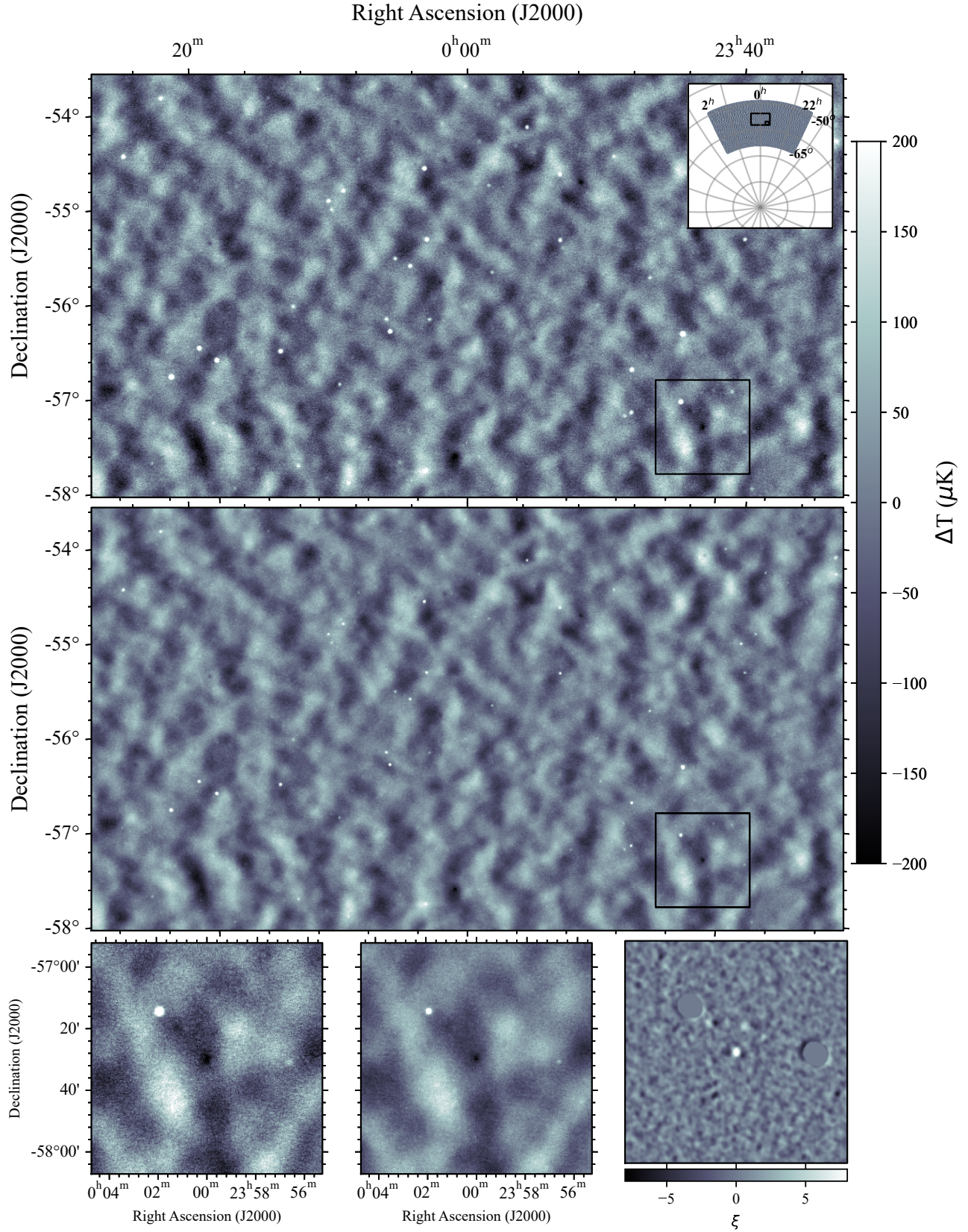
Figure 1. Sequentially zoomed-in images of the SPTpol 500d field, with the full field shown in inset at top. *(Top panel)* 24 deg^2 of 95 GHz data *(Middle panel)* The same region at 150 GHz. The full field temperature maps and associated data products are released along with this work. *(Bottom panel)* To better illustrate the sensitivity of these maps to small scales, we further zoom in to a 1.25 × 1.25 degree region (outlined in black in above panels) centered on SPT-CL J2341-5724, a $\xi = 14.3$ cluster at $z = 1.259$. Plotted from left-to-right are the 95 and 150 GHz temperature maps and the ξ-map constructed for optimal detection of clusters with $\theta_{core} = 0.25$. Sources brighter than 6 mJy at 150 GHz were masked in the cluster detection step, with two examples visible in the bottom right panel.

et al. 2020; Reichardt et al. 2021), the CMB gravitational lensing signal (Wu et al. 2019; BICEP/Keck Collaboration and SPTpol Collaboration et al. 2021; Raghunathan et al. 2019), and the properties of emissive sources (Gupta et al. 2019). The overall map-making and data processing procedures utilized here closely follow those of previous efforts. In this section we provide a brief summary of these procedures, highlighting changes specific to this work, and refer readers to prior publications for more details.

2.1. *Data Processing*

The maps presented here are the weighted sum of > 4000 individual observations ($\sim$10,200 hours) of the SPTpol 500d field acquired between 2013 April 30 and 2016 Aug 20. The majority of the observations were obtained by scanning the telescope in azimuth back and forth across the field, stepping in elevation, and repeating this process until the full field was covered. As detailed in Henning et al. (2018), most of the data obtained before 2014 May 29 was acquired instead in "lead-trail" mode. In this mode, the field is split into two equal halves via an equal division in right ascension. These two subfields were then sequentially scanned, with starting times offset owing to sky rotation, such that the same azimuthal range was covered by the telescope in each subfield. For this analysis we combine these "lead" and "trail" observations into full-field observations to match the rest of the 500d dataset.

The SPTpol data processing pipeline converts time-ordered electrical signals recorded by the camera into calibrated maps of the millimeter-wave (mm-wave) sky. We apply standard detector quality cuts (Crites et al. 2015) and electrical cross talk corrections to the time-ordered data (TOD). Following Bleem et al. (2020), to minimize the impact of low-frequency noise from the atmosphere and detector readout, both a common mode filter that removes the mean of all detectors in each frequency band and a seventh-order Legendre polynomial were fit to and subtracted from the TOD for each azimuthal scan. A scan-direction high-pass filter at angular multipole $\ell = 300$ and similar low-pass filter at $\ell = 20,000$ were then applied. Bright emissive sources detected at 150 GHz at > 6 mJy were masked with masks of $4'$ radii during these filtering steps so as to not bias the fits or imprint artifacts in the resulting maps.

Using the telescope pointing model and weights for the individual bolometers based on their noise in the 1-3 Hz band, the TOD was binned into $0\rlap{.}'25$ pixels in the Sanson-Flamsteed projection (Calabretta & Greisen 2002). The noise properties of each single-observation map were characterized and, following removal of a small number of maps with anomalous noise behavior, the observations were then combined via inverse noise-variance weighting to produce the final coadded maps of the field.

2.2. *Removal of Emissive Sources that Cause Spurious Cluster Candidates*

As discussed in Huang et al. (2020), unmasked emissive sources in the maps can lead to spurious cluster candidates owing to decrements produced by the sources "ringing" when the maps are high-pass filtered. To mitigate the number of such spurious detections, we identify and remove moderate signal-to-noise (S/N) sources below our masking threshold from the maps before cluster detection occurs.

We first filter each individual frequency map with a filter optimized to detect point sources and construct a catalog of emissive sources detected at S/N > 6 and below the masking threshold of 6 mJy at 150 GHz used in the map construction. This corresponds to thresholds of ~ 4 mJy (3.5 mJy) at 95 GHz (150 GHz). A total of 348 sources were detected at 95 GHz and 382 at 150 GHz (245 at S/N> 6 in both maps). When sources were only detected in one of the two frequency maps the other frequency map was forced-photometered to recover the missing flux.

An empirical template of the 2D source profile, incorporating the effects of the beam and transfer function, was constructed by creating a flux-normalized median stack of the raw unfiltered maps at the locations of the ~ 200 brightest sources at each frequency (see Figure 2). A flux-scaled copy of this template was then subtracted from the raw maps at the location of each of the detected sources. Analysis of the cluster catalog (whose construction is detailed in the next section) showed this simple procedure was sufficient to remove the spurious candidates associated with these emissive sources. Artifacts from remaining lower flux sources contribute $< 2\sigma$ SZ-like signals in the cluster detection maps. We use these source subtracted maps in all of our cluster identification steps.

3. IDENTIFICATION OF CLUSTER CANDIDATES

We closely follow the procedure utilized in previous SPT publications (most recently Huang et al. 2020; Bleem et al. 2020) to identify cluster candidates in the SPTpol 500d field with some small changes we explain below. As in these works, we filter the maps with a spatial-spectral filter that has been optimized to isolate cluster signals in the presence of frequency- and scale-dependent sources of noise (Melin et al. 2006). The spatial profile of clusters are modeled as a series of projected spherical β profiles (Cavaliere & Fusco-Femiano 1976)

$$\Delta T = \Delta T_0 (1 + \theta^2/\theta_c^2)^{-(3\beta-1)/2} \tag{1}$$

with $\beta = 1$, a free normalization, ΔT_0, and with core radii, θ_c, that are allowed to vary in twelve equally spaced steps from $0\rlap{.}'25$ to $3'$. The frequency dependence of the temperature signal in each map, ΔT, is given by the thermal SZ effect (Sunyaev & Zel'dovich 1972). At the SPTpol effective band centers of 95.9 and 148.5 GHz for a non-relativistic thermal SZ spectrum, this results in the thermal SZ signal being $1.6\times$ brighter (in CMB temperature units) in the 95 GHz than 150 GHz data. This enhancement of the signal amplitude largely offsets the higher instrumental noise in the 95 GHz data, and—combined with the impacts of astrophysical noise discussed below—results in the two channels contributing close to equal weight in the construction of the cluster catalog. The noise in the SPTpol maps is broadly composed of two components: (1) astrophysical/cosmological "noise" arising from fluctuations in the primary CMB and emission from extragalactic sources and (2) noise specific to our observations arising from the SPTpol instrument as well as residual atmospheric contamination.
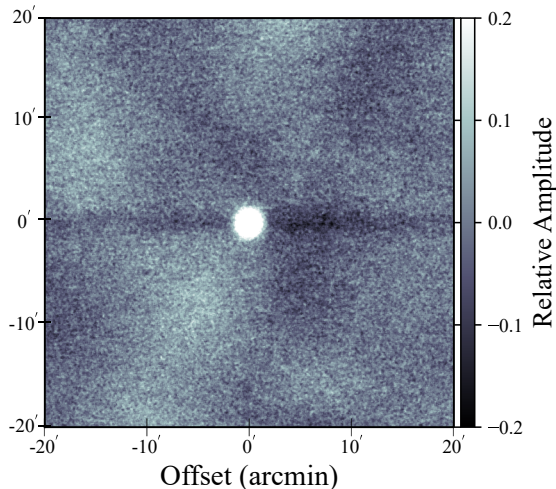
Figure 2. $40' \times 40'$ normalized median stack of sources at 95 GHz used to make the source subtraction template; a similar template was constructed at 150 GHz. The negative filtering artifacts along the scan (horizontal) direction are clearly visible even in these stacks which have significant residual large scale noise contributions from the primary CMB.

The SPTpol data are deep enough that—for identical reasons as in the case of moderate signal-to-noise emissive sources discussed in Section 2.2—the Fourier filtering induces spurious candidates around massive clusters along the telescope scan direction. As the sky density of such clusters is significantly lower than that of the emissive sources—0.09 per $\deg^2$ at the conservative threshold we apply below—and they have a less well defined shape, we do not attempt to subtract a model of these clusters from the map. Instead we use a two-step procedure to construct a clean cluster candidate list that also recovers the properties of the most massive systems.

In the first step, we perform a cluster detection run on the maps masking both emissive sources with flux > 6 mJy at 150 GHz and massive clusters previously detected in the SPT-SZ survey[1] at significance[2] $\xi \geq 6$. This corresponds to a masking threshold of $M_{500c} \gtrsim 4.5 \times 10^{14} M_{\odot}/h_{70}$. We use $4'$ radii masks and further exclude cluster candidates detected within $8'$ of these objects. Cluster candidates identified with $\xi > 4$ in this step from the SPTpol data form the core of the new cluster sample.

In the second step, to include the massive clusters masked in the previous step in our catalog, we perform a second filtering of the maps in which only the emissive sources > 6 mJy at 150 GHz are masked. We then add only the new detections of previously masked clusters and their properties to our cluster candidate list. There were no clusters masked in the first step that did not exceed our $\xi \geq 4$ cut. We validated through comparison of the noise properties in the two filtering steps that the presence of the most massive systems does not impact the estimated noise. We additionally visually inspected cutouts of the raw and filtered maps around all

---

[1] The SPT-SZ survey covers all but 1 $\deg^2$ of the SPTpol 500d field.

[2] In this work, as in all previous SPT cluster publications, we define significance, ξ, as the maximum detection significance across the 12 matched filter scales.

$\xi > 4$ cluster candidates to validate our treatment of both emissive sources and the highest signficance clusters. In total, after all masking is accounted for, 460 of the 498 $\deg^2$ uniform depth region (92%) of the SPTpol 500d field was included in the cluster search.

4. FOLLOW-UP OBSERVATIONS

SZ galaxy cluster candidates are confirmed and redshifts obtained via the identification of significant galaxy overdensities in optical and/or infrared imaging data. These data are drawn from both wide-field imaging surveys and targeted photometric and spectroscopic follow-up observations. The majority of our candidates are confirmed using data from the DES (Flaugher et al. 2015) and the highest-redshift clusters are confirmed using observations from the Wide-field Infrared Survey Explorer (WISE; Wright et al. 2010) and *Spitzer*/IRAC (Fazio et al. 2004). A small number of candidates at the borders of the SPTpol survey do not overlap with DES; these candidates are characterized using data from the DECam Legacy Survey (DECaLS; Dey et al. 2019).

4.1. *Optical/Near-Infrared Imaging from the Dark Energy Camera*

The DES is a $\sim$5000 $\deg^2$ 5 band *grizY* optical and near-infrared imaging survey that was conducted using the 4 m Blanco telescope at Cerro Tololo Inter-American Observatory in Chile. Data were acquired over 760 nights between August 2013 and January 2019 (Abbott et al. 2021). In this analysis, we make use of photometric catalogs extracted from the full 6 year coadds. These data reach median 10σ coadded depths in $1''.95$ apertures of [24.7, 24.4, 23.8, 23.1, 21.7] magnitude in the *grizY* bands. The DES data cover almost the entire SPTpol 500d field and are typically deep enough to robustly confirm SPTpol cluster candidates to redshift $z \sim 1.1$.

Eighteen candidates at the edges of the SPTpol 500d field fall outside the DES coverage region. We use *griz* photometry data from the tenth data release of DECaLS[1] to confirm and obtain redshifts for 11 of these candidates; the remaining 7 candidates are unconfirmed after optical/infrared analysis. Tests of cluster redshift estimates using systems in regions where DES and DECaLS overlap show good agreement.

4.2. *Wide Field Infrared Explorer*

To detect candidates at higher redshifts, we analyze data from the all-sky WISE dataset. Specifically we use 3.4 μm and 4.6 μm data (*W1* and *W2* band, respectively) from the "unWISE" analysis of Schlafly et al. (2019) which combined five years of data from WISE and NEOWISE (Mainzer et al. 2014) data at native WISE resolution.

4.3. *Spitzer/IRAC*

A subset of high-redshift cluster candidates were also targeted with *Spitzer*/IRAC at 3.6 and 4.5 μm ([3.6] and [4.5] bands). These deeper data are significantly higher resolution than WISE ([3.6]$_{\mathrm{FWHM}} \sim 2''$ compared to $6''$ from WISE *W1*), allowing us to confirm additional high-redshift clusters as well as to validate our WISE analysis. *Spitzer*/IRAC observations of cluster candidates are

---

[1] https://www.legacysurvey.org/dr10/description/

drawn from three sources: 50 candidates were previously targeted for follow-up observations in the production of the SPT-SZ cluster sample (PI: Brodwin, see details in Bleem et al. 2015), 84 cluster candidates were imaged in new targeted observations in *Spitzer* cycles 11, 12, and 14 (Program IDs 11096, 12073, 14096; PI: Bleem), and 163 cluster candidates (at any redshift) were within the footprint of the *Spitzer* South Pole Telescope Deep Field (SSDF; Ashby et al. 2013), with 31 of these candidates also having deeper targeted follow-up from the earlier SPT-SZ work.

The SPTpol candidates imaged in Cycles 11-14 were initially detected in preliminary versions of the SPTpol 500d cluster sample, and were selected for infrared follow-up based on the absence of galaxy overdensity counterparts in then existing DES data (DES Year 1 and DES Year 3, depending on the cycle; Abbott et al. 2018). In the new *Spitzer* observations, candidates were observed in each band in 6×30 s exposures and the data were reduced following the procedures detailed in Ashby et al. (2009). This exposure time is sufficient to reach a 5σ sensitivity of 4.8μJy at 3.6μm in an aperture-corrected $4''$ aperture. Here we use $4''$ diameter aperture-corrected magnitudes.

5. CLUSTER CONFIRMATION AND REDSHIFT ESTIMATION

The majority of newly confirmed cluster candidates in this work were confirmed using the multi-component matched filter cluster confirmation tool (MCMF) previously described in detail in Klein et al. (2018, 2019).

5.1. *MCMF*

As explained in Klein et al. (2018, 2019), the MCMF algorithm was designed to provide—amongst other properties—cluster confirmation, redshift, and cluster galaxy richness information for samples of X-ray and SZ clusters by robustly identifying associated cluster galaxy counterparts. We provide a brief overview of the method here, including choices specific to this analysis, and refer readers to previous works for more details. The MCMF algorithm works as follows:

- At the location of each cluster candidate, local background-corrected cluster richnesses, λ_{MCMF}, are estimated as a function of redshift from $0.01 < z < 2$, in steps of $\delta_z = 0.005$.

- These richnesses are computed as the sum of galaxy weights within a projected radius of r_{500c} centered on the SZ candidate location where r_{500c} is determined from the $\xi - M_{500c}$ relation (see Section 6) at the redshift of interest.

- Galaxy weights are computed for galaxies brighter than $i \leq m^*(z)+1.25$[1] and are based on (1) the consistency of galaxy colors and magnitudes with a redshift-dependent cluster population model and (2) a radial weight from the SZ center based on a normalized Navarro, Frenk and White (NFW) profile (Navarro et al. 1997) with a scale radius

---

[1] Here m^* corresponds to the apparent magnitude of L* galaxies, modeled as described in Klein et al. (2019).

of $R_s = r_{500c}/3$ (Hennig et al. 2017). Following e.g., Gladders & Yee (2000), a passive red-sequence population model is used to describe the color-magnitude relation of cluster galaxies. This model was empirically calibrated using $\sim 2,500$ clusters with spectroscopic redshifts from the SPT-SZ cluster catalog (Bleem et al. 2015; Bayliss et al. 2016; Khullar et al. 2019), the redMaPPer (RM) Y1 catalog (Rykoff et al. 2016; McClintock et al. 2019), and the MCXC cluster catalog (Piffaretti et al. 2011). At low redshift, the 4000Å break drives redshift determination, while at high redshift ($z > 1.1$) where WISE data are used, the "1.6 μm Stellar Bump" feature (see Section 5.2) provides discriminating power.

- A correction is applied as needed to the richness at high redshift where the data are not complete to $m^*(z)+1.25$.

- Random sight lines are used to determine the probability of false associations as a function of redshift (z_i) and richness (λ_i), with this contamination fraction given by:

$$f_{\mathrm{cont}}(\lambda_i, z_i) = \frac{\int_{\lambda_i}^{\infty} f_{\mathrm{rand}}(\lambda, z_i)d\lambda}{\int_{\lambda_i}^{\infty} f_{\mathrm{obs}}(\lambda, z_i)d\lambda}. \quad (2)$$

where f_{rand} is the richness distributions along random lines-of-sight and f_{obs} is the richness distributions along candidate lines of sight.

- Up to three peaks per candidate are analyzed in richness-redshift space, with the peak associated with the lowest chance of being contamination assigned as the most likely counterpart to the SPT cluster candidate.

- Below a threshold of $f_{\mathrm{cont}} = 0.2$ we denote candidates as "confirmed". The expected net contamination in the confirmed sample is a combination of the intrinsic purity of the SZ sample (see Section 6.4) and the optical/IR contamination. Under the assumption that the follow-up data is sufficiently deep to detect all real associations, the contamination of the optically confirmed sample is given by (see also Klein et al. 2023):

$$\mathrm{contamination} = f_{\mathrm{cont}}^{\max} * (1 - p(\xi > \xi_{\min})) \quad (3)$$

where $p(\xi > \xi_{\min})$ is the purity of the complete SZ candidate sample at $\xi > \xi_{\min}$, and we adopt $f_{\mathrm{cont}}^{\max} = 0.2$.

In Table 1 we provide MCMF summary statistics for the cluster candidates (except when confirmed by *Spitzer*, see below) including their redshifts and optical richnesses.

5.2. *Spitzer Confirmation*

For those cluster candidates with available higher-resolution and deeper *Spitzer* observations, we adopt a simpler, though related approach, to measuring the cluster redshifts, richnesses, and false associations. Given the small field-of-view of the targeted observations it is not possible to apply local background corrections.
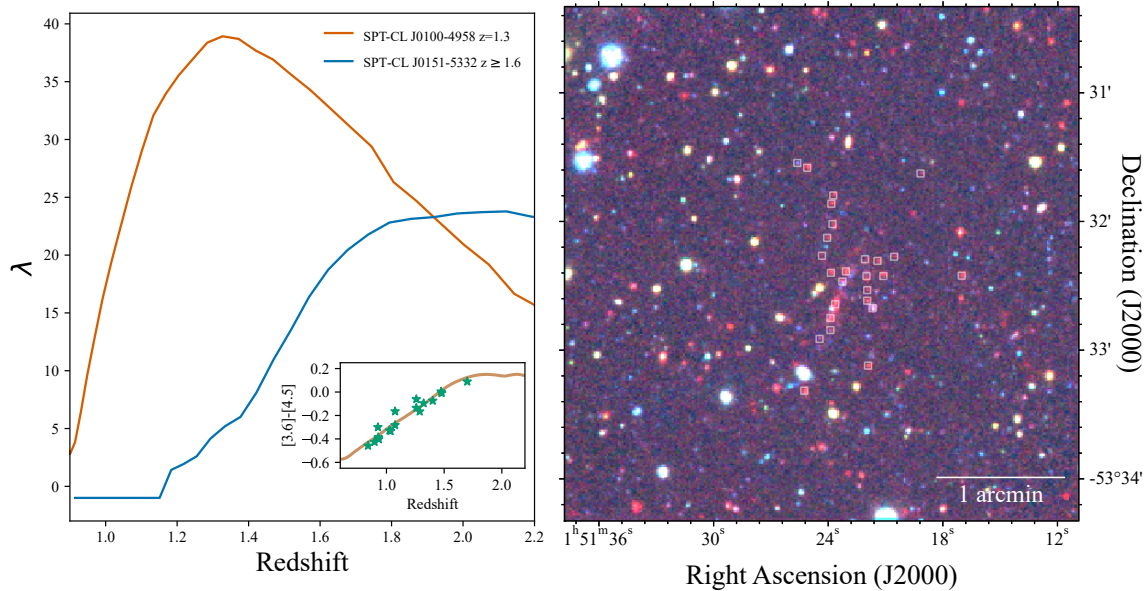
Figure 3. *(Left)* Example of *Spitzer* redshift determination on two high-z SPTpol clusters. Plotted are IR richness (λ) versus redshift. In the inset we plot the median $[3.6]-[4.5]$ color for SPT clusters with spectroscopic redshifts (green stars) and in brown we overplot our synthetic model calibrated using these systems. As can be seen, the *Spitzer* colors lose redshift discrimination power at $z > 1.6$ and so we assign all systems with higher best-fit redshifts to $z = 1.6$ and note this is a lower limit. *(Right)* SPT-CL J0151$-$5332 at $z \geq 1.6$ with identified cluster members marked with white squares. The RGB image is constructed from *Spitzer* $[3.6]$ and DES i- and g- band data.

Clusters are confirmed in *Spitzer* data via the identification of excess galaxies at the cluster candidate locations as a function of $[3.6]-[4.5]$ color via a variation of the "1.6 μm Stellar Bump method" previously employed in e.g., Papovich (2008); Muzzin et al. (2013); Gonzalez et al. (2019). As detailed in these previous works, after excluding low-redshift galaxies, there is a close mapping between the *Spitzer* color and redshift. We generate our model for this relation using the GALAXEV package (Bruzual & Charlot 2003) assuming that the cluster galaxy population was formed by a single starburst at $z = 3$ with a Salpeter initial mass function (Salpeter 1955) and then followed the MILES (Vazdekis et al. 2010) evolutionary tracks thereafter. As noted in e.g., Sorba & Sawicki (2010), the 1.6 μm feature is a robust feature immune to the details of the star formation history for all but the youngest stellar populations.

We match sources selected from the *Spitzer* fields[2] to optically selected counterparts from the DES using a 1″ matching radius. Following Muzzin et al. (2013); Gonzalez et al. (2019), to reduce the number of low-z interloper galaxies, we remove galaxies with $z - [3.6] < 1.6$ and $i < 21.3$ from our catalogs. We next run the single-color λ-richness estimator introduced in Rykoff et al. (2012) modified to use our 1.6 μm bump redshift model in place of the red-sequence model. We adopt an intrinsic color-spread in the model at fixed redshift of $\sigma_{[3.6-4.5]} = 0.07$ (Muzzin et al. 2013). Background galaxy densities are estimated from either 25 blank-field pointings of unconfirmed cluster candidates from the SPT-SZ sample (Bleem et al. 2015) for the deep *Spitzer* observations or from the full SSDF field for the shallower observations.

Following MCMF (Klein et al. 2023), we also modify the radial extent of the richness aperture to extend to what would be r_{500c} for a cluster detected at significance ξ at the redshift of interest. Richnesses were computed from $0.8 < z < 2$ with the candidate assigned the redshift and richness corresponding to the maximum λ value. The $[3.6]-[4.5]$ color loses redshift discrimination power at $z > 1.6$ so systems with solutions at higher redshift are assigned $z = 1.6$ and flagged in the catalog. An example of this fitting procedure for two different high-z SPTpol clusters is shown in Figure 3.

While we do apply a color cut to remove low-redshift galaxies, faint galaxies below the DES detection limit can enter our catalog. As the 1.6 μm bump redshift model above $z \sim 0.7$ is degenerate with solutions at low-redshift (see e.g., Figure 1 in Muzzin et al. 2013), we also apply a secondary run estimating λ versus redshift from $0.1 < z < 2$ and visually inspect all outputs, flagging and removing cases where low-redshift interlopers are biasing our results. In the vast majority of cases, these contaminants do indeed correspond to galaxies in the faint end of the luminosity function of rich low-redshift clusters confirmed by MCMF in DES optical data alone. A future improvement to our *Spitzer* confirmation work will incorporate additional optical information beyond our simple color cut.

We also follow a similar convention to MCMF to estimate the contamination of the confirmed sample at fixed λ but here restrict ourselves to a single wide redshift bin from $1 < z < 2$. To compute this contamination fraction we first select ~ 800 random locations in the SSDF (with galaxies also matched to DES and the color cut to remove low-z galaxies applied) that were screened to be $> 5'$ from any SPTpol cluster candidate and not in highly masked regions of DES. We randomly assigned each location a ξ value from the SPTpol catalog and then

---

[2] Which we convert from Vega to AB magnitudes using the offsets of $m_{AB} = m_{Vega} + 2.79$ (3.26) for the $[3.6]$($[4.5]$) bands (Papovich et al. 2016).

estimated λ as for the real candidates to generate our random distribution. We denote fractional contamination determined using *Spitzer* data as f_{Scont}. We adopt a somewhat more conservative threshold ($f_{\mathrm{Scont}} < 0.1$ versus $f_{\mathrm{cont}} < 0.2$ from MCMF) for our *Spitzer* confirmation thresholds given the steepness of this contamination fraction with declining richness and our limited ability to sample blind *Spitzer* fields across the full 500d survey.

5.3. *Comparison Between WISE and Spitzer Observations*

We can compare the performance of MCMF as applied to the DES-WISE dataset on high-z clusters that were also observed in higher-resolution *Spitzer*/IRAC data. In total we have 108 candidates observed with *Spitzer* with estimated redshifts $z \geq 0.85$ and *Spitzer*-derived contamination $f_{\mathrm{Scont}} < 0.1$. Of these systems, 78 are also confirmed via MCMF and have redshifts in decent agreement ($|\delta z| < 0.2$) with the *Spitzer* estimates. For the remaining 30 systems, differences in redshift/confirmation estimates between the MCMF and *Spitzer* analyses fall in two (expected) categories (1) detection in *Spitzer* data of higher-z systems not well detected by MCMF in DES+WISE data, (2) identification of different galaxy over-densities along the line of sight, leading to different redshift estimates. In the first scenario, 14 high-z systems confirmed by *Spitzer* are not confirmed by MCMF ($f_{\mathrm{cont}} > 0.2$); 5 of these systems have MCMF redshifts approximately consistent with those obtained by *Spitzer*, but with richnesses up to a factor of $2\times$ smaller, and 9 are solely detected in *Spitzer* data. The remaining 16 systems have significant differences in identified counterparts/redshifts between the algorithms. After further inspection, for 9 of these systems we selected the *Spitzer*-identified over-density as the primary counterpart as it is better centered on the SZ detection or a richer detection and comparably centered (see Figure 4 and the middle panel of Figure 10 for two examples). For the remaining 7 systems the MCMF detection was selected as the primary counterpart. We flag systems with multiple significant over-densities along the line of sight in the cluster candidate table, Table 1.

In summary, we find generally good agreement between the MCMF/WISE and *Spitzer* analyses and that the WISE analysis provides an excellent addition to the analysis of DES data when deeper higher-resolution IR imaging is not available. The lower-resolution WISE data naturally has some limitations, and we find that the *Spitzer* data provide surer cluster confirmations (5 systems) or enables new detections not found in the WISE analysis (15 additional systems), impacting 20/108 clusters (16/51 at $z > 1.1$) for which we had both datasets. In the near future data from the *Euclid* mission (Laureijs et al. 2011) will enable us to reach beyond the limits of WISE confirmations for the full sample. These data, expected to allow detections of high-z clusters to $z \sim 2$ (Euclid Collaboration et al. 2019), will enable confirmations of additional high-z systems from this SPTpol sample as well as future cluster samples from SPT-3G (Sobrin et al. 2018).

6. MASS ESTIMATION AND SAMPLE PURITY

In this section, we detail how we connect our SPT observable, ξ, to mass. We also explain how we use realistic
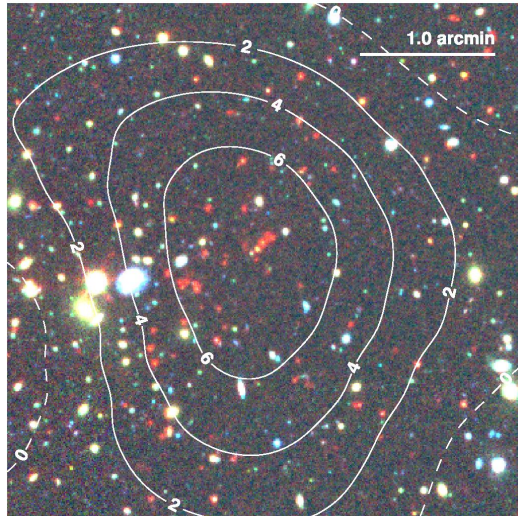
Figure 4. Example of a system with multiple significant over-densities along the line-of-sight. SPT-CL J2331−5737 at $\xi = 7.6$ has potential counterparts located at (redshift, richness) $z = 0.3, \lambda = 65$ and $z = 1.5, \lambda_{\mathrm{Spitzer}} = 25$. We adopt the higher-$z$ counterpart as our primary identification given its excellent alignment with the SPT position. While richer, the lower-z counterpart is centered $\gtrsim 70''$ away from SPT detection; the statistical uncertainty on the SPT position is $11''$. The RGB image is constructed from *Spitzer* [3.6] and DES r- and g- band data.

simulations of the SPTpol 500d field to explore the expected behavior of our observable-mass scaling relation and to estimate the purity of the SZ candidate list.

6.1. *The ζ-Mass Scaling Relation*

As in previous SPT cluster catalogs, we use an observable-mass scaling relation to relate our detection significances to mass. This is done through a two step process. First, as discussed in Vanderlinde et al. (2010), to account for the bias owing to the maximization of the cluster detection algorithm over position and filter scales, we relate our observable ξ to ζ, an "unbiased" detection significance via

$$P(\xi|\zeta) = \mathcal{N}(\sqrt{\zeta^2 + 3}, 1) \qquad (4)$$

for $\zeta > 2$ (see also a formal derivation of this maximization correction in Zubeldia et al. 2021).

Next, this unbiased significance is connected to mass via the relation:

$$\langle \ln \zeta \rangle = \ln\Big[A_{\mathrm{SZ}} \left(\frac{M_{500c}}{3 \times 10^{14} M_{\odot} h^{-1}} \right)^{B_{\mathrm{SZ}}} \left(\frac{H(z)}{H(0.6)} \right)^{C_{\mathrm{SZ}}} \Big],$$
$$(5)$$

and

$$P(\ln \zeta | M, z) = \mathcal{N}[\langle \ln \zeta \rangle (M, z), \sigma_{\ln \zeta}] \qquad (6)$$

where A_{SZ} is the normalization, B_{SZ} the slope, C_{SZ} the redshift evolution, $\sigma_{\ln \zeta}$ the log-normal scatter on ζ, and $H(z)$ is the Hubble parameter. As in Reichardt et al. (2013) and other SPT cluster works thereafter, we rescale the normalization to account for varying depth in the different SPT survey regions

$$A_{\mathrm{SZ}} \to \gamma_{\mathrm{field}} A_{\mathrm{SZ}}. \qquad (7)$$

6.2. *Simulations of the SPTpol field*

We make use of simulations tailored to mimic the SPT-pol observations to measure the rescaling factor, γ, for the 500d field as well as to estimate the sample purity. Following Bleem et al. (2020); Huang et al. (2020), we have constructed five realizations of the 500d field by combining realizations of the CMB (Keisler et al. 2011)[1], cosmic infrared background (CIB; Reichardt et al. 2021), discrete radio sources (De Zotti et al. 2005) with spectral indices consistent with Everett et al. (2020), thermal SZ, and instrumental/residual atmospheric noise (the latter hereafter referred to as "instrumental noise" for brevity). The thermal SZ maps are created by applying the methods of Flender et al. (2016) to halo lightcones from the Outer Rim simulation (Heitmann et al. 2019) and the instrumental noise maps are constructed from jackknife coadds of the SPT maps in which half of the observations were multiplied by -1 in order to produce maps with no sky signal. The SPT beam and transfer function are then applied to the simulated maps. The emissive source subtraction on the real maps (Section 2.2) reduces both the noise during cluster detection (by $\sim 3\%$ in the filtered maps) and the number of spurious cluster candidates. To mimic the effect of this subtraction in the simulations, we do not include radio sources brighter than the flux above which the source density of our radio source model matches the density of sources subtracted from the maps.

Following Reichardt et al. (2013), to measure γ, we first filter the maps with the same optimal filters used in the cluster identification and extract the ζ values at the known location and optimal filter scales of the simulated clusters. We then fit for the scaling relation parameters (Eq. 5 above). We measure $\gamma = 2.23$ for the SPTpol 500d field. This value implies the SPTpol 500d field depth should be roughly comparable to SPTpol 100d, and that clusters should be detected at $\sim 1.8\times$ higher significance in SPTpol than SPT-SZ (see e.g., Table 1 in de Haan et al. 2016).

We also tested the consistency of the B_{SZ} and C_{SZ} parameters measured in the SPTpol 500d simulations with those measured in simulated fields from the SPT-SZ (Bleem et al. 2015) and SPT-ECS (Bleem et al. 2020) surveys. While we find B_{SZ} to be consistent with previous values at better than the 1σ level, the best fit C_{SZ} values have increased by $\Delta C_{SZ} = 0.26$, corresponding to a 7σ shift in the simulations.

This change in C_{SZ} arises from a combination of the reduced noise level and the larger contribution of the 95 GHz data to cluster detection in SPTpol compared to SPT-SZ. Decreasing the noise level increases sensitivity to higher-redshift clusters more than lower-redshift ones because of the fixed low-ℓ "noise" contribution from the primary CMB. Meanwhile, the increased weight at 95 GHz improves sensitivity to low-redshift clusters. We have confirmed both of these trends in simulations: The values for $C_{SZ,95\ only}$ and $C_{SZ,150\ only}$ determined by running the cluster finder on single frequency maps are below

---

and above the combined joint analysis value by 0.2, respectively, meanwhile excluding instrumental noise from simulations increases C_{SZ}. We surmise that, in the data, the effect of the noise reduction is larger, resulting in an increase in C_{SZ}.
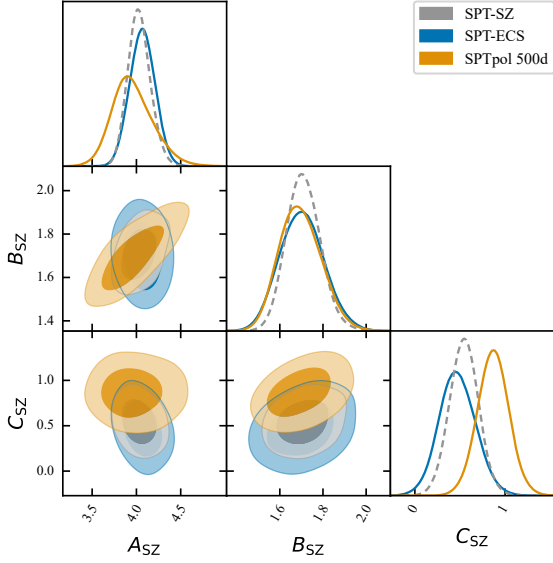
6.3. *Scaling Relation Parameters*

In recent works, we have used scaling-relation parameters based on best-fit weighted averages from a Monte Carlo Markov chain (MCMC) analysis of the abundance of clusters in the SPT-SZ dataset as a function of ξ and redshift at our fiducial cosmology (Bocquet et al. 2019). This analysis was conducted using the $\xi \geq 5$ sample for which we had complete optical/IR follow-up and assuming a fixed scatter of $\sigma_{\ln \zeta} = 0.2$ whose value was motivated by comparisons with X-ray observables for a large sample of SPT clusters. Motivated by observed changes in C_{SZ} in our simulations, here we explore the validity of these scaling parameters for the SPTpol 500d sample using the data itself.

In this test we replace the SPT-SZ sample above with the confirmed SPTpol 500d clusters at $\xi > 5$ and run a new abundance analysis at fixed cosmology to estimate the SPTpol 500d mass-ζ scaling relation parameters. The simulated normalization rescaling factors are applied for each survey field to make the normalizations directly comparable. We plot the results in Figure 5 along with the best fit parameters derived for SPT-SZ and SPT-ECS; the latter two results were derived using the $\xi > 5$ confirmed samples from the respective surveys. We indeed observe a shift in the redshift evolution parameter of the scaling relation $C_{SZ} = 0.87 \pm 0.17$ (compared to e.g., 0.64 ± 0.14 in SPT-SZ) but find better than 0.5σ consistency between the two surveys for the amplitude parameter $A_{SZ} = 3.95 \pm 0.23$ (4.08 ± 0.1 in SPT-SZ) and mass slope $B_{SZ} = 1.69 \pm 0.09$ (1.65 ± 0.08 for SPT-SZ).

Given the consistency in A_{SZ} and B_{SZ} for the 3 SPT surveys of significantly different depths, and the increased degeneracy between these parameters in the SPTpol 500d field given the smaller number of massive clusters observed owing to its smaller survey volume, we continue to use the best fit values from SPT-SZ for these parameters. Given the significant shift in the C_{SZ}, we adopt the newly derived value from SPTpol 500d data when reporting our cluster masses for the SPTpol 500d sample.

6.4. *Expected Purity of the SPTpol 500d Cluster Sample*

In this work, we apply a new method to estimate the cluster sample purity that significantly improves the accuracy at lower detection significances. In previous SPT works, the number of false candidates as a function of significance was estimated by running the cluster detection algorithm on sky simulations with no tSZ signal. This is sufficient for characterizing the properties of high-significance samples drawn from maps in which significant instrumental and residual atmospheric noise is present (such as the SPT-SZ sample presented in Bleem et al. 2015 and used in the cosmological analyses of de Haan et al. 2016; Bocquet et al. 2019). However, it is known that astrophysical foregrounds and the tSZ itself are not necessarily Gaussian (see e.g., recent measurements in Crawford et al. 2014; Coulton et al. 2018). The

Figure 5. Best fit mass-ζ scaling relation parameters (see Eq. 5) at our fiducial cosmology for the SPT-SZ, SPT-ECS, and SPTpol 500d cluster samples at $\xi > 5$. There is good consistency between the normalization and slope parameters (A_{SZ} and B_{SZ}, respectively) in all three surveys; additionally the shift in the redshift evolution parameter (C_{SZ}) between SPTpol and the shallower surveys is captured in our simulations discussed in Section 6.2. The smaller area surveyed in SPTpol 500d results in fewer massive clusters and increases the degeneracy between A_{SZ} and B_{SZ}; this increases the uncertainty on the recovered A_{SZ} parameter.

impact of this non-Gaussianity on the expected number of false candidates becomes more pronounced as cluster samples are produced from lower-noise data and to lower detection significance.

To illustrate this effect, we measure the number of false candidates in a simulated 500 deg² region varying the amplitude of the tSZ signal. The process by which we identify false candidates is discussed below. We plot the results of these simulations in Figure 6. As can be seen, the relative amplitude of the tSZ to the total noise can have a significant impact on the expected number of false detections, especially at lower ξ values; using tSZ-free simulations this quantity can be overestimated by factors of ~ 1.4 at $\xi_{\min} = 4$. This tension with estimations from tSZ-free simulations at low ξ is also seen empirically using optical follow-up observations as discussed in Klein et al. (2023).

In light of this effect, we update our method of prediction for the expected number of false candidates (and correspondingly sample purity) to use simulations that are statistically as close to the data as possible. We run the cluster finder on maps with tSZ included and make use of the fact that our tSZ maps are constructed with perfect correspondence to massive halos in the OuterRim Simulation. This provides us with a complete listing of all real possible cluster detections. We then estimate the purity of our cluster sample at $\xi > \xi_{\min}$ as follows:

- For each of 5 independent simulated realizations of the SPTpol 500d field (2500 square-degrees in total) we run the cluster detection algorithm. Each realization is drawn from a non-overlapping region of the simulated Compton-y map and has different
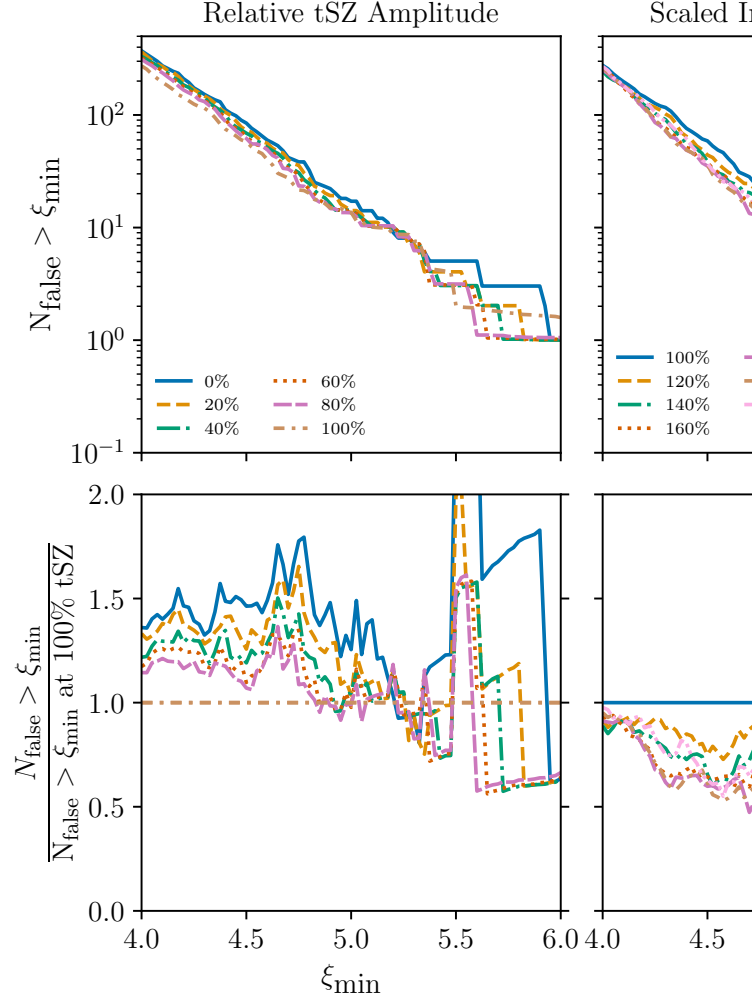
Figure 6. Variations in expected number of false detections based on differences in assumed tSZ amplitude for a 500-square-degree SPTpol-like field. In the *(top)* panel we show the expected number of false detections at $\xi > \xi_{\min}$ and in the *(bottom)* panel the ratio in the number of spurious detections compared to our reference assumptions. We vary the relative amplitude of the tSZ signal in the sky simulations, where "100%" corresponds to the maps having tSZ power which matches SPT power spectrum data (Reichardt et al. 2021) at $\ell = 3000$. Estimating the expected number of false detections through tSZ-free simulations can overestimate their counts by factors of 1.4 at low-ξ.

CMB, foreground, and noise realizations. Starting with the highest-significance cluster detection, candidates are matched to the most massive unmatched simulation halo within 2 arcmin. Matched halos are prevented from being matched with lower-significance candidates.

- A similar matching is done for 5000 random sightlines within each field footprint which determines the probability of randomly associating with a halo of a given mass within the association radius, $f_{\mathrm{R}}(M)$. Because of the strong dependence of number density on halo mass owing to the steepness of the halo mass function, it is important to include mass information when quantifying random associations.

- Next, using the observed number of candidates at $\xi > \xi_{\min}$ as well as this random association probability as a function of halo mass, we can estimate the number of false candidates above $\xi_{\min}$. Starting at the highest mass (with lowest chance of random association), we calculate the fraction of true associations to total candidates, $p(M, \xi_{\min})$, given N_{obs} associations for N_{cand} candidates at significance $> \xi_{\min}$ as

$$p(M, \xi_{\min}) = \frac{N_{\text{obs}} - N_{\text{cand}} f_{\text{R}}(M)}{N_{\text{cand}}(1 - f_{\text{R}}(M))}$$

The number of false associations, N_{FA}, at $\xi > \xi_{\min}$ and mass is then simply

$$N_{\text{FA}}(M, \xi_{\min}) = N_{\text{obs}} - p(M, \xi_{\min})N_{\text{cand}}$$

We integrate with decreasing mass, reducing the number of candidates available for random associations by the true associations calculated in previous steps, to compute the total number of false candidates. This value is given by the sum of cluster candidates unassociated with simulated halos and the number candidates falsely associated with such halos.

- We then estimate the purity of the sample in the real survey by dividing this number of false candidates by the observed number of candidates in the SPTpol sample.

We have estimated this purity under two different assumptions that we plot in Figure 7. The first uses simulations in which we have normalized the tSZ power spectrum at $\ell = 3000$ to match previous SPT results (George et al. 2015; Reichardt et al. 2021) and we adopt this as our baseline model. This tSZ model leads to approximately twice as many clusters at $\xi \geq 4$ in the simulated SPTpol field as compared to observation (likely owing to some combination of different cosmological parameters between the simulations and real data, differences from reality of the assumed tSZ profile as a function of mass and redshift, and lack of simulated correlated emission from cluster members with the tSZ signals, though we find no strong evidence for the latter in our data—see Section 7). As an alternative, we estimate the purity using simulations where we have scaled the tSZ amplitude so that the candidate count matches the observed SPTpol results. These two models agree with each other within 1 σ at $\xi > 4.5$. For reference we also plot the "tSZ-free" simulation case, which shows lower purity estimates at low ξ than the other two models.

Using Eq. 3, our baseline SZ purity model, and the subset of cluster candidates with contamination < 0.2, we estimate an overall purity of our confirmed cluster sample of 93%. We can omit use of the simulations, and estimate a purity such that Eq. 3 is satisfied and we observe consistency between the number of observed unassociated detections and predictions (as was done in Klein et al. 2023). This estimate raises the expected purity value slightly to 95% which corresponds to a $\sim 2.5\sigma$ difference between the two estimates of the purity of the full SZ candidate sample $\xi > 4$. Given the good agreement between the estimates for the confirmed portion, we quote $\sim 94\%$ as the expected purity of our confirmed

sample. To further refine our purity estimates and cluster selection modeling we are in the process of improving our simulations of cluster gas properties (Kéruzoré et al. 2023) and correlated sources of mm-wavelength contamination. This work will be important to develop in parallel to keep pace with the upcoming cluster samples from e.g., SPT-3G (Sobrin et al. 2018), and Simons Observatory (Simons Observatory Collaboration et al. 2019).

7. SYSTEMATIC EXPLORATIONS

We conduct several tests to search for potential biases in the SZ signal we use to identify SPTpol clusters and estimate their masses. Such biases may arise from correlated emission from cluster galaxies, namely synchrotron from radio sources or emission from dust associated with star formation in cluster members. Based on multi-wavelength studies of the cluster galaxy population (see e.g., Gralla et al. 2011; Alberts et al. 2016; Melin et al. 2018), synchrotron contamination is expected to arise from bright discrete sources such as active galactic nuclei in cluster central galaxies, while contamination correlated with star formation is predominately sourced through the integrated emission from a large number of cluster members. Here we use external radio imaging data as well as internal comparisons of data from the two SPTpol frequencies to search for and estimate the level of bias from these sources in our sample. We note that as this study is being conducted using an SZ-selected sample, the impact of very strong contamination (such as from a powerful radio source) that completely fills in the SZ decrement will not be accounted for in this test. Based on previous studies of optical-, IR-, and X-ray-selected systems (e.g., Lin et al. 2009; Gralla et al. 2011, 2014; Gupta et al. 2017; Mo et al. 2020; Dicker et al. 2021), such extreme sources are expected to be rare and not have a large impact on the completeness of SZ surveys at redshifts $z > 0.25$.

7.1. Radio Source Check

To assess potential contamination from radio sources below the detection threshold of SPTpol, we follow a procedure very similar to that used in Bleem et al. (2020). In this work, we use publicly available thumbnail maps from the Sydney University Molonglo Sky Survey (SUMSS, Mauch et al. 2003) at 843 MHz, while Bleem et al. (2020) used the 1.4 GHz National Radio Astronomy Observatory (NRAO) Very Large Array (VLA) Sky Survey (NVSS, Condon et al. 1998) which unfortunately does not extend as far south as the SPTpol field. Otherwise the process is identical; we summarize the analysis briefly here and refer the reader to Bleem et al. (2020) for more details.

First, we download all SUMSS postage-stamp maps that overlap with the SPTpol 500d field and reproject them onto the same pixel grid as the SPTpol maps. We make beam- and transfer-function-matched SUMSS maps for each of the SPTpol observing frequencies and scale the intensity of the maps assuming a single spectral index of -0.7 (Coble et al. 2003), and we convert the result to CMB fluctuation temperature. We produce maps of contamination to the cluster-finding by combining the single-frequency maps with the same weights as used in the cluster-finding and then filtering the result with each
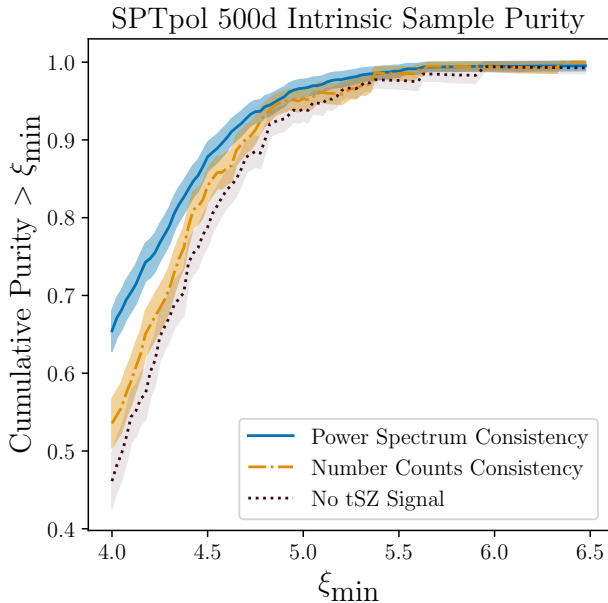
Figure 7. Expected intrinsic purity of SPTpol 500d candidate list (without considering optical/IR confirmation) under different modeling assumptions for the tSZ contribution to simulated survey maps. Overall our purity for the SPTpol sample agree within $1\,\sigma$ at $\xi > 4.5$ for our two bounding assump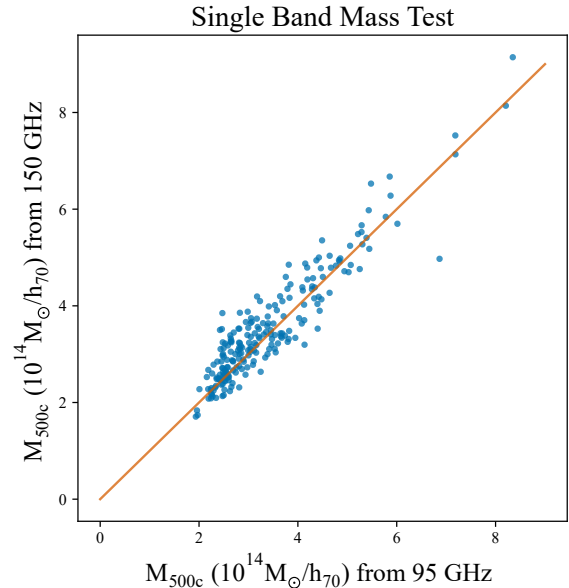tions of either (1) matching the tSZ amplitude at $\ell = 3000$ to recent power spectrum constraints (Reichardt et al. 2021) or (2) matching the identified candidate density in the 500-sq-degree footprint to that of the observed SPTpol sample. Estimating the number of false detections (and hence purity) of the sample using tSZ-free simulations significantly underestimates the sample purity at lower ξ values.

Figure 8. Masses estimated from 95 and 150 GHz data alone for 250 clusters individually detected in each band. Overall we find excellent agreement between the two, with the largest outlier, SPT-CL J2332-5358 (5.4σ, at a ratio of $M_{95\,\mathrm{GHz}}/M_{150\,\mathrm{GHz}} = 7/5$) having previously been identified as a cluster-scale strong lens of a distant star forming galaxy whose emission results in significantly reduced tSZ signal in 150 GHz data.

of the 12 matched filters. We estimate the contamination to ξ for each cluster by taking the value of the appropriate contamination map at the cluster center and dividing by the noise in the actual SPTpol combined, cluster-filtered map at that location. Because of artifacts in the SUMSS map around the bright radio source PKS 2356-61, we are not able to perform this calculation within approximately 1.5 degrees of that source. Eight of the 689 candidates in the SPTpol 500d catalog lie in this area.

The median contamination calculated in this way is $\Delta\xi_{\mathrm{med}} = 0.032$ (where $\Delta\xi$ is defined such that $\xi_{\mathrm{observed}} = \xi_{\mathrm{true}} - \Delta\xi$), or 0.8% of the $\xi = 4$ threshold value for inclusion in the catalog. Of the 681 candidates in the catalog for which we are able to perform this test, 47 ($\sim 7\%$) have a predicted contamination of greater than $\Delta\xi = 1$, and 18 ($\sim 2.5\%$) have a predicted contamination of greater than $\Delta\xi = 2$. Of the 18 candidates with a predicted contamination greater than $\Delta\xi = 2$, three are low-redshift ($z < 0.25$) systems, and two have $\xi < 4.25$, leaving only thirteen such candidates that would be included in a cosmological analysis. We flag candidates with predicated contamination $\Delta\xi > 2$ in the candidate Table 1.

7.2. *95/150 GHz Internal Consistency Test*

We can use cluster samples selected independently from the SPTpol 95 and 150 GHz data to provide an independent test of predictions from our simulations as well as to look for signatures of potential contamination to the SZ signal. This test is based on the premise that

the two key expected sources of correlated contaminating emission—synchrotron and thermal dust radiation from cluster member galaxies—should impact the recovered SZ differently at each frequency given their differing spectral energy distributions. Here we compare end-to-end predictions of the masses estimated from each frequency as cluster mass is what we are most concerned about for cosmological analyses.

Following the cluster identification procedure of Section 3 but now run on the single band maps, we detect 540 candidates (514 candidates) at $\xi > 4$ in the 95 (150 GHz) data with 250 common detections representing 221/544 confirmed systems with redshifts. Repeating the simulations above to standardize the extracted ξ values we expect the amplitude normalization factors, γ, to be 0.85 (0.78) at 95 (150) GHz relative to the full depth field, with changes in C_{SZ} between the bands as discussed above.

In Figure 8 we plot the masses estimated from each individual frequency for the matched clusters. We find the median ratio in the masses estimated from 95 and 150 GHz alone to be 0.968 ± 0.005. We attribute this offset from unity to a small misestimation of the foreground levels in the simulations, due to uncertainty in the amplitude of the uncorrelated CIB at 95 GHz (Reichardt et al. 2021), as well as our simplified modeling of the applied source cleaning, which might affect the bands differently due to the source populations in each map. For example, if we split the sample into halves based on the estimated level of radio contamination from the SUMSS data, the 95/150 GHz mass ratio is only 1% different between the two halves. Regardless, as the amplitude and other parameters of our observable-mass scaling relation will be

determined via weak lensing (e.g., Dietrich et al. 2019; Schrabback et al. 2018, 2021), small shifts of this order in our simulation calibration have negligible impact.

We next check for a redshift evolution in this relation. Splitting this joint sample at its median redshift of $z = 0.66$, we find the median ratio of the masses to be consistent, $0.97^{+0.01}_{-0.02}$ for the lower redshift half and 0.97 ± 0.01 for the higher redshift half. Restricting ourselves to the highest redshift clusters in the common sample at $z > 1$ (35 systems) we may see some evolution in the CIB contribution to the 150 GHz band, with the median ratio of 95/150 GHz masses shifting to $1.04^{+0.02}_{-0.03}$, indicating that the 150 GHz signal may be being partially filled in. This change would result in a $\sim 3.5\%$ change in the estimated masses of these highest redshift systems in our multi-band mass estimates, and is much smaller than our current best fit uncertainty in the C_{SZ} relation calibrated with weak lensing (Schrabback et al. 2021; Zohren et al. 2022) or constrained by our joint lensing+cosmological analyses (Bocquet et al. 2019).

To check for outliers in the mass comparison, we difference the masses determined by data from each frequency and divide by the mass uncertainty determined by the statistical uncertainty only (as the intrinsic Compton-y mass scatter should be the same for a given cluster measured at two different frequencies). To account for correlated scatter in the noise at each frequency from common foreground/atmospheric residuals we normalize this distribution to be a Gaussian of unit width by reducing the statistical uncertainty by 0.57, an empirical factor measured by taking a robust measure of the standard deviation of the distribution.[1] We find three clusters where the 95 and 150 GHz mass estimates differ at $> 3\sigma$. The largest discrepancy is SPT-CL J2332-5358 (5.4σ) which was previously discussed in Vanderlinde et al. (2010); Andersson et al. (2011) as a cluster that is lensing a distant star-forming galaxy. The emission from this galaxy significantly reduces the SZ signal measured at 150 GHz which lowers its 150 GHz mass estimate. This cluster is noticeable as the biggest outlier in Figure 8.

Conversely, there are two systems (SPT-CL J2337-5942, SPT-CL J0154-5619) both with 95 GHz mass estimates less than the 150 GHz mass estimates by $\sim 3.1\sigma$. These differences might be caused by co-located radio sources. Indeed for SPT-CL J2337-5942 there are 3 low-brightness SUMSS sources (7-10 mJy) within $2'$. However, for SPT-CL J0154-5619, there is no SUMSS source within $2'$ of the SPT location. Given the sample size of 221 clusters, one would expect two systems as $\geq 3.1\sigma$ outliers $\sim 7\%$ of the time.

If we look instead at clusters detected significantly in one channel but not the other ($> 7\sigma$, or 3σ above our search threshold), we find only one system, SPT-CL J2240−6117 at $z = 0.95$, detected in 95 GHz data at $\xi_{95} = 8$. Using forced-photometry on the 150 GHz detection map, we find the cluster detected at $\xi_{150} = 2.2$. Examination of a preliminary version of the first SPT-3G point source catalog (Archipley et al., in prep), reveals a dusty source detected at 220 GHz at 15 mJy within $0\!.'2$ of the 95 GHz centroid, making this system potentially

a cluster lens similar to SPT-CL J2332-5358 discussed above. The high sensitivity of the SPT-3G at 220 GHz, in combination with significantly deeper data 95 and 150 GHz, will offer more opportunities to identify instances of high-z dusty sources lensed by massive clusters.

8. THE 500-SQUARE-DEGREE SPTPOL SURVEY SZ CLUSTER CATALOG

The SPTpol 500d cluster catalog consists of 689 SZ candidates detected at $\xi > 4$. Using optical and infrared observations we have confirmed 544 of these candidates as galaxy clusters with an expected contamination of our confirmed sample of less than $\sim 6\%$. The redshifts of the confirmed sample are in the range $0.03 < z \lesssim 1.6$ and the masses are in the range $1.5 \times 10^{14} < M_{500c} < 9 \times 10^{14} M_\odot/h_{70}$. The sample has a median redshift of 0.7, median mass of $2.5 \times 10^{14} M_\odot/h_{70}$, and a spatial density of 1.18 confirmed clusters/deg^2. We provide the complete cluster candidate list as well as redshifts, estimated masses, and select optical properties for confirmed clusters in Table 1.

In Figure 9 we plot the mass-redshift distribution of the SPTpol 500d sample as compared to several other SZ-selected cluster samples. As seen in this plot, the high sensitivity of SPTpol and our extensive follow-up efforts have enabled us to confirm a large number of low-mass and high-redshift clusters; 114 of the SZ clusters are at $z > 1$ (21% of our total sample). This is a much higher fraction than the SPT-SZ (42/516 or 8%, Bleem et al. 2015) and ACT samples (222/4195, 5%, Hilton et al. 2021). We further compare select properties of the SPTpol sample to these other samples in Section 8.1. The redshift and mass reach of the SPTpol sample will enable a number of exciting studies of both cosmology (e.g., Bocquet et al. 2023) and astrophysics through studies of the mass and redshift evolution of clusters. In Figure 10 we highlight several of the new high-z clusters reported in this work.

In Figure 11 we plot the estimated selection function of the sample at $z > 0.25$. This selection function is empirically derived via propagating the $\xi \geq 4$ sample cut into mass- and redshift-space using the ξ-mass relation discussed in Section 6. The SPTpol sample is highly ($> 90\%$) complete at masses $M_{500c} > 3.5 \times 10^{14} M_\odot/h_{70}$ and $z > 0.25$. The SPTpol survey, like previous SPT works, has an increasing sensitivity to lower-mass clusters as a function of increasing redshift. As described in Huang et al. (2020), this trend arises mainly from two effects: (1) residual fluctuations from the CMB and atmosphere increase the noise in the maps at larger angular scales (2) self-similar evolution of clusters leads to hotter clusters at fixed mass at higher redshifts and hence makes higher-z systems easier to detect.

8.1. Comparison to Other Cluster Surveys

In this section, we compare the properties of the SPTpol 500d cluster sample to SZ and optical samples in the same survey region. For the SZ samples we focus on catalogs from ACT and SPT[1] and check the consistency of mass and redshift estimates for the clusters in common

---

[1] This robust standard deviation is computed using the median absolute deviation as an initial estimate, and then using Tukey's biweight to weight points, see discussion in e.g., Beers et al. (1990).

[1] While there is overlap of 22 systems with *Planck*, the typically higher redshift and lower mass SPTpol 500d sample adds no significant new information to the SPT-*Planck* comparisons previously
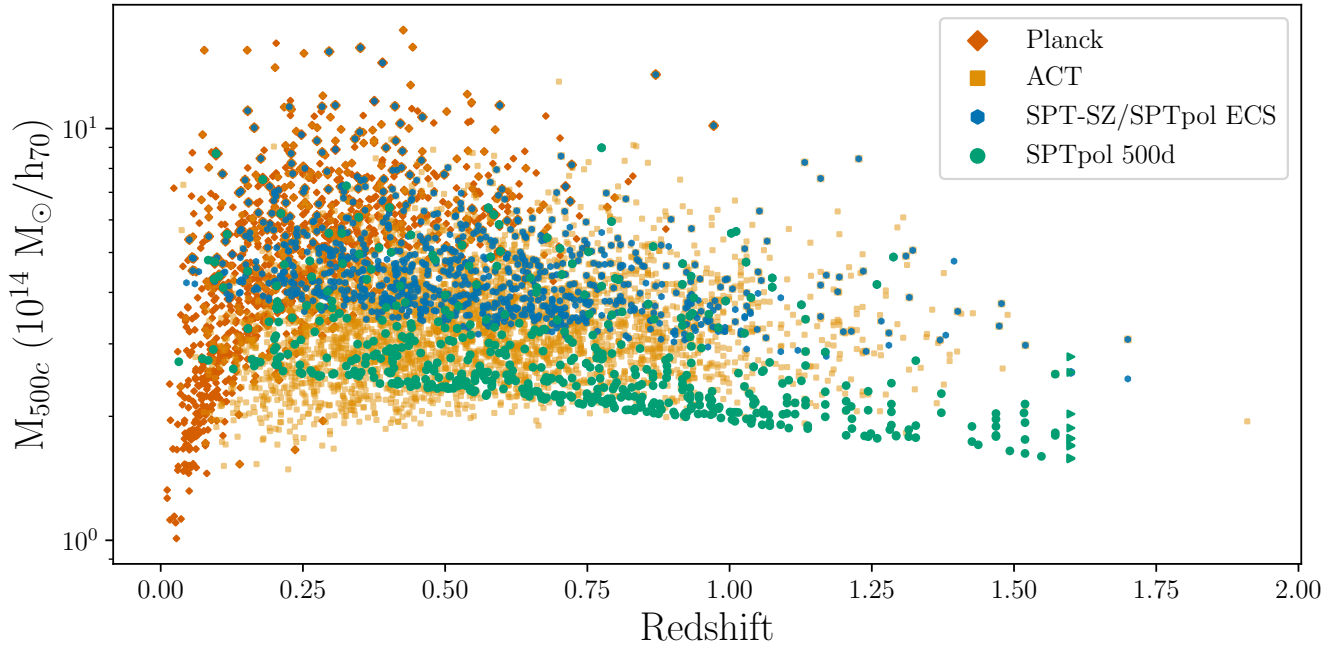
Figure 9. The mass-redshift distribution of the SPTpol 500d cluster sample. Plotted for comparison are wide-field SZ cluster samples from *Planck* (Planck Collaboration et al. 2016b), ACT (Hilton et al. 2021), and SPT-SZ/SPT-ECS (Bleem et al. 2015, 2020). The SPTpol sample consists of 544 clusters, with 21% of the sample at $z > 1$. As discussed in Section 5.2, redshifts for clusters confirmed in *Spitzer* and WISE data at $z \geq 1.6$ are considered lower limits. These systems are plotted as right-facing triangles in the plot.

between the samples. For our comparisons to the optically selected systems from DES and WISE data we check whether the SZ systems were detected and compare estimated redshifts. Detailed comparisons that more fully leverage the constraining power offered by the lower-mass SPTpol systems, such as exploring the $\lambda - M_{500c}$ relation and contamination of the optical samples (see, e.g., Bleem et al. 2020; Grandis et al. 2021), are reserved for future work.

8.1.1. *SPT-SZ*

There are 118 SPT-SZ cluster candidates detected at $\xi > 4.5$ that fall within the SPTpol 500d footprint and 113 of these candidates in unmasked regions (with masking owing to nearby bright point sources as discussed in Section 2.1).[2] Using an association radius of $3'$ to identify matching detections, we find that 97 of these candidates have matches in the SPTpol catalog, with median ratio of the significance of cluster detection between SPTpol/SPT-SZ being 1.7, and a median spatial separation of $0\overset{\prime}{.}26$. As discussed in Klein et al. (2023), for 5 of these matched systems, the improved DES and WISE follow-up data allow us to confirm them and provide redshifts. Of the 16 unmatched SPT-SZ candidates ranging in $4.5 < \xi < 5.2$ (median $\xi = 4.7$), only one—SPT-CL J2232-6151, $\xi = 5.04, z = 0.79$—was reported confirmed by follow-up optical and infrared observations in Bleem et al. (2015). This is consistent with the es-

undertaken in (Bleem et al. 2020) for the SPT-SZ and SPT-ECS samples.
[2] We note the point source mask between SPT-SZ and SPTpol differs slightly owing to survey noise and source variability as each was constructed using sources brighter than $\sim$6 mJy as measured in the maps used for cluster identification.

timate for the purity of the optically confirmed sample, using the framework developed in this paper. There are 597 cluster candidates at $\xi > 4$ in SPTpol that are not found in SPT-SZ, with 448 (385) of these having optical contamination values less than 0.2 (0.05). Of these systems, 123 are at $\xi > 5.5$ where the raw SPTpol candidate list is $> 99\%$ pure (Section 6.4).

Comparing the estimated masses we find the median ratio of the masses of common systems in SPTpol/SPT-SZ to be $1.025^{+0.01}_{-0.04}$. A plot showing the masses of the common systems within $\delta_z = 0.1$ (this cut removes 5 systems at $z > 0.85$) is shown in Figure 12. We apply the redshift cut here and in the other SZ sample comparisons in this section to avoid highlighting differences in mass that would purely arise from the masses being estimated at significantly different redshifts.

8.1.2. *SPTpol 100d*

Next, we compare the SPTpol 500d sample to the sample produced from the SPTpol 100d survey (Huang et al. 2020). This sample consists of 89 clusters detected at $\xi > 4.6$. Of these 89 systems, 86 are in the non-point source masked region and 73 are in the SPTpol 500d sample. The matched candidates have a median spatial separation of $0\overset{\prime}{.}22$. Using our updated scaling-relation parameters discussed in Section 6, we find the median ratio of the masses of clusters in SPTpol 500d/SPTpol 100d to be 1.02 ± 0.02 for systems within $\delta_z = 0.1$. This comparison was conducted using 66 systems, which excludes from the 73 matches above 1 unconfirmed candidate, 2 newly confirmed systems in this work, and 4 systems with updated *Spitzer* redshifts that shifted them outside this range. We plot the SPTpol 500d and 100d masses against each other in the middle panel of Figure
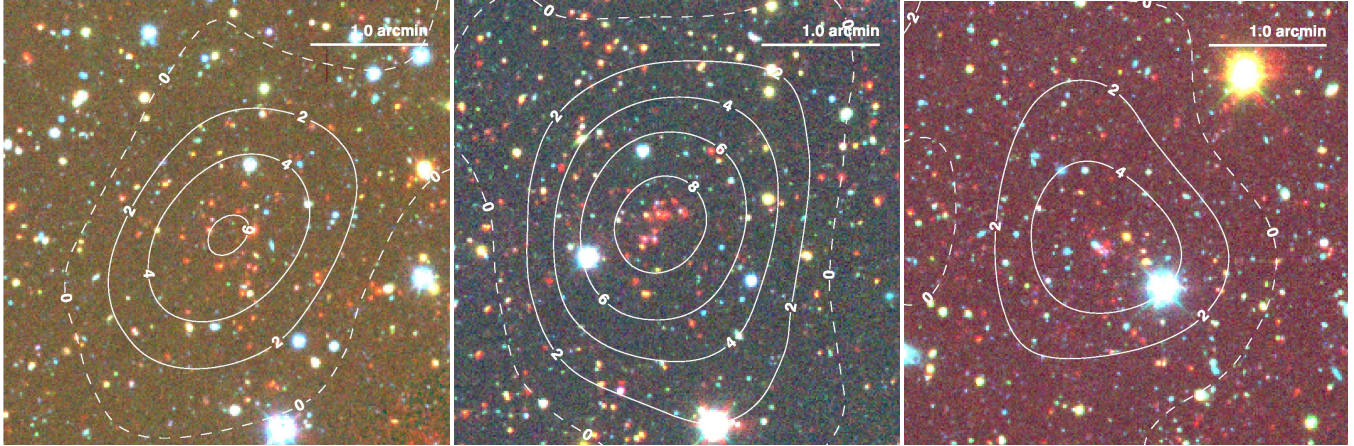
Figure 10. Three of the high-z clusters discovered in the SPTpol 500d survey. From left to right, SPT-CL J0128-5222 at $\xi = 6$ and $z = 1.4 \pm 0.07$, SPT-CL J0122-5801 at $\xi = 9$ and $z \gtrsim 1.6$, and SPT-CL J0116-5039 at $\xi = 6$ and $z \gtrsim 1.6$. The SZ detection contours are overlaid on RGB images from *Spitzer* [3.6] and DES i- and g- band data. Star formation—as traced by bluer emission correlated with the galaxy overdensities—is prominently visible in some of these high-z cluster galaxies, highlighting the ability of this sample to probe clusters in the high-z transitional era between active star formation and passive galaxy evolution. SPT-CL J0122-5801 is one of the systems tagged as having multiple overdensities along the line-of-sight, with an additional foreground system of $\lambda = 16, z = 0.6$, and $f_{cont} = 0.05$. The deep high-resolution *Spitzer* data allow us to detect the more significant distant background cluster.
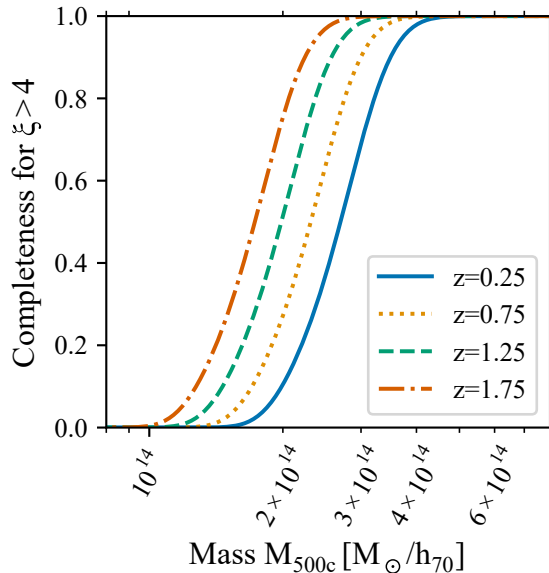
Figure 11. Expected completeness of the $\xi > 4$ SPTpol sample as a function of M_{500c} at several redshifts. The sample is expected to be $> 90\%$ complete at $M_{500c} > 3.5 \times 10^{14}$ $M_\odot/h_{70}$ at $z > 0.25$. At lower redshifts the atmospheric filtering removes larger angular-scale cluster signals leading the sample to be increasingly incomplete at $z < 0.25$.

12. The ξ values of unmatched SPTpol 100d cluster candidates (8/13 confirmed with redshifts) range from 4.6 to 6.2.

8.1.3. *ACT*

Finally, repeating the matching exercise with the ACT cluster catalog of Hilton et al. (2021), we find 141 ACT cluster candidates detected at ACT signal-to-noise > 4 fall within the SPTpol 500d footprint and 132 in the non-

masked region. Using the same $3'$ matching radius as for SPT-SZ, we find 108 of these candidates have matches in the SPTpol sample, with a median ratio of SPTpol/ACT detection signal-to-noise of 1.66 and median spatial separation of $0\rlap{.}'33$. There are 24 candidates not matched, ranging in ACT detection significance from 4.1 to 5.4σ and having a median reported mass of $M_{500c} = 2 \times 10^{14}$ $M_\odot/h_{70}$.

Reversing the question, there are 389 SPTpol candidates at $\xi > 4$ and north of $\delta = -60$ (the southernmost extent of the ACT sample) not found in the ACT sample, with 290 having been confirmed by optical/IR follow-up observations. The ξ values of these unmatched confirmed clusters lie in the range $4 < \xi < 9$ with a median mass of $M_{500c} = 2.4 \times 10^{14}$ $M_\odot/h_{70}$. Of these systems, 64 are at $\xi > 5.5$, a significance above which candidates are highly pure, independent of optical follow-up (see Figure 7).

A more detailed comparison of the relative completeness of the ACT and SPTpol samples will require careful investigations of the cluster confirmation procedure as well as masking and spatial variations in the noise levels in the ACT maps. Hilton et al. (2021) also did not report a full candidate list, rather only cluster candidates confirmed by their optical/infrared analysis, which further complicates this comparison. The dominant source of follow-up confirmation and redshifts for ACT clusters in the SPTpol region was the redMaPPer algorithm run on DES data (which has excellent agreement with MCMF at $z < 1$, see Figure 14), followed by the zCluster algorithm run on DESI Legacy Survey data (Dey et al. 2019) which includes optical grz photometry combined with WISE *W1* and *W2* channel data, and then previously reported cluster redshifts from SPT and the literature. Given the challenges of confirming high-redshift clusters, we would naturally expect most variation in the confirmation fraction of this portion of the sample.

Moving on from the identification of systems, we now
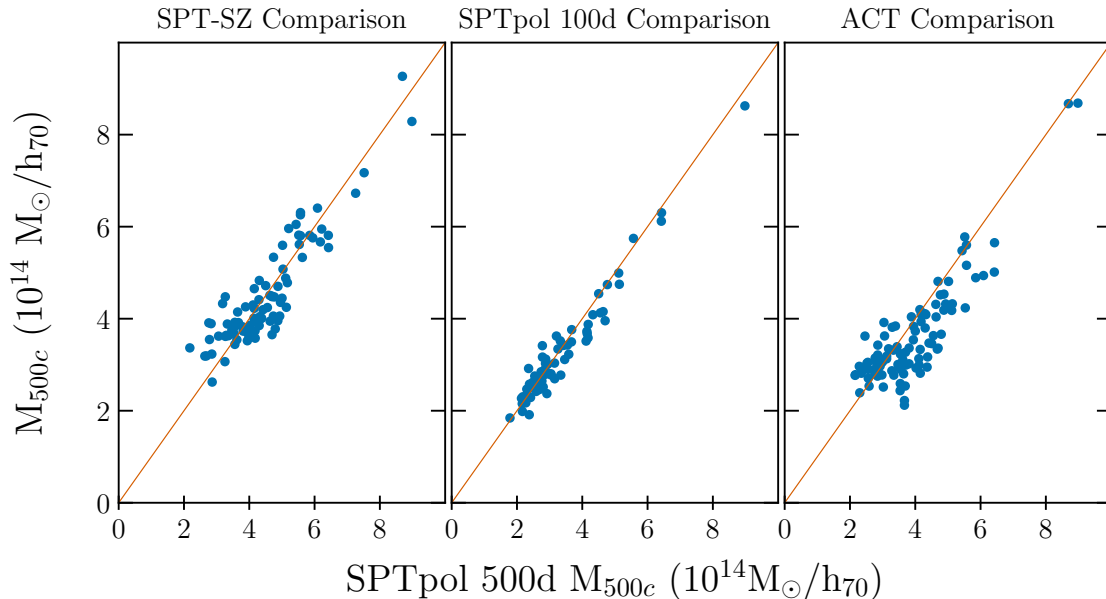
Figure 12. Comparisons of mass estimates for clusters from SPTpol 500d that are in common with systems in SPT-SZ (Bleem et al. 2015), SPTpol 100d (Huang et al. 2020), and ACT (Hilton et al. 2021). Over-plotted is a line representing a one-to-one relationship. As discussed in Section 8.1, we find good agreement between the 3 SPT surveys, with the median ratio of masses of SPTpol 500d/SPT-SZ to be $1.02^{+0.02}_{-0.04}$ and SPTpol 500d/SPTpol 100d to be 1.02 ± 0.02. We do note a small (2.3σ) difference in the normalization of the ACT and SPT masses, finding the ratio of masses from SPTpol 500d/ACT $=1.07 \pm 0.03$ (differing from the consistency shown in Hilton et al. 2021), but a stronger test of any cross experiment mass calibration differences will come when comparing weak-lensing calibrated samples in future works.

compare the estimated masses. The ACT collaboration uses a different procedure than SPT for estimating the masses of clusters. Following initial cluster identification, a central Compton-y parameter, y_o, is measured for each candidate using a $2'.4$ matched filter. This central value is then corrected for the mismatch as a function of cluster mass and redshift between the expected cluster profile and that adopted for the matched filter. The Arnaud et al. (2010) pressure-mass scaling relation, statistical and assumed intrinsic scatter in y_o, and the Tinker et al. (2008) mass function (computed at the same fiducial cosmology we adopt in this work) are then used to compute the probability distribution, $P(M_{500c}|\ y_o, z)$. The maximum in this distribution is assigned as the cluster mass. This mass is further corrected by a value of 0.71 ± 0.07 using the weak lensing λ- mass calibration of McClintock et al. (2019); these masses are reported as $M_{500c}^{\rm Cal}$ in the ACT catalog.

A plot showing the masses of the common SPTpol 500d/ACT systems within $\delta_z = 0.1$ (100 clusters, 8 $z > 0.96$ systems excluded for redshift differences) is shown in Figure 12. Comparing these masses, we find the ratio of SPTpol/ACT masses to be 1.07 ± 0.03. We find this ratio to be consistent with the results comparing the median mass ratio of 362 common clusters between SPT-SZ and ACT ($1.06^{+0.02}_{-0.006}$). This difference in normalization is larger than the 1.027 ± 0.012 reported in Hilton et al. (2021). That work measured this ratio using 228 common clusters with ACT signal-to-noise > 6 and the full SPT-SZ sample at $\xi > 4.5$; we recover the same mass ratio when applying ACT's thresholds. We note given the significant differences in how the mass-scaling relation parameters are determined—SPT's via

the abundance matching of our sample to a fiducial cosmology versus ACT's adoption of a weak lensing calibration via cross matching with the DES redMaPPER calibration (the latter scaling known to be biased by projection effects, especially at lower masses Bleem et al. 2020; Grandis et al. 2021)— that the agreement here between SPT and ACT masses is not a strong cross check of the mass estimation techniques.

8.1.4. *Optically Selected Cluster Samples*

We compare the SPTpol 500d sample to two optical samples produced by algorithms that adopt complementary approaches to finding clusters in photometric data. The first sample, the DES redMaPPer[1] sample (hereafter RM), was constructed by running the RM algorithm (Rykoff et al. 2016) on DES Y3 data (Abbott et al. 2018). RM identifies clusters by locating spatial over-densities of red-sequence galaxies. The full Y3 RM sample consists of 869,335 systems with a weighted galaxy-count mass proxy $\lambda > 5$ and redshifts $0.1 < z < 0.95$. The second sample, produced by Wen & Han (2022, hereafter WH), was constructed using DES and WISE (Wright et al. 2010) data; clusters in this sample were identified as over-densities of stellar mass in photometric redshift slices. This sample contains 151,244 clusters from $0.1 < z < 1.5$ above a detection signal-to-noise of 5. The inclusion of IR data from WISE greatly extends the redshift reach of the catalog compared to that of RM.

Here, as the spatial density of the optical systems is much greater than that of the SZ surveys, we define a cluster-match between samples as having a counterpart

[1] Version 6.4.22+2
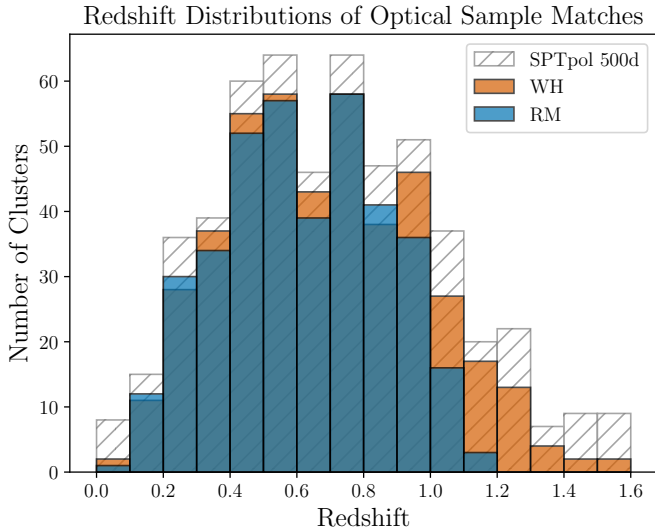
Figure 13. Redshift distribution of optical/IR cluster sample matches from RM and WH to the full SPTpol 500d sample. Matches are plotted at the SPTpol redshifts. Overall, the RM sample recovers 70% of the SPTpol sample and the WH sample recovers 81%; many of the lower-redshift clusters not recovered in RM are near regions masked in their analysis.

within $2'$ and within $\delta_z = 0.1 \times (1 + z)$. When multiple systems are found, we adopt the closest match in redshift as the cluster counterpart. In total we match 379/544 (70%) of the SZ clusters using RM and 441/544 (81%) using WH. We plot the redshift distribution of the SPTpol 500d sample and its matched counterparts in the wide-field optical/IR cluster searches in Figure 13.

We next compare the redshift consistency for estimates from the different samples. We relax our matching criteria to include optical systems matched within $2'$ for candidates which did not have a good spatial and redshift match to allow us to check for instances where RM and WH may have detected clusters not already captured in our analysis or identified the same optical system at a discrepant redshift. To account for the fact that there are candidates for which we have identified lower-significance galaxy excesses along the line-of-sight below our optical confirmation threshold, we assign these unconfirmed systems the redshifts of these over-densities for this exercise only. Finally, it is important to remember that the redshift estimates we are comparing here were conducted using similar or identical datasets (DES Years 3 or 6, with WISE for some a subset of the high-z clusters), though with different methods (photo-z versus red-sequence) and with different spectroscopic calibration samples.

As shown in Figure 14, overall there is good agreement in the measured redshifts for matching systems. We find $\sigma_{\delta_z}/(1 + z) = 0.009$ (0.014) for RM (WH) at $z < 1$ for clusters we deem a spatial/redshift match, with the blind RM search systematically underestimating matched redshifts at $z > 0.9$ (beyond its stated redshift reliability). At $z > 1$, the scatter broadens for the difference between SPTpol 500d and WH to $\sigma_{\delta_z}/(1 + z) = 0.04$. Given their small number of high-z spectroscopic calibrators, WH do not report redshift uncertainties for these highest-z systems. The optical/IR systems from the wide-field
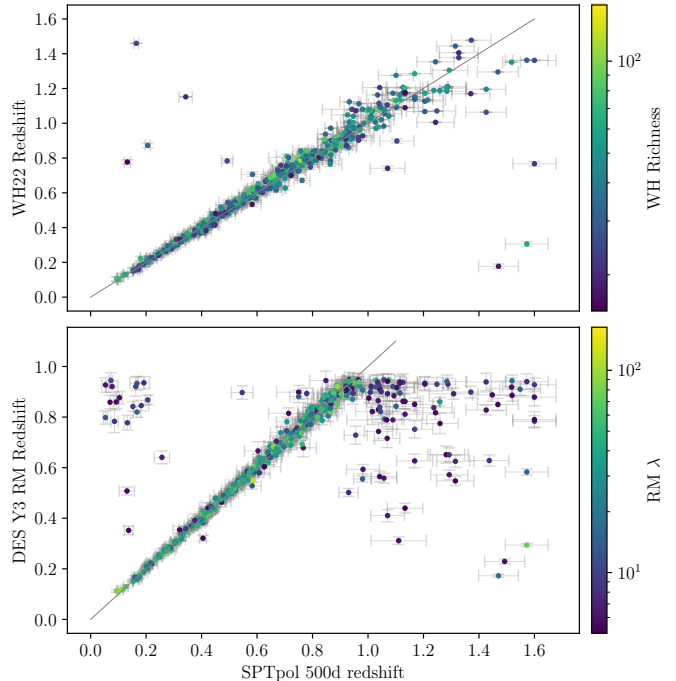

Figure 14. Comparison of redshifts of systems from wide-field cluster searches associated with SPTpol 500d candidates by a (1) redshift/spatial proximity match or (2) only a spatial-proximity match if no systems fell within the redshift association cut (for more details of the matching process see Section 8.1.4). In the *top* panel are shown matches to the Wen & Han (2022) optical/IR sample and in the *bottom* panel to the DES RM sample constructed using the DES Y3 dataset. Note that redshift uncertainties are not provided at $z > 1$ for the WH sample. Plotted in gray on each panel is a line representing a one-to-one relationship. The WH (RM) sample has good spatial and redshift matches for 81% (70%) of the SPTpol sample. Systems with redshifts that significantly differ between SPTpol and the wide-field optical/IR searches have typically low wide-field survey richnesses, and are likely spurious associations with the SZ detections. This highlights the importance of accounting for chance associations when matching galaxy over-densities to SZ detections.

searches that have discrepant redshifts are typically low-richness and thus likely spurious associations; such discrepant associations are particularly noticeable for high-z SPT clusters at redshifts higher than the RM search. This highlights the importance of quantifying such false association probabilities (Klein et al. 2018; Bleem et al. 2020; Hilton et al. 2021) when mapping associations between optical galaxy over-densities and SZ clusters.

9. CONCLUSIONS

In this work we described the production of a new sample of galaxy clusters detected by their SZ signature in the SPTpol 500d survey. We implemented several important improvements to our cluster catalog production and characterization processes. These improvements include the subtraction of moderate signal-to-noise emissive sources from the temperature maps before cluster finding to reduce the number of spurious candidates, improved cluster simulations and sample purity estimation techniques, and new tests to identify potential biases to our recovered SZ signal.

The new SPTpol 500d sample consists of 689 galaxy cluster candidates detected at $\xi > 4$. These candidates

were selected from coadded maps of depths 5.3 (11.7) μK$_{\rm CMB}$-arcmin at 150 (95) GHz that were created from > 4000 observations of the SPTpol 500d field. To confirm candidates as clusters, we search optical and IR observations from DECam, WISE, and *Spitzer* with the MCMF algorithm and a related IR-based code to identify significant red-sequence and/or IR galaxy over-densities at the candidate locations. We probabilistically confirm 544 of these candidates as galaxy clusters, with an expected confirmed sample purity of $\sim 94\%$. The SPTpol 500d cluster sample has a median mass of $2.5 \times 10^{14} M_\odot/h_{70}$, a median redshift of $z = 0.7$, and is expected to be $> 90\%$ complete at $M_{500c} > 3.5 \times 10^{14}~M_\odot/h_{70}$ at $z > 0.25$. A significant fraction of the systems are at high z, with 114 clusters at $z > 1$.

Masses are estimated for confirmed clusters via a $\xi-$mass scaling relation whose parameters are determined by matching the abundance of observed clusters to a fixed ΛCDM cosmology. Using simulations to relatively calibrate this relation for three independently extracted cluster catalogs from data of variable survey depth—the SPT-SZ (Bleem et al. 2015), SPTpol 100d (Huang et al. 2020), and SPTpol 500d cluster samples—we find excellent agreement for the masses of clusters in common between SPTpol 500d and the other surveys. We have used both external datasets and internal checks to test for contamination of the SZ signal that could bias these mass estimates. These investigations include an assessment of potential radio contamination via extrapolating data from the 843 MHz Sydney University Molonglo Sky Survey at cluster locations. This analysis predicts a median contamination of $\Delta\xi_{\rm med} = 0.032$ and that $\sim 7\%$ of candidates could have a predicted contamination of greater than $\Delta\xi = 1$. However, this prediction requires a significant extrapolation from low-frequency data to the SPT bands, and may be an overestimate. Internal tests comparing masses for clusters detected at 95 and 150 GHz alone show—with the exception of a small number of clusters—insignificant radio or CIB contamination to the SZ signal.

Matching to previous high-resolution SZ surveys in the region, we find 73, 97, and 141 clusters in common with the SPTpol 100d, SPT-SZ, and ACT (Hilton et al. 2021) cluster samples, respectively. These clusters are detected at $\sim 1.7\times$ higher signal-to-noise in SPTpol data than SPT-SZ or ACT data. We find good agreement between the masses of systems in common between the SPT surveys and that the SPT masses are $\sim 1.07\times$ higher than the ACT reported masses for the common clusters. A spatial-redshift match to the wide-field optical/IR cluster samples of DES Y3 redMaPPer (Rykoff et al. 2016) and the sample produced by Wen & Han (2022) finds matches for 70-81% of the SPTpol sample, but also highlights the importance of probabilistic confirmation techniques to avoid spurious associations.

While this is the final cluster sample from the SPTpol collaboration, a number of ongoing astrophysical and cosmological studies are underway that take advantage of its unique low-mass and high-redshift capabilities. Although surveys like SPT-3G (Sobrin et al. 2018), Simons Observatory (Simons Observatory Collaboration 2019), and CMB-S4 (CMB-S4 Collaboration et al. 2019) will in the future surpass the SPTpol survey with deeper and wider data sets, the work here—particularly the explo-

rations of emissive sources, simulation modeling of SZ cluster samples, and internal and external contamination tests—pave the way for maximizing the potential of the SPTpol and these future surveys for SZ cluster science.

As a final note— We also release the coadded mm-wave maps and associated data products used to produce this sample. The maps and supporting products are available at https://pole.uchicago.edu/public/data/sptpol_500d_clusters/index.html, and the NASA LAMBDA website. An interactive sky server with the SPTpol maps and Dark Energy Survey data release 2 images is also available at NCSA https://skyviewer.ncsa.illinois.edu.

REFERENCES

Abbott, T. M. C., Abdalla, F. B., Allam, S., et al. 2018, The Astrophysical Journal Supplement Series, 239, 18

Abbott, T. M. C., Adamów, M., Aguena, M., et al. 2021, ApJS, 255, 20

Alberts, S., Pope, A., Brodwin, M., et al. 2016, The Astrophysical Journal, 825, 72

Anbajagane, D., Chang, C., Jain, B., et al. 2022, MNRAS, 514, 1645

Andersson, K., Benson, B. A., Ade, P. A. R., et al. 2011, ApJ, 738, 48

Arnaud, M., Pratt, G. W., Piffaretti, R., et al. 2010, A&A, 517, A92

Ashby, M. L. N., Stern, D., Brodwin, M., et al. 2009, ApJ,, 701, 428

Ashby, M. L. N., Stanford, S. A., Brodwin, M., et al. 2013, ApJS, 209, 22

Austermann, J. E., Aird, K. A., Beall, J. A., et al. 2012, in Society of Photo-Optical Instrumentation Engineers (SPIE) Conference Series, Vol. 8452, Society of Photo-Optical Instrumentation Engineers (SPIE) Conference Series

Bayliss, M. B., Ruel, J., Stubbs, C. W., et al. 2016, ApJS, 227, 3

Beers, T. C., Flynn, K., & Gebhardt, K. 1990, AJ, 100, 32

BICEP/Keck Collaboration and SPTpol Collaboration, Ade, P. A. R., Ahmed, Z., et al. 2021, Phys. Rev. D, 103, 022004

Bleem, L. E., Stalder, B., de Haan, T., et al. 2015, ApJS, 216, 27

Bleem, L. E., Bocquet, S., Stalder, B., et al. 2020, ApJS, 247, 25

Bocquet, S., Dietrich, J. P., Schrabback, T., et al. 2019, ApJ, 878, 55

Bocquet, S., Grandis, S., Bleem, L. E., et al. 2023, arXiv e-prints, arXiv:2310.12213

Bruzual, G., & Charlot, S. 2003, MNRAS, 344, 1000

Calabretta, M. R., & Greisen, E. W. 2002, A&A, 395, 1077

Cavaliere, A., & Fusco-Femiano, R. 1976, A&A, 49, 137

Chaubal, P. S., Reichardt, C. L., Gupta, N., et al. 2022, ApJ, 931, 139

CHEX-MATE Collaboration, Arnaud, M., Ettori, S., et al. 2021, A&A, 650, A104

Chiu, I., Mohr, J. J., McDonald, M., et al. 2018, MNRAS, 478, 3072

CMB-S4 Collaboration, Abazajian, K., Addison, G., et al. 2019, arXiv e-prints, arXiv:1907.04473

Coble, K., Ade, P. A. R., Bock, J. J., et al. 2003, ArXiv Astrophysics e-prints, arXiv:astro-ph/0301599

Condon, J. J., Cotton, W. D., Greisen, E. W., et al. 1998, AJ, 115, 1693

Costanzi, M., Saro, A., Bocquet, S., et al. 2021, Phys. Rev. D, 103, 043522

Coulton, W. R., Aiola, S., Battaglia, N., et al. 2018, J. Cosmology Astropart. Phys., 2018, 022

Crawford, T. M., Schaffer, K. K., Bhattacharya, S., et al. 2014, ApJ, 784, 143

Crites, A. T., Henning, J. W., Ade, P. A. R., et al. 2015, ApJ, 805, 36

de Haan, T., Benson, B. A., Bleem, L. E., et al. 2016, ApJ, 832, 95

De Zotti, G., Ricci, R., Mesa, D., et al. 2005, A&A, 431, 893

Dey, A., Schlegel, D. J., Lang, D., et al. 2019, AJ, 157, 168

Dicker, S. R., Battistelli, E. S., Bhandarkar, T., et al. 2021, MNRAS, 508, 2600

Dietrich, J. P., Bocquet, S., Schrabback, T., et al. 2019, MNRAS, 483, 2871

Euclid Collaboration, Adam, R., Vannier, M., et al. 2019, Astronomy and Astrophysics, 627, A23

Everett, W. B., Zhang, L., Crawford, T. M., et al. 2020, ApJ, 900, 55

Fazio, G. G., Hora, J. L., Allen, L. E., et al. 2004, ApJS, 154, 10

Flaugher, B., Diehl, H. T., Honscheid, K., et al. 2015, AJ, 150, 150

Flender, S., Bleem, L., Finkel, H., et al. 2016, ApJ, 823, 98

Flores, A. M., Mantz, A. B., Allen, S. W., et al. 2021, MNRAS, 507, 5195

George, E. M., Reichardt, C. L., Aird, K. A., et al. 2015, ApJ, 799, 177

Ghirardini, V., Bulbul, E., Kraft, R., et al. 2021, ApJ, 910, 14

Gladders, M. D., & Yee, H. K. C. 2000, AJ, 120, 2148

Gonzalez, A. H., Gettings, D. P., Brodwin, M., et al. 2019, The Astrophysical Journal Supplement Series, 240, 33

Gralla, M. B., Gladders, M. D., Yee, H. K. C., & Barrientos, L. F. 2011, ApJ, 734, 103

Gralla, M. B., Crichton, D., Marriage, T. A., et al. 2014, MNRAS, 445, 460

Grandis, S., Mohr, J. J., Costanzi, M., et al. 2021, MNRAS, 504, 1253

Gupta, N., Saro, A., Mohr, J. J., et al. 2017, MNRAS, 467, 3737

Gupta, N., Reichardt, C. L., Ade, P. A. R., et al. 2019, MNRAS, 490, 5712

Heitmann, K., Finkel, H., Pope, A., et al. 2019, ApJS, 245, 16

Hennig, C., Mohr, J. J., Zenteno, A., et al. 2017, MNRAS, 467, 4015

Henning, J. W., Sayre, J. T., Reichardt, C. L., et al. 2018, ApJ, 852, 97

Hilton, M., Hasselfield, M., Sifón, C., et al. 2018, ApJS, 235, 20
Hilton, M., Sifón, C., Naess, S., et al. 2021, ApJS, 253, 3
Huang, N., Bleem, L. E., Stalder, B., et al. 2020, AJ, 159, 110
Keisler, R., Reichardt, C. L., Aird, K. A., et al. 2011, ApJ, 743, 28
Kéruzoré, F., Bleem, L. E., Buehlmann, M., et al. 2023, arXiv e-prints, arXiv:2306.13807
Khullar, G., Bleem, L. E., Bayliss, M. B., et al. 2019, ApJ, 870, 7
Khullar, G., Bayliss, M. B., Gladders, M. D., et al. 2022, ApJ, 934, 177
Kim, K. J., Bayliss, M. B., Noble, A. G., et al. 2023, ApJ, 955, 32
Klein, M., Mohr, J. J., Desai, S., et al. 2018, MNRAS, 474, 3324
Klein, M., Grandis, S., Mohr, J. J., et al. 2019, MNRAS, 488, 739
Klein, M., Mohr, J. J., Bocquet, S., et al. 2023, arXiv e-prints, arXiv:2309.09908
Laureijs, R., Amiaux, J., Arduini, S., et al. 2011, arXiv e-prints, arXiv:1110.3193
Lin, Y., Partridge, B., Pober, J. C., et al. 2009, ApJ, 694, 992
Mainzer, A., Bauer, J., Cutri, R. M., et al. 2014, ApJ, 792, 30
Mauch, T., Murphy, T., Buttery, H. J., et al. 2003, MNRAS, 342, 1117
McClintock, T., Varga, T. N., Gruen, D., et al. 2019, MNRAS, 482, 1352
McDonald, M., Allen, S. W., Bayliss, M., et al. 2017, ApJ, 843, 28
Melin, J.-B., Bartlett, J. G., Cai, Z.-Y., et al. 2018, A&A, 617, A75
Melin, J.-B., Bartlett, J. G., & Delabrouille, J. 2006, A&A, 459, 341
Mo, W., Gonzalez, A., Brodwin, M., et al. 2020, ApJ, 901, 131
Muzzin, A., Wilson, G., Demarco, R., et al. 2013, ApJ, 767, 39
Navarro, J. F., Frenk, C. S., & White, S. D. M. 1997, ApJ, 490, 493
Oke, J. B. 1974, ApJS, 27, 21
Olivares, V., Su, Y., Nulsen, P., et al. 2022, MNRAS, 516, L101
Orlowski-Scherer, J., Di Mascolo, L., Bhandarkar, T., et al. 2021, A&A, 653, A135
Papovich, C. 2008, ApJ, 676, 206
Papovich, C., Shipley, H. V., Mehrtens, N., et al. 2016, ApJS, 224, 28
Piffaretti, R., Arnaud, M., Pratt, G. W., Pointecouteau, E., & Melin, J.-B. 2011, A&A, 534, A109
Planck Collaboration, Ade, P. A. R., Aghanim, N., et al. 2016a, A&A, 594, A24
—. 2016b, A&A, 594, A27
Planck Collaboration, Aghanim, N., Akrami, Y., et al. 2020, A&A, 641, A6
Raghunathan, S., Patil, S., Baxter, E., et al. 2019, Phys. Rev. Lett., 123, 181301
Reichardt, C. L., Stalder, B., Bleem, L. E., et al. 2013, ApJ, 763, 127
Reichardt, C. L., Patil, S., Ade, P. A. R., et al. 2021, ApJ, 908, 199

Robitaille, T. 2019, APLpy v2.0: The Astronomical Plotting Library in Python
Robitaille, T., & Bressert, E. 2012, APLpy: Astronomical Plotting Library in Python, Astrophysics Source Code Library, ascl:1208.017
Ruppin, F., McDonald, M., Hlavacek-Larrondo, J., et al. 2023, ApJ, 948, 49
Rykoff, E. S., Koester, B. P., Rozo, E., et al. 2012, ApJ, 746, 178
Rykoff, E. S., Rozo, E., Hollowood, D., et al. 2016, The Astrophysical Journal Supplement Series, 224, 1
Salpeter, E. E. 1955, ApJ, 121, 161
Salvati, L., Saro, A., Bocquet, S., et al. 2022, ApJ, 934, 129
Sayre, J. T., Reichardt, C. L., Henning, J. W., et al. 2020, Phys. Rev. D, 101, 122003
Schlafly, E. F., Meisner, A. M., & Green, G. M. 2019, The Astrophysical Journal Supplement Series, 240, 30
Schrabback, T., Applegate, D., Dietrich, J. P., et al. 2018, MNRAS, 474, 2635
Schrabback, T., Bocquet, S., Sommer, M., et al. 2021, MNRAS, 505, 3923
Simons Observatory Collaboration. 2019, Journal of Cosmology and Astro-Particle Physics, 2019, 056
Simons Observatory Collaboration, Ade, P., Aguirre, J., et al. 2019, Journal of Cosmology and Astro-Particle Physics, 2019, 056
Sobrin, J. A., Ade, P. A. R., Ahmed, Z., et al. 2018, in Society of Photo-Optical Instrumentation Engineers (SPIE) Conference Series, Vol. 10708, Proc. SPIE, 107081H
Somboonpanyakul, T., McDonald, M., Noble, A., et al. 2022, AJ, 163, 146
Sorba, R., & Sawicki, M. 2010, ApJ, 721, 1056
Strazzullo, V., Pannella, M., Mohr, J. J., et al. 2019, A&A, 622, A117
Sunyaev, R. A., & Zel'dovich, Y. B. 1972, Comments on Astrophysics and Space Physics, 4, 173
Tinker, J., Kravtsov, A. V., Klypin, A., et al. 2008, ApJ, 688, 709
Vanderlinde, K., Crawford, T. M., de Haan, T., et al. 2010, ApJ, 722, 1180
Vazdekis, A., Sánchez-Blázquez, P., Falcón-Barroso, J., et al. 2010, MNRAS, 404, 1639
Wen, Z. L., & Han, J. L. 2022, MNRAS, 513, 3946
Wright, E. L., Eisenhardt, P. R. M., Mainzer, A. K., et al. 2010, AJ, 140, 1868
Wu, W. L. K., Mocanu, L. M., Ade, P. A. R., et al. 2019, ApJ, 884, 70
Zohren, H., Schrabback, T., Bocquet, S., et al. 2022, A&A, 668, A18
Zubeldia, Í., & Challinor, A. 2019, MNRAS, 489, 401
Zubeldia, Í., Chluba, J., & Battye, R. 2023, MNRAS, 522, 5123
Zubeldia, Í., Rotti, A., Chluba, J., & Battye, R. 2021, MNRAS, 507, 4852

BLEEM ET AL.

Table 1
Galaxy Cluster Candidates at $\xi > 4$ in the SPTpol 500d Survey

SPT ID	R.A. (J2000)	Decl. (J2000)	Best		Redshift	$\mathbf{M}_{500c}$ $(10^{14}h_{70}^{-1}M_\odot)$	λ	*Spitzer*	Notes
			ξ	θ_c					
SPT-CL J0000−6020	0.0348	−60.3367	7.15	0.25	0.76±0.02	$3.15^{+0.43}_{-0.52}$	51±8	0	-
SPT-CL J0000−5825	0.0855	−58.4250	4.03	0.50	0.74±0.03	$2.14^{+0.33}_{-0.47}$	30±7	0	-
SPT-CL J0000−6301	0.1269	−63.0190	4.44	0.25	0.245±0.008	$2.67^{+0.44}_{-0.57}$	55±9	0	-
SPT-CL J0000−6121	0.1890	−61.3538	4.01	0.25	-	-	-	0	-
SPT-CL J0000−5748	0.2479	−57.8083	14.58	0.25	0.702	$5.12^{+0.56}_{-0.69}$	85±10	0	RC
SPT-CL J0001−5917	0.3674	−59.2986	4.09	0.25	0.57±0.03	$2.27^{+0.36}_{-0.49}$	17±5	0	-
SPT-CL J0001−5552	0.3867	−55.8667	4.10	0.50	0.28±0.01	$2.51^{+0.41}_{-0.55}$	28±6	0	-
SPT-CL J0001−6258	0.4021	−62.9795	4.86	0.50	0.22±0.01	$2.83^{+0.49}_{-0.59}$	26±6	0	-
SPT-CL J0001−5440	0.4146	−54.6679	8.34	0.25	0.92±0.03	$3.33^{+0.42}_{-0.51}$	47±8	0	-
SPT-CL J0001−5614	0.4807	−56.2437	4.96	0.75	0.41±0.01	$2.71^{+0.47}_{-0.56}$	41±6	0	-
SPT-CL J0002−5557	0.5119	−55.9623	7.86	0.50	1.60±0.08	$2.56^{+0.33}_{-0.39}$	18±3	1	LL
SPT-CL J0002−5017	0.6415	−50.2894	5.18	0.25	0.97±0.03	$2.30^{+0.39}_{-0.46}$	35±7	0	-
SPT-CL J0003−5938	0.8124	−59.6381	4.06	1.00	-	-	-	0	-
SPT-CL J0004−5814	1.0230	−58.2430	4.06	1.00	-	-	-	0	-
SPT-CL J0005−5415	1.2639	−54.2519	7.99	0.25	0.52±0.01	$3.70^{+0.48}_{-0.59}$	56±8	0	-
SPT-CL J0005−5849	1.2785	−58.8215	4.25	0.25	0.64±0.03	$2.27^{+0.37}_{-0.50}$	24±5	0	-
SPT-CL J0005−5426	1.4344	−54.4359	4.28	0.75	0.85±0.03	$2.12^{+0.36}_{-0.47}$	39±7	0	-
SPT-CL J0005−5758	1.4655	−57.9698	5.17	0.25	0.37±0.01	$2.82^{+0.51}_{-0.57}$	44±7	0	-
SPT-CL J0006−5143	1.5704	−51.7297	4.52	1.25	0.40±0.01	$2.55^{+0.43}_{-0.55}$	49±7	0	LOS
SPT-CL J0007−5710	1.7826	−57.1680	4.48	0.25	0.58±0.02	$2.38^{+0.40}_{-0.51}$	50±7	0	LOS
SPT-CL J0007−5719	1.9268	−57.3277	5.95	0.50	0.60±0.02	$2.90^{+0.50}_{-0.51}$	47±7	0	-
SPT-CL J0007−5605	1.9781	−56.0897	4.60	0.50	0.95±0.03	$2.13^{+0.36}_{-0.46}$	33±6	0	-
SPT-CL J0008−6247	2.0091	−62.7914	4.25	0.25	0.97±0.03	$2.02^{+0.32}_{-0.44}$	31±6	0	RC
SPT-CL J0008−5334	2.2486	−53.5782	4.52	0.50	-	-	-	0	-
SPT-CL J0009−4949	2.4618	−49.8267	4.08	1.00	-	-	-	0	-
SPT-CL J0010−6422	2.5448	−64.3674	4.16	0.50	-	-	-	0	-
SPT-CL J0010−6042	2.6230	−60.7137	5.43	0.50	0.80±0.02	$2.53^{+0.43}_{-0.50}$	38±7	0	-
SPT-CL J0010−5450	2.6790	−54.8345	4.29	0.25	0.52±0.02	$2.37^{+0.38}_{-0.52}$	23±5	0	-
SPT-CL J0010−5202	2.7092	−52.0437	4.27	0.25	0.96±0.04	$2.03^{+0.34}_{-0.45}$	21±6	0	-
SPT-CL J0010−5112	2.7398	−51.2038	6.83	1.50	0.210±0.007	$3.67^{+0.51}_{-0.63}$	56±8	0	-
SPT-CL J0011−5541	2.9803	−55.6944	4.24	0.25	0.94±0.05	$2.03^{+0.32}_{-0.45}$	15±5	0	-
SPT-CL J0012−5352	3.0747	−53.8692	4.96	1.25	0.34±0.01	$2.76^{+0.49}_{-0.57}$	46±7	0	-
SPT-CL J0012−4959	3.2111	−49.9852	5.22	0.50	-	-	-	0	-
SPT-CL J0012−5959	3.2475	−59.9861	5.08	0.25	0.72±0.03	$2.48^{+0.43}_{-0.50}$	24±6	0	-
SPT-CL J0013−5714	3.2946	−57.2429	4.73	1.50	0.61±0.02	$2.45^{+0.42}_{-0.52}$	45±7	0	-
SPT-CL J0013−5310	3.4148	−53.1815	5.56	0.50	0.89±0.03	$2.48^{+0.42}_{-0.49}$	45±8	0	LOS
SPT-CL J0013−5926	3.4787	−59.4499	4.62	0.25	0.98±0.06	$2.11^{+0.37}_{-0.46}$	29±6	0	-
SPT-CL J0014−5142	3.5477	−51.7065	4.03	0.75	-	-	-	0	-
SPT-CL J0014−4952	3.7042	−49.8776	14.48	0.25	0.752	$5.02^{+0.54}_{-0.68}$	98±11	0	-
SPT-CL J0014−6446	3.7288	−64.7675	4.21	0.25	0.78±0.04	$2.15^{+0.35}_{-0.47}$	17±5	0	-
SPT-CL J0015−5004	3.7826	−50.0757	9.45	0.25	0.96±0.02	$3.54^{+0.43}_{-0.52}$	61±9	0	-
SPT-CL J0015−5604	3.8840	−56.0809	4.21	0.25	1.31±0.07	$1.79^{+0.27}_{-0.39}$	24±6	0	-
SPT-CL J0015−5146	3.8981	−51.7727	7.62	0.50	0.414±0.009	$3.72^{+0.50}_{-0.60}$	84±9	0	-
SPT-CL J0016−5650	4.2114	−56.8405	4.02	0.75	0.47±0.02	$2.35^{+0.37}_{-0.51}$	31±6	0	-
SPT-CL J0018−5504	4.5592	−55.0697	5.20	0.75	0.42±0.01	$2.81^{+0.48}_{-0.56}$	53±8	0	RC
SPT-CL J0018−6148	4.5878	−61.8119	4.02	0.25	-	-	-	0	-
SPT-CL J0018−5700	4.6800	−57.0118	4.11	0.25	-	-	-	0	-
SPT-CL J0019−5527	4.8269	−55.4525	12.94	0.25	0.93±0.03	$4.38^{+0.52}_{-0.61}$	53±8	0	-
SPT-CL J0019−5128	4.8894	−51.4723	5.12	0.50	0.62±0.02	$2.58^{+0.45}_{-0.52}$	40±7	0	-
SPT-CL J0020−5612	5.2074	−56.2100	5.68	0.25	1.17±0.07	$2.29^{+0.40}_{-0.44}$	29±4	1	-
SPT-CL J0021−5900	5.3445	−59.0070	5.56	0.75	0.36±0.01	$2.99^{+0.51}_{-0.57}$	46±7	0	-
SPT-CL J0022−5043	5.5924	−50.7194	4.70	2.00	-	-	-	0	-
SPT-CL J0023−6037	5.7988	−60.6255	4.38	0.25	-	-	-	0	-
SPT-CL J0023−5450	5.9387	−54.8430	5.10	0.75	0.41±0.01	$2.76^{+0.49}_{-0.56}$	44±7	0	-
SPT-CL J0023−5905	5.9869	−59.0897	5.74	0.25	0.58±0.02	$2.87^{+0.47}_{-0.53}$	48±8	0	-
SPT-CL J0024−6001	6.0309	−60.0210	4.27	0.25	1.03±0.04	$1.97^{+0.33}_{-0.44}$	22±6	0	-
SPT-CL J0024−6338	6.0549	−63.6336	4.43	0.25	1.28±0.07	$1.86^{+0.30}_{-0.40}$	20±5	0	-
SPT-CL J0024−5752	6.0798	−57.8703	4.03	0.25	0.85±0.04	$2.05^{+0.32}_{-0.44}$	21±6	0	-
SPT-CL J0024−5151	6.1538	−51.8648	5.61	0.50	0.75±0.02	$2.63^{+0.44}_{-0.50}$	60±9	0	LOS
SPT-CL J0024−6301	6.1704	−63.0222	4.88	0.25	0.67±0.02	$2.44^{+0.44}_{-0.51}$	45±7	0	-

Table 1 — *Continued*

SPT ID	R.A. (J2000)	Decl. (J2000)	Best ξ	θ_c	Redshift	M_{500c} $(10^{14} h_{70}^{-1} M_\odot)$	λ	*Spitzer*	Notes
SPT-CL J0024−5147	6.2343	−51.7968	4.37	0.25	0.86±0.04	$2.12^{+0.35}_{-0.47}$	15±5	0	-
SPT-CL J0025−5619	6.3622	−56.3232	6.79	0.50	0.81±0.02	$2.99^{+0.45}_{-0.50}$	38±7	0	LOS
SPT-CL J0025−5034	6.3676	−50.5791	9.26	0.50	0.36±0.01	$4.30^{+0.53}_{-0.64}$	55±7	0	-
SPT-CL J0025−5120	6.4535	−51.3395	4.44	0.25	0.35±0.01	$2.56^{+0.44}_{-0.56}$	41±6	0	-
SPT-CL J0026−5855	6.5763	−58.9184	6.07	1.00	0.59±0.02	$2.98^{+0.47}_{-0.52}$	44±8	0	-
SPT-CL J0026−5640	6.6204	−56.6818	4.81	0.25	0.47±0.02	$2.59^{+0.46}_{-0.55}$	30±6	0	-
SPT-CL J0026−5700	6.7270	−57.0123	4.88	0.25	0.78±0.02	$2.35^{+0.40}_{-0.50}$	45±7	0	LOS
SPT-CL J0027−5456	6.8825	−54.9483	5.00	0.25	0.83±0.03	$2.35^{+0.40}_{-0.49}$	29±6	0	-
SPT-CL J0027−6326	6.9483	−63.4353	9.67	0.25	0.86±0.03	$3.75^{+0.45}_{-0.55}$	24±7	0	-
SPT-CL J0027−5313	6.9607	−53.2293	6.29	0.75	0.53±0.02	$3.11^{+0.48}_{-0.54}$	47±7	0	RC
SPT-CL J0028−6426	7.1692	−64.4468	5.35	0.25	0.61±0.02	$2.67^{+0.46}_{-0.52}$	45±7	0	-
SPT-CL J0030−5213	7.5117	−52.2299	6.74	0.25	0.52±0.02	$3.27^{+0.49}_{-0.55}$	45±8	0	LOS
SPT-CL J0030−5615	7.5495	−56.2654	4.56	0.25	0.52±0.03	$2.45^{+0.42}_{-0.53}$	10±4	0	-
SPT-CL J0030−6134	7.7407	−61.5720	5.79	0.25	0.85±0.02	$2.60^{+0.45}_{-0.47}$	45±7	0	-
SPT-CL J0031−5508	7.8273	−55.1439	4.90	0.25	0.81±0.02	$2.33^{+0.40}_{-0.48}$	37±7	0	LOS
SPT-CL J0031−6433	7.9829	−64.5542	4.70	0.25	1.10±0.06	$2.03^{+0.36}_{-0.45}$	31±4	1	-
SPT-CL J0031−5712	7.9970	−57.2113	4.05	0.25	0.90±0.02	$2.02^{+0.31}_{-0.44}$	50±7	0	-
SPT-CL J0032−5746	8.1115	−57.7734	6.99	0.50	0.67±0.01	$3.21^{+0.47}_{-0.54}$	74±10	0	-
SPT-CL J0032−5211	8.1165	−52.1948	4.12	0.25	0.51±0.03	$2.34^{+0.36}_{-0.51}$	14±4	0	-
SPT-CL J0032−5540	8.2167	−55.6693	5.09	1.00	0.202±0.008	$2.94^{+0.50}_{-0.62}$	39±6	0	-
SPT-CL J0033−6117	8.2608	−61.2901	4.03	0.25	0.82±0.03	$2.08^{+0.32}_{-0.45}$	23±5	0	-
SPT-CL J0033−5027	8.2927	−50.4538	4.07	0.25	-	-	-	0	-
SPT-CL J0033−6326	8.4711	−63.4456	13.46	0.50	0.597	$5.03^{+0.58}_{-0.70}$	68±8	0	-
SPT-CL J0034−5906	8.6528	−59.1130	4.92	0.50	0.59±0.02	$2.52^{+0.45}_{-0.54}$	36±7	0	LOS
SPT-CL J0035−5455	8.8176	−54.9295	6.58	0.75	0.30±0.01	$3.47^{+0.49}_{-0.61}$	42±7	0	-
SPT-CL J0035−6030	8.8704	−60.5161	5.11	0.50	0.92±0.03	$2.32^{+0.41}_{-0.47}$	37±7	0	-
SPT-CL J0036−6241	9.1737	−62.6913	5.53	0.25	0.202±0.007	$3.14^{+0.51}_{-0.60}$	63±8	0	LOS
SPT-CL J0036−6000	9.2339	−60.0136	5.78	0.25	0.89±0.03	$2.57^{+0.43}_{-0.48}$	46±7	0	-
SPT-CL J0037−6327	9.2882	−63.4666	5.14	0.25	0.85±0.03	$2.39^{+0.42}_{-0.48}$	37±7	0	-
SPT-CL J0037−5047	9.4429	−50.7934	8.26	0.75	1.026	$3.18^{+0.40}_{-0.50}$	44±0	0	-
SPT-CL J0038−6215	9.5065	−62.2590	6.41	1.25	0.231±0.007	$3.47^{+0.53}_{-0.60}$	68±8	0	-
SPT-CL J0038−6436	9.5726	−64.6005	6.18	0.25	0.61±0.02	$2.98^{+0.47}_{-0.53}$	60±8	0	-
SPT-CL J0038−5040	9.6165	−50.6735	4.34	0.75	1.22±0.06	$1.87^{+0.30}_{-0.42}$	16±5	0	-
SPT-CL J0038−5244	9.7196	−52.7439	7.87	0.50	0.43±0.01	$3.78^{+0.49}_{-0.59}$	67±8	0	-
SPT-CL J0039−5007	9.8005	−50.1267	4.01	0.25	-	-	-	0	-
SPT-CL J0040−6351	10.0648	−63.8555	4.09	0.75	1.01±0.05	$1.95^{+0.30}_{-0.44}$	19±6	0	-
SPT-CL J0040−6347	10.1694	−63.7859	5.27	0.50	-	-	-	0	-
SPT-CL J0041−6030	10.2714	−60.5131	4.09	0.25	-	-	-	0	-
SPT-CL J0041−5343	10.2810	−53.7291	4.79	0.25	0.62±0.02	$2.47^{+0.42}_{-0.52}$	34±6	0	-
SPT-CL J0041−5107	10.3028	−51.1186	6.07	0.25	0.51±0.01	$3.06^{+0.47}_{-0.54}$	61±8	0	-
SPT-CL J0041−5119	10.4302	−51.3207	4.25	0.25	-	-	-	0	-
SPT-CL J0042−6244	10.5539	−62.7433	5.30	0.25	1.60±0.08	$1.87^{+0.33}_{-0.39}$	32±4	1	LL
SPT-CL J0043−5314	10.8292	−53.2362	4.22	0.25	0.70±0.02	$2.22^{+0.35}_{-0.48}$	70±9	0	-
SPT-CL J0043−6241	10.8382	−62.6836	4.10	0.50	0.55±0.02	$2.30^{+0.36}_{-0.50}$	47±8	0	-
SPT-CL J0043−6433	10.9242	−64.5563	4.02	0.25	0.44±0.02	$2.36^{+0.37}_{-0.52}$	21±5	0	-
SPT-CL J0044−6415	11.0309	−64.2565	6.76	0.25	1.13±0.06	$2.66^{+0.40}_{-0.45}$	29±4	1	-
SPT-CL J0044−5737	11.0507	−57.6234	4.05	0.50	0.70±0.02	$2.16^{+0.34}_{-0.48}$	54±8	0	-
SPT-CL J0044−5157	11.2408	−51.9643	4.91	0.25	0.93±0.06	$2.23^{+0.39}_{-0.47}$	34±6	0	-
SPT-CL J0045−6254	11.2543	−62.9128	4.00	0.25	-	-	-	0	-
SPT-CL J0045−6039	11.2607	−60.6517	4.96	0.25	0.61±0.02	$2.52^{+0.45}_{-0.53}$	29±6	0	-
SPT-CL J0045−6236	11.4931	−62.6089	5.57	0.25	0.54±0.02	$2.82^{+0.47}_{-0.53}$	40±7	0	-
SPT-CL J0046−5239	11.5438	−52.6639	4.24	0.25	0.54±0.02	$2.35^{+0.39}_{-0.51}$	30±6	0	-
SPT-CL J0046−5537	11.6335	−55.6312	4.23	1.50	0.164±0.009	$2.65^{+0.44}_{-0.58}$	30±6	0	-
SPT-CL J0046−6456	11.6568	−64.9391	4.42	0.25	0.79±0.03	$2.21^{+0.36}_{-0.48}$	22±5	0	LOS
SPT-CL J0046−5413	11.6642	−54.2276	4.19	0.50	0.44±0.01	$2.41^{+0.39}_{-0.53}$	42±6	0	LOS
SPT-CL J0046−6502	11.6843	−65.0433	4.17	1.50	0.032±0.005	$2.71^{+0.45}_{-0.60}$	19±3	0	-
SPT-CL J0046−5825	11.7044	−58.4228	5.34	0.25	0.65±0.02	$2.63^{+0.46}_{-0.51}$	42±7	0	-
SPT-CL J0047−6428	11.7508	−64.4765	4.75	0.25	1.22±0.06	$1.97^{+0.34}_{-0.44}$	44±8	0	-
SPT-CL J0047−6057	11.9330	−60.9513	4.24	0.50	0.43±0.01	$2.43^{+0.39}_{-0.53}$	40±7	0	-

BLEEM ET AL.

Table 1 — *Continued*

SPT ID	R.A. (J2000)	Decl. (J2000)	ξ	θ_c	Redshift	M_{500c} $(10^{14} h_{70}^{-1} M_\odot)$	λ	*Spitzer*	Notes
SPT-CL J0048−5244	12.0884	−52.7478	15.45	0.25	1.03±0.02	$4.74^{+0.51}_{-0.63}$	72±10	0	LOS
SPT-CL J0048−6416	12.2362	−64.2709	14.32	0.25	0.92±0.02	$4.70^{+0.52}_{-0.63}$	61±9	0	-
SPT-CL J0049−5615	12.2950	−56.2536	6.09	0.25	0.40±0.01	$3.18^{+0.47}_{-0.55}$	56±7	0	LOS
SPT-CL J0049−5315	12.3777	−53.2527	12.84	0.25	0.72±0.01	$4.70^{+0.52}_{-0.65}$	87±10	0	-
SPT-CL J0049−5247	12.4467	−52.7946	6.65	0.25	0.60±0.02	$3.16^{+0.46}_{-0.54}$	43±7	0	LOS
SPT-CL J0049−6200	12.4603	−62.0003	4.65	0.25	0.57±0.02	$2.45^{+0.43}_{-0.52}$	45±7	0	-
SPT-CL J0049−5709	12.4690	−57.1522	5.17	0.50	0.87±0.02	$2.37^{+0.42}_{-0.49}$	61±9	0	LOS
SPT-CL J0050−5646	12.6118	−56.7808	4.17	0.25	-	-	-	0	-
SPT-CL J0050−5817	12.6648	−58.2841	4.00	0.25	0.88±0.03	$2.03^{+0.32}_{-0.44}$	38±7	0	LOS
SPT-CL J0050−5018	12.6693	−50.3017	4.49	0.50	0.160±0.009	$2.75^{+0.45}_{-0.59}$	27±5	0	-
SPT-CL J0050−5944	12.7493	−59.7402	4.03	0.25	-	-	-	0	-
SPT-CL J0051−5153	12.8530	−51.8936	6.49	0.50	0.42±0.01	$3.31^{+0.48}_{-0.57}$	60±8	0	-
SPT-CL J0051−6318	12.8557	−63.3085	4.13	0.25	-	-	-	0	-
SPT-CL J0051−5033	12.9869	−50.5516	4.18	0.25	0.90±0.03	$2.05^{+0.33}_{-0.46}$	42±7	0	-
SPT-CL J0052−5657	13.1433	−56.9604	6.84	0.50	0.314±0.010	$3.56^{+0.51}_{-0.60}$	52±8	0	LOS
SPT-CL J0052−5746	13.1456	−57.7698	7.05	0.50	0.256±0.009	$3.71^{+0.50}_{-0.62}$	50±7	0	-
SPT-CL J0052−5942	13.2060	−59.7116	9.88	0.25	1.13±0.06	$3.44^{+0.42}_{-0.51}$	51±5	1	-
SPT-CL J0053−5944	13.3739	−59.7374	4.13	0.25	-	-	-	0	-
SPT-CL J0054−6023	13.6430	−60.3881	5.06	0.25	1.47±0.07	$1.89^{+0.33}_{-0.40}$	37±4	1	-
SPT-CL J0054−6104	13.6782	−61.0817	4.19	0.75	-	-	-	0	-
SPT-CL J0054−5821	13.6947	−58.3654	4.04	0.25	-	-	-	0	-
SPT-CL J0054−5731	13.7290	−57.5277	6.01	0.50	0.77±0.02	$2.77^{+0.44}_{-0.50}$	55±8	0	-
SPT-CL J0054−5710	13.7362	−57.1737	4.09	2.75	-	-	-	0	-
SPT-CL J0055−6310	13.9758	−63.1752	4.30	0.25	0.54±0.02	$2.37^{+0.39}_{-0.52}$	46±7	0	-
SPT-CL J0057−5054	14.3376	−50.9053	4.47	1.25	0.54±0.02	$2.43^{+0.39}_{-0.52}$	43±7	0	-
SPT-CL J0058−6146	14.5858	−61.7667	16.29	0.25	0.87±0.02	$5.17^{+0.56}_{-0.68}$	93±10	0	-
SPT-CL J0059−5105	14.7743	−51.0960	7.80	0.75	0.60±0.02	$3.54^{+0.47}_{-0.56}$	58±8	0	LOS
SPT-CL J0059−5539	14.7967	−55.6599	4.39	0.25	0.79±0.05	$2.18^{+0.37}_{-0.47}$	11±4	0	-
SPT-CL J0059−5436	14.8002	−54.6089	4.74	0.50	0.41±0.01	$2.62^{+0.46}_{-0.56}$	36±6	0	-
SPT-CL J0059−4955	14.9454	−49.9198	5.00	0.25	0.97±0.05	$2.23^{+0.39}_{-0.47}$	14±5	0	-
SPT-CL J0059−5217	14.9651	−52.2940	4.13	0.25	-	-	-	0	-
SPT-CL J0100−5359	15.0208	−53.9865	6.39	0.25	1.04±0.05	$2.64^{+0.40}_{-0.45}$	20±6	0	-
SPT-CL J0100−5021	15.0554	−50.3508	4.07	0.25	-	-	-	0	-
SPT-CL J0100−4958	15.0573	−49.9736	7.65	0.25	1.33±0.07	$2.73^{+0.36}_{-0.43}$	37±4	1	-
SPT-CL J0100−5910	15.2263	−59.1668	5.58	0.25	0.92±0.03	$2.46^{+0.43}_{-0.48}$	36±7	0	LOS
SPT-CL J0101−5332	15.2549	−53.5473	5.29	0.75	1.10±0.06	$2.22^{+0.37}_{-0.45}$	32±4	1	LOS
SPT-CL J0101−6047	15.2808	−60.7845	6.12	0.50	0.207±0.007	$3.39^{+0.51}_{-0.61}$	55±8	0	-
SPT-CL J0101−6007	15.3214	−60.1231	4.52	1.25	-	-	-	0	-
SPT-CL J0101−5219	15.4187	−52.3228	4.13	0.50	0.45±0.02	$2.38^{+0.38}_{-0.52}$	18±4	0	-
SPT-CL J0102−5028	15.7048	−50.4805	4.43	0.50	0.76±0.02	$2.23^{+0.37}_{-0.48}$	46±8	0	-
SPT-CL J0103−5242	15.8405	−52.7120	4.95	0.50	0.61±0.02	$2.52^{+0.44}_{-0.52}$	26±6	0	-
SPT-CL J0103−5516	15.9610	−55.2769	4.04	0.25	-	-	-	0	-
SPT-CL J0104−5706	16.1265	−57.1155	4.56	0.25	0.53±0.02	$2.47^{+0.42}_{-0.53}$	37±7	0	-
SPT-CL J0104−6219	16.1963	−62.3214	5.75	0.25	0.61±0.02	$2.81^{+0.47}_{-0.52}$	36±6	0	-
SPT-CL J0104−6226	16.2477	−62.4357	4.51	0.50	0.93±0.03	$2.11^{+0.35}_{-0.46}$	42±7	0	-
SPT-CL J0105−6257	16.3001	−62.9645	4.52	0.25	1.06±0.03	$2.02^{+0.33}_{-0.45}$	52±9	0	-
SPT-CL J0105−6302	16.4095	−63.0373	5.33	0.25	0.92±0.03	$2.39^{+0.41}_{-0.48}$	37±7	0	-
SPT-CL J0106−5355	16.5707	−53.9277	11.63	0.25	0.48±0.01	$4.80^{+0.55}_{-0.68}$	64±8	0	-
SPT-CL J0106−5229	16.6116	−52.4875	4.67	0.25	1.52±0.08	$1.76^{+0.29}_{-0.39}$	15±3	1	-
SPT-CL J0106−5943	16.6119	−59.7195	16.02	0.50	0.348	$6.09^{+0.65}_{-0.81}$	93±10	0	-
SPT-CL J0106−5800	16.6646	−58.0071	7.09	1.25	0.280±0.008	$3.69^{+0.50}_{-0.61}$	64±8	0	RC
SPT-CL J0106−6233	16.7239	−62.5628	4.08	0.25	0.92±0.04	$2.01^{+0.31}_{-0.45}$	19±6	0	-
SPT-CL J0107−6324	16.8100	−63.4145	4.58	0.50	0.97±0.04	$2.11^{+0.34}_{-0.46}$	26±6	0	-
SPT-CL J0107−5242	16.8464	−52.7014	4.19	0.50	1.14±0.06	$1.90^{+0.29}_{-0.42}$	29±6	0	-
SPT-CL J0107−6332	16.8527	−63.5376	5.49	0.25	0.246±0.010	$3.07^{+0.55}_{-0.57}$	36±6	0	LOS
SPT-CL J0107−5833	16.9150	−58.5511	11.11	0.25	1.13±0.06	$3.73^{+0.42}_{-0.53}$	45±8	0	-
SPT-CL J0109−6028	17.3170	−60.4832	4.18	0.25	-	-	-	0	-
SPT-CL J0109−5132	17.3319	−51.5410	4.60	0.25	0.33±0.01	$2.65^{+0.44}_{-0.56}$	34±6	0	-
SPT-CL J0109−5839	17.3347	−58.6522	4.32	0.50	0.72±0.02	$2.23^{+0.36}_{-0.48}$	40±7	0	-
SPT-CL J0109−5629	17.4039	−56.4875	5.12	0.25	0.49±0.01	$2.70^{+0.47}_{-0.55}$	52±8	0	-
SPT-CL J0110−5121	17.5213	−51.3590	6.32	0.75	0.79±0.02	$2.84^{+0.45}_{-0.50}$	64±8	0	-

Table 1 — *Continued*

SPT ID	R.A. (J2000)	Decl. (J2000)	Best ξ	θ_c	Redshift	M_{500c} $(10^{14} h_{70}^{-1} M_\odot)$	λ	*Spitzer*	Notes
SPT-CL J0110−5857	17.5342	−58.9656	4.81	0.25	0.34±0.02	$2.73^{+0.46}_{-0.57}$	18±5	0	LOS
SPT-CL J0110−6045	17.5847	−60.7615	5.79	1.00	0.72±0.03	$2.73^{+0.47}_{-0.48}$	29±7	0	-
SPT-CL J0110−5333	17.5874	−53.5659	4.44	0.75	0.93±0.03	$2.09^{+0.35}_{-0.46}$	29±6	0	-
SPT-CL J0110−5622	17.6798	−56.3795	5.71	0.25	1.52±0.03	$2.04^{+0.38}_{-0.39}$	40±6	0	LOS
SPT-CL J0111−6336	17.7603	−63.6044	4.03	0.25	-	-	-	0	-
SPT-CL J0111−5941	17.7612	−59.6971	4.86	0.25	0.97±0.06	$2.18^{+0.38}_{-0.47}$	18±3	1	LOS
SPT-CL J0111−5425	17.7712	−54.4186	12.11	0.25	0.48±0.01	$4.93^{+0.56}_{-0.68}$	73±10	0	-
SPT-CL J0111−5818	17.8279	−58.3026	7.81	0.25	0.70±0.03	$3.42^{+0.45}_{-0.54}$	24±6	0	-
SPT-CL J0111−5519	17.8592	−55.3181	7.64	1.00	0.50±0.01	$3.62^{+0.50}_{-0.58}$	51±8	0	LOS
SPT-CL J0111−5428	17.9422	−54.4753	4.54	0.75	-	-	-	0	-
SPT-CL J0112−5942	18.0257	−59.7081	5.39	0.25	1.20±0.07	$2.18^{+0.39}_{-0.43}$	34±4	1	-
SPT-CL J0112−6439	18.1680	−64.6598	4.45	0.50	-	-	-	0	-
SPT-CL J0113−5011	18.2646	−50.1954	4.11	0.25	-	-	-	0	-
SPT-CL J0113−5550	18.3560	−55.8433	4.80	0.75	0.360±0.010	$2.69^{+0.48}_{-0.56}$	61±8	0	RC,LOS
SPT-CL J0113−6105	18.3854	−61.0885	6.69	0.75	0.44±0.01	$3.36^{+0.47}_{-0.57}$	67±8	0	-
SPT-CL J0113−5502	18.4476	−55.0395	4.08	0.25	0.25±0.01	$2.54^{+0.39}_{-0.56}$	31±6	0	-
SPT-CL J0114−5244	18.5018	−52.7395	5.95	0.75	0.43±0.01	$3.09^{+0.48}_{-0.56}$	64±8	0	-
SPT-CL J0114−6144	18.5294	−61.7363	5.06	3.00	1.57±0.08	$1.82^{+0.32}_{-0.39}$	28±4	1	-
SPT-CL J0115−5730	18.7995	−57.5107	4.40	0.25	0.20±0.01	$2.67^{+0.45}_{-0.58}$	16±4	0	-
SPT-CL J0115−6516	18.8105	−65.2826	5.01	0.25	0.68±0.04	$2.49^{+0.45}_{-0.51}$	14±5	0	-
SPT-CL J0115−5517	18.9960	−55.2845	4.08	0.75	0.49±0.02	$2.34^{+0.37}_{-0.52}$	26±6	0	-
SPT-CL J0116−5039	19.0948	−50.6624	5.86	0.25	1.60±0.08	$2.03^{+0.36}_{-0.37}$	22±4	1	LL
SPT-CL J0116−5045	19.1481	−50.7652	5.47	0.75	0.40±0.01	$2.92^{+0.48}_{-0.56}$	56±8	0	-
SPT-CL J0117−5053	19.2821	−50.8946	7.15	1.75	0.205±0.007	$3.80^{+0.53}_{-0.62}$	63±8	0	RC
SPT-CL J0117−5050	19.2897	−50.8481	4.36	0.25	0.206±0.009	$2.66^{+0.43}_{-0.56}$	35±6	0	-
SPT-CL J0117−6032	19.3721	−60.5406	11.26	0.50	1.04±0.03	$3.89^{+0.46}_{-0.55}$	55±9	0	-
SPT-CL J0118−5637	19.5198	−56.6332	6.75	1.00	0.205±0.007	$3.64^{+0.51}_{-0.61}$	59±8	0	-
SPT-CL J0118−5156	19.5989	−51.9418	11.51	0.50	0.705	$4.42^{+0.51}_{-0.61}$	76±9	0	-
SPT-CL J0118−5402	19.6647	−54.0450	5.27	1.00	0.236±0.008	$2.99^{+0.49}_{-0.60}$	51±7	0	-
SPT-CL J0118−5826	19.7030	−58.4391	4.16	0.25	0.27±0.01	$2.54^{+0.41}_{-0.55}$	38±6	0	LOS
SPT-CL J0118−6520	19.7399	−65.3345	9.54	0.50	0.083±0.008	$4.79^{+0.56}_{-0.71}$	19±6	0	-
SPT-CL J0118−5644	19.7483	−56.7487	4.65	0.25	1.47±0.07	$1.79^{+0.30}_{-0.39}$	10±3	1	-
SPT-CL J0119−5750	19.8480	−57.8488	4.92	0.25	0.95±0.03	$2.23^{+0.38}_{-0.48}$	40±7	0	-
SPT-CL J0119−5919	19.9157	−59.3281	6.95	0.50	0.59±0.02	$3.29^{+0.44}_{-0.55}$	43±7	0	-
SPT-CL J0119−5838	19.9825	−58.6462	5.19	0.25	0.56±0.02	$2.65^{+0.47}_{-0.53}$	20±5	0	-
SPT-CL J0120−5435	20.0146	−54.5869	4.04	1.00	-	-	-	0	-
SPT-CL J0120−6522	20.0564	−65.3780	4.12	0.25	0.54±0.03	$2.31^{+0.37}_{-0.51}$	15±4	0	-
SPT-CL J0121−5432	20.2773	−54.5366	4.28	0.25	-	-	-	0	-
SPT-CL J0121−5547	20.3367	−55.7882	4.62	0.25	1.09±0.04	$2.02^{+0.34}_{-0.44}$	31±7	0	LOS
SPT-CL J0121−5121	20.3561	−51.3578	4.14	0.50	0.24±0.01	$2.56^{+0.41}_{-0.56}$	23±5	0	-
SPT-CL J0121−5458	20.3704	−54.9673	5.73	0.50	0.83±0.02	$2.60^{+0.43}_{-0.48}$	58±8	0	LOS
SPT-CL J0121−5804	20.4650	−58.0800	4.05	0.25	-	-	-	0	-
SPT-CL J0122−5801	20.5492	−58.0218	8.98	0.25	1.60±0.08	$2.79^{+0.36}_{-0.41}$	25±3	1	LOS,LL
SPT-CL J0122−5241	20.5959	−52.6896	4.23	0.25	1.29±0.07	$1.79^{+0.29}_{-0.40}$	19±5	0	-
SPT-CL J0122−5554	20.6445	−55.9067	4.36	0.50	0.69±0.03	$2.26^{+0.37}_{-0.49}$	25±6	0	LOS
SPT-CL J0123−5112	20.8847	−51.2131	4.17	1.75	-	-	-	0	-
SPT-CL J0123−6159	20.8886	−61.9975	8.53	0.25	0.87±0.02	$3.44^{+0.43}_{-0.52}$	57±8	0	-
SPT-CL J0124−5937	21.1861	−59.6276	8.13	0.75	0.204±0.006	$4.15^{+0.53}_{-0.64}$	76±9	0	-
SPT-CL J0125−5637	21.2960	−56.6279	5.30	0.75	1.47±0.07	$1.97^{+0.34}_{-0.40}$	9±3	1	-
SPT-CL J0126−6143	21.7079	−61.7230	4.34	0.50	0.78±0.03	$2.19^{+0.35}_{-0.48}$	21±6	0	-
SPT-CL J0128−6506	22.0118	−65.1107	6.27	0.25	1.28±0.07	$2.41^{+0.36}_{-0.42}$	25±4	1	-
SPT-CL J0128−5714	22.0502	−57.2363	4.08	1.00	0.42±0.02	$2.39^{+0.39}_{-0.52}$	17±5	0	-
SPT-CL J0128−5222	22.0507	−52.3827	6.12	0.25	1.37±0.07	$2.27^{+0.36}_{-0.41}$	28±4	1	-
SPT-CL J0128−5058	22.2053	−50.9773	4.80	2.00	-	-	-	0	-
SPT-CL J0129−5329	22.3076	−53.4900	4.18	0.50	-	-	-	0	-
SPT-CL J0129−6442	22.3702	−64.7091	4.15	0.25	-	-	-	0	-
SPT-CL J0129−6432	22.4317	−64.5462	21.42	0.50	0.326	$7.26^{+0.78}_{-0.94}$	118±11	0	-
SPT-CL J0130−6357	22.6164	−63.9585	4.14	0.25	0.51±0.02	$2.34^{+0.39}_{-0.51}$	47±7	0	LOS
SPT-CL J0130−6314	22.6190	−63.2355	6.01	0.25	0.77±0.02	$2.75^{+0.45}_{-0.50}$	45±8	0	-
SPT-CL J0131−5849	22.8516	−58.8206	4.76	0.50	0.48±0.01	$2.57^{+0.46}_{-0.54}$	67±8	0	-
SPT-CL J0131−6248	22.8519	−62.8015	4.98	0.25	0.69±0.03	$2.47^{+0.41}_{-0.50}$	23±6	0	LOS

Bleem et al.

Table 1 — *Continued*

SPT ID	R.A. (J2000)	Decl. (J2000)	Best ξ	θ_c	Redshift	M_{500c} $(10^{14}h_{70}^{-1}M_\odot)$	λ	*Spitzer*	Notes
SPT-CL J0131−5921	22.8565	−59.3589	10.72	0.25	0.99±0.06	$3.81^{+0.44}_{-0.55}$	51±7	0	-
SPT-CL J0131−5604	22.9319	−56.0802	11.68	0.25	0.80±0.02	$4.30^{+0.51}_{-0.60}$	86±10	0	-
SPT-CL J0132−5535	23.0601	−55.5896	6.07	0.25	0.67±0.02	$2.88^{+0.46}_{-0.52}$	61±8	0	-
SPT-CL J0132−5712	23.1202	−57.2154	5.24	0.25	1.21±0.05	$2.11^{+0.38}_{-0.44}$	18±6	0	-
SPT-CL J0132−5312	23.2140	−53.2039	4.33	0.25	-	-	-	0	-
SPT-CL J0133−5945	23.2542	−59.7631	4.09	0.75	-	-	-	0	-
SPT-CL J0133−5821	23.2738	−58.3511	4.93	1.00	0.199±0.008	$2.89^{+0.50}_{-0.59}$	40±7	0	-
SPT-CL J0133−6417	23.4020	−64.2980	4.21	0.50	-	-	-	0	-
SPT-CL J0133−6434	23.4076	−64.5699	13.68	1.00	0.319±0.007	$5.57^{+0.62}_{-0.77}$	113±11	0	-
SPT-CL J0134−5318	23.7405	−53.3138	4.95	0.25	0.96±0.03	$2.22^{+0.39}_{-0.47}$	31±6	0	-
SPT-CL J0135−5902	23.7892	−59.0340	7.40	0.25	0.51±0.01	$3.52^{+0.48}_{-0.57}$	57±8	0	-
SPT-CL J0135−6139	23.8714	−61.6504	4.02	0.25	-	-	-	0	-
SPT-CL J0135−5904	23.9792	−59.0810	8.66	0.75	0.50±0.01	$3.94^{+0.48}_{-0.59}$	99±11	0	LOS
SPT-CL J0136−6226	24.0412	−62.4467	6.02	0.50	0.89±0.03	$2.65^{+0.42}_{-0.47}$	26±6	0	LOS
SPT-CL J0137−6105	24.3434	−61.0908	6.03	0.25	0.42±0.01	$3.13^{+0.48}_{-0.57}$	45±7	0	-
SPT-CL J0137−6044	24.4366	−60.7464	4.25	0.25	-	-	-	0	-
SPT-CL J0138−6340	24.6007	−63.6745	4.26	0.25	1.29±0.07	$1.80^{+0.29}_{-0.40}$	25±5	0	-
SPT-CL J0139−6135	24.7755	−61.5980	4.56	0.50	-	-	-	0	-
SPT-CL J0139−5749	24.8289	−57.8267	5.04	0.25	0.76±0.02	$2.44^{+0.41}_{-0.50}$	49±8	0	-
SPT-CL J0139−5204	24.8873	−52.0786	9.37	0.25	0.93±0.02	$3.56^{+0.44}_{-0.53}$	61±8	0	-
SPT-CL J0139−5804	24.8881	−58.0673	4.80	0.25	0.77±0.03	$2.33^{+0.42}_{-0.49}$	33±6	0	-
SPT-CL J0140−4957	25.0294	−49.9538	4.20	0.50	-	-	-	0	-
SPT-CL J0140−5603	25.1185	−56.0547	4.20	0.50	-	-	-	0	-
SPT-CL J0140−5718	25.1340	−57.3155	4.04	0.25	-	-	-	0	-
SPT-CL J0140−6234	25.2163	−62.5690	4.04	0.25	1.06±0.05	$1.91^{+0.30}_{-0.42}$	20±6	0	-
SPT-CL J0140−5453	25.2227	−54.8877	4.02	0.75	-	-	-	0	-
SPT-CL J0140−6129	25.2469	−61.4852	4.16	0.25	-	-	-	0	-
SPT-CL J0142−5032	25.5442	−50.5386	15.94	0.25	0.679	$5.43^{+0.61}_{-0.72}$	105±10	0	-
SPT-CL J0142−5441	25.5801	−54.6979	4.13	0.25	-	-	-	0	-
SPT-CL J0143−5828	25.7887	−58.4755	5.40	0.50	0.200±0.007	$3.09^{+0.53}_{-0.60}$	56±8	0	-
SPT-CL J0144−5035	26.0838	−50.5912	4.01	1.50	1.07±0.06	$1.90^{+0.29}_{-0.41}$	17±5	0	-
SPT-CL J0144−5018	26.1727	−50.3070	4.22	1.75	-	-	-	0	-
SPT-CL J0144−5815	26.1784	−58.2593	4.53	1.25	0.84±0.05	$2.18^{+0.37}_{-0.48}$	10±4	0	-
SPT-CL J0145−5301	26.2552	−53.0259	12.21	1.50	0.117	$5.53^{+0.65}_{-0.77}$	52±7	0	-
SPT-CL J0145−5627	26.2753	−56.4506	4.74	0.25	0.210±0.010	$2.79^{+0.50}_{-0.60}$	30±6	0	-
SPT-CL J0145−6033	26.3021	−60.5587	21.08	0.50	0.179	$7.52^{+0.80}_{-0.97}$	89±10	0	-
SPT-CL J0145−5643	26.3099	−56.7209	4.57	0.25	0.89±0.06	$2.16^{+0.36}_{-0.47}$	9±5	0	-
SPT-CL J0145−6044	26.3217	−60.7346	4.21	1.00	-	-	-	0	-
SPT-CL J0145−5641	26.3532	−56.6947	4.06	0.25	-	-	-	0	-
SPT-CL J0145−5926	26.4847	−59.4435	4.44	0.25	0.52±0.02	$2.43^{+0.41}_{-0.52}$	25±5	0	-
SPT-CL J0146−5956	26.5663	−59.9490	4.59	0.25	1.60±0.08	$1.69^{+0.28}_{-0.37}$	-	0	LL
SPT-CL J0146−5002	26.5737	−50.0418	4.09	0.75	-	-	-	0	-
SPT-CL J0146−5320	26.6424	−53.3412	4.21	0.25	0.80±0.02	$2.14^{+0.34}_{-0.47}$	50±8	0	-
SPT-CL J0146−6126	26.6588	−61.4365	9.17	0.25	0.93±0.03	$3.51^{+0.44}_{-0.53}$	49±8	0	-
SPT-CL J0147−6330	26.9083	−63.5155	4.80	0.25	0.93±0.03	$2.20^{+0.38}_{-0.47}$	28±6	0	LOS
SPT-CL J0147−5017	26.9284	−50.2965	4.33	0.75	-	-	-	0	-
SPT-CL J0147−5150	26.9521	−51.8358	8.58	0.25	0.79±0.03	$3.53^{+0.44}_{-0.54}$	32±6	0	-
SPT-CL J0147−5622	26.9634	−56.3758	9.63	0.50	0.66±0.01	$4.00^{+0.48}_{-0.58}$	83±10	0	LOS
SPT-CL J0148−6525	27.0799	−65.4230	4.33	1.00	-	-	-	0	-
SPT-CL J0148−5034	27.2160	−50.5780	4.00	0.25	1.20±0.07	$1.80^{+0.27}_{-0.39}$	13±3	1	-
SPT-CL J0148−5500	27.2379	−55.0059	4.97	0.25	0.93±0.03	$2.25^{+0.40}_{-0.48}$	52±8	0	-
SPT-CL J0148−6124	27.2474	−61.4148	4.08	0.75	0.92±0.05	$1.99^{+0.31}_{-0.45}$	14±4	0	-
SPT-CL J0149−5947	27.2665	−59.7894	4.58	0.25	0.65±0.02	$2.36^{+0.40}_{-0.51}$	30±5	0	-
SPT-CL J0149−5127	27.3409	−51.4503	4.18	0.25	0.98±0.04	$1.98^{+0.31}_{-0.44}$	23±6	0	-
SPT-CL J0149−6311	27.3928	−63.1919	4.04	0.75	-	-	-	0	-
SPT-CL J0149−5840	27.3979	−58.6792	5.31	0.25	0.41±0.01	$2.86^{+0.48}_{-0.56}$	29±6	0	-
SPT-CL J0149−5608	27.4563	−56.1483	4.88	0.50	0.95±0.03	$2.21^{+0.40}_{-0.47}$	32±6	0	LOS
SPT-CL J0150−5224	27.5406	−52.4142	4.43	0.50	0.64±0.02	$2.33^{+0.39}_{-0.50}$	41±6	0	-
SPT-CL J0150−5003	27.6380	−50.0563	4.77	0.25	0.82±0.02	$2.29^{+0.41}_{-0.48}$	53±8	0	-
SPT-CL J0150−5215	27.6833	−52.2602	4.34	0.50	0.97±0.06	$2.03^{+0.34}_{-0.45}$	14±4	0	-
SPT-CL J0151−5654	27.7780	−56.9147	8.08	0.50	0.293±0.008	$4.02^{+0.52}_{-0.63}$	67±8	0	-
SPT-CL J0151−6526	27.8136	−65.4403	4.40	0.75	-	-	-	0	-
SPT-CL J0151−5848	27.8448	−58.8057	6.24	0.25	0.78±0.03	$2.84^{+0.44}_{-0.50}$	31±7	0	LOS

Table 1 — *Continued*

SPT ID	R.A. (J2000)	Decl. (J2000)	Best ξ	θ_c	Redshift	M_{500c} $(10^{14} h_{70}^{-1} M_\odot)$	λ	*Spitzer*	Notes
SPT-CL J0151−5332	27.8514	−53.5388	4.67	0.25	1.60±0.08	$1.70^{+0.28}_{-0.38}$	23±3	1	LL
SPT-CL J0151−5954	27.8559	−59.9075	13.71	0.25	1.07±0.02	$4.34^{+0.47}_{-0.58}$	100±11	0	-
SPT-CL J0151−6145	27.8957	−61.7535	4.16	0.25	-	-	-	0	-
SPT-CL J0152−5133	28.1295	−51.5510	4.08	0.75	-	-	-	0	-
SPT-CL J0152−5829	28.2060	−58.4845	5.90	0.25	0.73±0.02	$2.77^{+0.45}_{-0.50}$	57±8	0	-
SPT-CL J0152−6437	28.2378	−64.6272	4.01	0.25	0.39±0.01	$2.40^{+0.38}_{-0.52}$	40±6	0	RC
SPT-CL J0152−5303	28.2379	−53.0567	12.60	0.50	0.58±0.01	$4.88^{+0.54}_{-0.67}$	107±11	0	-
SPT-CL J0153−6059	28.2670	−60.9929	4.68	0.25	1.06±0.06	$2.08^{+0.35}_{-0.44}$	22±5	0	-
SPT-CL J0153−5939	28.3719	−59.6523	4.69	0.25	1.12±0.06	$2.03^{+0.35}_{-0.45}$	39±7	0	-
SPT-CL J0153−5827	28.4229	−58.4541	4.13	0.25	0.67±0.02	$2.21^{+0.36}_{-0.49}$	29±6	0	-
SPT-CL J0153−6525	28.4928	−65.4211	5.55	0.25	-	-	-	0	-
SPT-CL J0154−5843	28.5128	−58.7193	4.12	0.50	0.67±0.02	$2.20^{+0.34}_{-0.48}$	38±7	0	-
SPT-CL J0154−6504	28.5660	−65.0788	4.44	0.25	-	-	-	0	-
SPT-CL J0154−5619	28.6214	−56.3236	7.86	0.25	0.79±0.02	$3.34^{+0.44}_{-0.52}$	51±8	0	-
SPT-CL J0154−6409	28.6916	−64.1539	6.70	0.25	1.07±0.06	$2.70^{+0.39}_{-0.46}$	41±4	1	-
SPT-CL J0154−5201	28.6989	−52.0286	4.05	0.25	-	-	-	0	-
SPT-CL J0155−6105	28.7878	−61.0845	4.12	0.25	-	-	-	0	-
SPT-CL J0155−5321	28.9014	−53.3514	4.29	0.50	0.34±0.01	$2.52^{+0.42}_{-0.55}$	39±8	0	-
SPT-CL J0155−5218	28.9896	−52.3088	5.55	0.50	0.70±0.02	$2.67^{+0.45}_{-0.51}$	63±8	0	-
SPT-CL J0156−5541	29.0426	−55.6992	18.69	0.25	1.288	$4.87^{+0.52}_{-0.63}$	50±0	0	RC
SPT-CL J0156−5112	29.0510	−51.2090	4.74	0.75	0.65±0.02	$2.40^{+0.42}_{-0.52}$	31±6	0	-
SPT-CL J0156−6224	29.0598	−62.4107	4.02	0.25	-	-	-	0	-
SPT-CL J0156−5424	29.0937	−54.4062	4.53	0.50	0.41±0.01	$2.55^{+0.44}_{-0.55}$	44±7	0	LOS
SPT-CL J0156−5003	29.1486	−50.0538	4.03	0.25	-	-	-	0	-
SPT-CL J0157−5820	29.3060	−58.3476	9.81	0.50	0.217±0.006	$4.67^{+0.58}_{-0.68}$	69±8	0	-
SPT-CL J0157−6117	29.3653	−61.2964	5.53	0.75	0.35±0.01	$3.00^{+0.50}_{-0.57}$	51±7	0	-
SPT-CL J0157−6425	29.4117	−64.4229	4.35	0.50	0.073±0.006	$2.76^{+0.45}_{-0.60}$	33±6	0	-
SPT-CL J0157−6442	29.4742	−64.7037	8.89	0.25	0.91±0.03	$3.47^{+0.46}_{-0.52}$	26±6	0	-
SPT-CL J0157−5917	29.4835	−59.2867	4.27	0.25	-	-	-	0	-
SPT-CL J0158−5505	29.5343	−55.0964	4.10	1.25	-	-	-	0	-
SPT-CL J0158−5438	29.5691	−54.6350	4.40	1.50	-	-	-	0	-
SPT-CL J0158−5705	29.7120	−57.0980	4.19	1.00	-	-	-	0	-
SPT-CL J0159−5947	29.7881	−59.7922	4.09	0.25	-	-	-	0	-
SPT-CL J0159−6437	29.8483	−64.6238	4.83	0.25	0.73±0.02	$2.37^{+0.41}_{-0.50}$	39±7	0	-
SPT-CL J2201−6105	330.3259	−61.0908	4.08	0.75	-	-	-	0	-
SPT-CL J2201−5620	330.3831	−56.3441	4.89	2.00	1.60±0.08	$1.77^{+0.31}_{-0.39}$	9±2	1	LL
SPT-CL J2201−5956	330.4675	−59.9495	26.11	1.00	0.097	$8.69^{+0.92}_{-1.12}$	142±13	0	-
SPT-CL J2202−5524	330.5098	−55.4102	4.22	0.25	-	-	-	0	-
SPT-CL J2202−5936	330.5514	−59.6020	5.67	0.25	0.44±0.01	$2.97^{+0.49}_{-0.55}$	45±8	0	-
SPT-CL J2202−5603	330.6143	−56.0649	4.06	0.25	1.14±0.06	$1.87^{+0.28}_{-0.41}$	19±5	0	-
SPT-CL J2202−6346	330.6872	−63.7758	4.56	0.50	-	-	-	0	-
SPT-CL J2202−6308	330.7357	−63.1481	4.01	0.25	-	-	-	0	-
SPT-CL J2203−6055	330.7531	−60.9186	5.53	0.25	0.413±0.009	$2.93^{+0.49}_{-0.57}$	83±9	0	-
SPT-CL J2203−5735	330.7619	−57.5977	4.62	0.25	0.95±0.03	$2.13^{+0.37}_{-0.47}$	53±8	0	-
SPT-CL J2203−5047	330.8042	−50.7861	10.68	0.25	0.94±0.02	$3.88^{+0.46}_{-0.55}$	56±9	0	-
SPT-CL J2203−5641	330.8305	−56.6834	4.05	0.50	-	-	-	0	-
SPT-CL J2203−5042	330.9236	−50.7044	4.04	0.25	-	-	-	0	-
SPT-CL J2204−5300	331.1467	−53.0118	4.03	0.50	0.87±0.03	$2.04^{+0.31}_{-0.44}$	31±6	0	-
SPT-CL J2204−5059	331.1949	−50.9870	4.28	0.25	0.084±0.008	$2.73^{+0.44}_{-0.58}$	19±5	0	-
SPT-CL J2204−5340	331.2069	−53.6722	6.33	0.25	0.93±0.03	$2.69^{+0.45}_{-0.47}$	34±7	0	LOS
SPT-CL J2204−6223	331.2076	−62.3834	6.34	0.50	0.279±0.009	$3.41^{+0.50}_{-0.60}$	56±8	0	-
SPT-CL J2205−5927	331.2582	−59.4525	11.47	0.50	0.349±0.008	$4.96^{+0.58}_{-0.69}$	84±9	0	LOS
SPT-CL J2205−5705	331.3290	−57.0884	4.05	1.25	0.28±0.01	$2.50^{+0.41}_{-0.55}$	40±6	0	-
SPT-CL J2205−6310	331.3809	−63.1708	4.66	0.25	0.83±0.04	$2.24^{+0.38}_{-0.49}$	18±5	0	-
SPT-CL J2205−5142	331.4881	−51.7090	4.17	0.25	-	-	-	0	-
SPT-CL J2206−5528	331.5163	−55.4724	5.00	0.25	0.57±0.02	$2.56^{+0.46}_{-0.53}$	36±7	0	-
SPT-CL J2206−5820	331.6166	−58.3429	5.00	0.25	0.69±0.04	$2.47^{+0.43}_{-0.51}$	12±4	0	-
SPT-CL J2206−5808	331.6486	−58.1347	11.65	0.75	0.59±0.01	$4.63^{+0.52}_{-0.65}$	90±10	0	LOS
SPT-CL J2206−6407	331.6509	−64.1270	6.00	0.25	1.13±0.06	$2.44^{+0.39}_{-0.44}$	26±6	0	-
SPT-CL J2206−5919	331.6748	−59.3248	5.60	0.25	0.77±0.02	$2.62^{+0.44}_{-0.50}$	48±8	0	-
SPT-CL J2206−5558	331.7366	−55.9730	4.52	0.25	0.40±0.02	$2.57^{+0.43}_{-0.55}$	15±4	0	-
SPT-CL J2207−5105	331.8744	−51.0958	4.28	0.25	1.04±0.06	$1.96^{+0.32}_{-0.44}$	11±6	0	-
SPT-CL J2207−5522	331.8976	−55.3685	5.48	0.50	0.87±0.03	$2.49^{+0.42}_{-0.48}$	26±6	0	-

BLEEM ET AL.

Table 1 — *Continued*

SPT ID	R.A. (J2000)	Decl. (J2000)	Best ξ	θ_c	Redshift	M_{500c} $(10^{14}h_{70}^{-1}M_\odot)$	λ	*Spitzer*	Notes
SPT-CL J2207−5056	331.9763	−50.9445	5.22	0.25	0.38±0.01	$2.84^{+0.49}_{-0.56}$	37±6	0	-
SPT-CL J2207−5136	331.9937	−51.6078	4.06	0.25	-	-	-	0	-
SPT-CL J2209−6350	332.2544	−63.8423	4.11	1.25	0.47±0.02	$2.37^{+0.38}_{-0.52}$	31±6	0	-
SPT-CL J2209−5807	332.3182	−58.1237	4.88	0.25	1.04±0.06	$2.14^{+0.38}_{-0.46}$	10±3	1	-
SPT-CL J2209−5940	332.3285	−59.6756	4.26	0.25	0.264±0.009	$2.58^{+0.42}_{-0.56}$	48±7	0	-
SPT-CL J2209−5148	332.3422	−51.8033	7.69	1.25	0.110	$4.11^{+0.54}_{-0.67}$	41±7	0	-
SPT-CL J2209−5622	332.3739	−56.3690	4.05	0.25	1.10±0.06	$1.87^{+0.29}_{-0.41}$	29±6	0	-
SPT-CL J2209−5801	332.4042	−58.0305	4.04	0.75	1.04±0.05	$1.92^{+0.29}_{-0.42}$	17±6	0	-
SPT-CL J2209−5002	332.4509	−50.0455	4.23	0.50	1.44±0.07	$1.71^{+0.26}_{-0.38}$	22±6	0	-
SPT-CL J2210−6347	332.5159	−63.7939	4.00	0.25	-	-	-	0	-
SPT-CL J2210−6500	332.5375	−65.0160	6.04	0.25	1.52±0.08	$2.14^{+0.36}_{-0.40}$	45±4	1	LOS
SPT-CL J2210−5709	332.6261	−57.1640	7.52	0.50	0.301±0.008	$3.81^{+0.52}_{-0.63}$	71±9	0	-
SPT-CL J2210−6046	332.7304	−60.7747	4.18	0.25	0.49±0.03	$2.36^{+0.38}_{-0.52}$	10±4	0	-
SPT-CL J2212−6249	333.1006	−62.8198	5.12	0.50	0.84±0.04	$2.37^{+0.42}_{-0.49}$	20±5	0	-
SPT-CL J2212−5010	333.1814	−50.1772	4.28	0.25	0.78±0.04	$2.17^{+0.36}_{-0.47}$	14±5	0	-
SPT-CL J2212−5228	333.2036	−52.4717	4.68	0.75	0.58±0.03	$2.45^{+0.43}_{-0.53}$	12±4	0	-
SPT-CL J2212−5335	333.2299	−53.5938	4.60	1.25	0.205±0.010	$2.75^{+0.48}_{-0.59}$	30±6	0	-
SPT-CL J2212−5434	333.2302	−54.5769	4.22	0.50	0.67±0.02	$2.24^{+0.37}_{-0.49}$	53±8	0	-
SPT-CL J2212−5616	333.2488	−56.2754	4.65	2.00	-	-	-	0	-
SPT-CL J2213−5024	333.4050	−50.4051	4.55	0.50	-	-	-	0	-
SPT-CL J2213−5150	333.4391	−51.8407	6.78	0.25	0.65±0.02	$3.16^{+0.43}_{-0.53}$	54±8	0	-
SPT-CL J2214−5501	333.5288	−55.0293	5.17	0.25	1.24±0.07	$2.07^{+0.36}_{-0.44}$	49±4	1	-
SPT-CL J2215−5204	333.7659	−52.0807	5.35	0.75	0.51±0.01	$2.77^{+0.48}_{-0.54}$	54±8	0	-
SPT-CL J2215−5252	333.8019	−52.8702	4.03	0.25	-	-	-	0	-
SPT-CL J2215−5119	333.9097	−51.3244	4.54	1.00	0.49±0.02	$2.49^{+0.42}_{-0.54}$	30±6	0	-
SPT-CL J2216−5705	334.0237	−57.0925	4.38	0.25	0.65±0.02	$2.30^{+0.38}_{-0.50}$	58±8	0	-
SPT-CL J2216−6421	334.1965	−64.3610	4.47	0.50	1.00±0.06	$2.05^{+0.34}_{-0.45}$	13±6	0	-
SPT-CL J2216−6422	334.2234	−64.3709	4.26	0.25	-	-	-	0	-
SPT-CL J2217−5431	334.3092	−54.5240	6.22	0.25	1.06±0.03	$2.57^{+0.40}_{-0.46}$	68±10	0	-
SPT-CL J2217−5524	334.4391	−55.4083	6.00	0.25	1.02±0.06	$2.55^{+0.39}_{-0.45}$	35±4	1	-
SPT-CL J2217−6510	334.4880	−65.1749	9.46	1.25	0.095	$4.74^{+0.59}_{-0.70}$	66±9	0	-
SPT-CL J2217−5652	334.4942	−56.8718	4.25	2.25	-	-	-	0	-
SPT-CL J2218−5533	334.5298	−55.5525	8.42	0.25	0.98±0.03	$3.28^{+0.41}_{-0.50}$	39±8	0	-
SPT-CL J2218−5008	334.5761	−50.1496	5.35	0.25	1.52±0.08	$1.93^{+0.35}_{-0.40}$	18±3	1	-
SPT-CL J2218−5232	334.5780	−52.5424	4.40	0.25	-	-	-	0	-
SPT-CL J2218−5402	334.6165	−54.0460	4.29	0.75	-	-	-	0	-
SPT-CL J2218−5405	334.7446	−54.0929	4.69	0.25	1.28±0.07	$1.90^{+0.33}_{-0.42}$	39±4	1	-
SPT-CL J2219−5239	334.8425	−52.6662	4.33	1.50	-	-	-	0	-
SPT-CL J2219−6005	334.8464	−60.0984	4.12	1.00	1.00±0.04	$1.96^{+0.31}_{-0.43}$	26±10	0	LOS
SPT-CL J2219−5708	334.9564	−57.1431	13.46	0.50	0.296±0.007	$5.57^{+0.61}_{-0.76}$	106±10	0	-
SPT-CL J2219−5816	334.9954	−58.2698	4.84	0.25	0.29±0.01	$2.77^{+0.46}_{-0.57}$	31±6	0	-
SPT-CL J2220−5228	335.0381	−52.4786	4.77	1.25	0.092±0.005	$2.91^{+0.49}_{-0.61}$	55±8	0	-
SPT-CL J2220−5159	335.1961	−51.9931	6.94	0.25	0.49±0.02	$3.39^{+0.47}_{-0.56}$	39±7	0	-
SPT-CL J2221−5631	335.4261	−56.5322	4.91	0.25	0.48±0.02	$2.62^{+0.45}_{-0.56}$	31±6	0	-
SPT-CL J2221−5345	335.4376	−53.7550	4.90	0.25	1.60±0.08	$1.77^{+0.31}_{-0.38}$	12±3	1	LL
SPT-CL J2222−6106	335.5123	−61.1092	4.18	0.50	0.30±0.01	$2.53^{+0.39}_{-0.55}$	37±6	0	-
SPT-CL J2222−5105	335.7226	−51.0882	5.02	0.25	1.57±0.08	$1.80^{+0.32}_{-0.39}$	22±3	1	-
SPT-CL J2223−5228	335.8490	−52.4684	9.04	1.25	0.265±0.007	$4.36^{+0.54}_{-0.66}$	85±9	0	-
SPT-CL J2223−5604	335.8969	−56.0719	4.33	0.25	-	-	-	0	-
SPT-CL J2224−5039	336.0727	−50.6509	4.24	0.75	0.33±0.01	$2.52^{+0.42}_{-0.55}$	31±6	0	-
SPT-CL J2224−5420	336.1979	−54.3351	4.04	1.00	-	-	-	0	-
SPT-CL J2225−6526	336.2697	−65.4345	10.09	0.75	0.66±0.01	$4.11^{+0.51}_{-0.60}$	91±10	0	-
SPT-CL J2225−6120	336.3334	−61.3421	4.62	0.50	-	-	-	0	-
SPT-CL J2225−6131	336.4801	−61.5171	4.43	0.75	0.175±0.009	$2.71^{+0.45}_{-0.59}$	28±5	0	-
SPT-CL J2226−5714	336.5119	−57.2414	4.01	1.50	0.128±0.007	$2.61^{+0.42}_{-0.56}$	33±6	0	-
SPT-CL J2226−5214	336.6484	−52.2420	4.18	0.75	-	-	-	0	-
SPT-CL J2227−6220	336.9977	−62.3345	7.37	0.25	0.63±0.02	$3.37^{+0.47}_{-0.55}$	64±8	0	-
SPT-CL J2228−6513	337.1396	−65.2240	5.78	0.25	0.59±0.02	$2.85^{+0.48}_{-0.52}$	35±6	0	LOS
SPT-CL J2228−5158	337.1944	−51.9822	4.14	0.75	0.65±0.02	$2.24^{+0.36}_{-0.49}$	29±6	0	-
SPT-CL J2228−5828	337.2109	−58.4731	9.92	1.00	0.74±0.02	$3.95^{+0.50}_{-0.58}$	86±10	0	-
SPT-CL J2230−6300	337.5477	−63.0111	5.04	0.25	1.10±0.06	$2.15^{+0.38}_{-0.44}$	34±4	1	-

Table 1 — *Continued*

SPT ID	R.A. (J2000)	Decl. (J2000)	Best ξ	Best θ_c	Redshift	M_{500c} $(10^{14} h_{70}^{-1} M_\odot)$	λ	*Spitzer*	Notes
SPT-CL J2230−5048	337.5504	−50.8037	4.11	0.75	-	-	-	0	-
SPT-CL J2230−6340	337.6580	−63.6806	10.95	0.25	0.65±0.02	$4.34^{+0.52}_{-0.63}$	34±6	0	LOS
SPT-CL J2230−5239	337.6775	−52.6575	6.13	0.75	0.58±0.02	$3.01^{+0.45}_{-0.53}$	49±8	0	-
SPT-CL J2230−5634	337.6822	−56.5756	4.18	1.00	1.25±0.07	$1.82^{+0.27}_{-0.39}$	29±6	0	-
SPT-CL J2230−5826	337.6930	−58.4452	4.18	0.50	-	-	-	0	-
SPT-CL J2230−5339	337.7122	−53.6578	4.59	0.50	-	-	-	0	-
SPT-CL J2230−5748	337.7151	−57.8048	4.95	0.25	0.80±0.03	$2.37^{+0.40}_{-0.49}$	20±6	0	-
SPT-CL J2232−5959	338.1419	−59.9972	17.15	0.25	0.595	$5.85^{+0.63}_{-0.77}$	123±11	0	-
SPT-CL J2232−5216	338.1555	−52.2691	5.33	0.50	1.37±0.07	$2.04^{+0.35}_{-0.41}$	21±3	1	LOS
SPT-CL J2232−6301	338.1787	−63.0171	4.76	0.25	0.53±0.02	$2.52^{+0.44}_{-0.54}$	43±6	0	-
SPT-CL J2232−5358	338.2050	−53.9681	6.08	0.50	0.44±0.01	$3.12^{+0.47}_{-0.55}$	48±7	0	-
SPT-CL J2233−4951	338.3154	−49.8562	6.62	0.25	0.72±0.02	$3.02^{+0.45}_{-0.51}$	80±9	0	-
SPT-CL J2233−5339	338.3272	−53.6512	14.30	1.00	0.440	$5.52^{+0.62}_{-0.75}$	107±11	0	-
SPT-CL J2233−5552	338.4056	−55.8770	6.26	0.25	1.06±0.06	$2.58^{+0.40}_{-0.45}$	39±7	0	-
SPT-CL J2234−5849	338.6376	−58.8223	4.40	0.25	-	-	-	0	-
SPT-CL J2234−6029	338.7367	−60.4839	5.38	0.25	0.67±0.02	$2.63^{+0.45}_{-0.51}$	33±7	0	-
SPT-CL J2234−5740	338.7432	−57.6673	5.02	0.25	0.47±0.02	$2.67^{+0.46}_{-0.56}$	26±5	0	-
SPT-CL J2235−5252	338.7981	−52.8709	4.16	0.25	-	-	-	0	-
SPT-CL J2235−5213	338.8268	−52.2202	4.82	1.75	0.53±0.02	$2.54^{+0.43}_{-0.54}$	36±7	0	-
SPT-CL J2235−5157	338.8578	−51.9534	5.54	0.25	1.03±0.03	$2.36^{+0.43}_{-0.44}$	50±8	0	-
SPT-CL J2236−5315	339.0131	−53.2596	4.25	0.25	1.04±0.04	$1.97^{+0.31}_{-0.44}$	27±6	0	LOS
SPT-CL J2236−5344	339.0388	−53.7471	5.89	1.25	0.45±0.01	$3.05^{+0.48}_{-0.56}$	43±8	0	-
SPT-CL J2236−6041	339.1794	−60.6969	4.08	0.75	1.55±0.07	$1.60^{+0.25}_{-0.36}$	13±5	0	-
SPT-CL J2237−5426	339.4693	−54.4351	4.39	0.25	0.17±0.01	$2.70^{+0.46}_{-0.59}$	20±5	0	-
SPT-CL J2237−5406	339.4800	−54.1010	7.42	0.75	0.40±0.01	$3.68^{+0.49}_{-0.59}$	56±8	0	-
SPT-CL J2238−5722	339.5596	−57.3707	4.36	0.25	-	-	-	0	-
SPT-CL J2238−6019	339.5601	−60.3289	4.20	0.25	0.50±0.03	$2.35^{+0.38}_{-0.52}$	16±5	0	-
SPT-CL J2238−6138	339.6819	−61.6425	4.45	0.50	0.168±0.010	$2.72^{+0.46}_{-0.60}$	24±5	0	-
SPT-CL J2238−6245	339.7367	−62.7595	4.10	0.25	1.24±0.07	$1.79^{+0.29}_{-0.41}$	28±6	0	-
SPT-CL J2239−5409	339.7978	−54.1509	4.33	0.25	-	-	-	0	-
SPT-CL J2239−5415	339.9061	−54.2562	4.39	1.25	0.45±0.02	$2.46^{+0.40}_{-0.54}$	29±6	0	-
SPT-CL J2239−5042	339.9902	−50.7053	4.31	0.50	0.69±0.02	$2.24^{+0.36}_{-0.49}$	43±8	0	-
SPT-CL J2240−6117	340.0204	−61.2957	7.05	0.50	0.95±0.02	$2.93^{+0.39}_{-0.48}$	65±9	0	-
SPT-CL J2241−5338	340.3322	−53.6443	7.64	0.25	0.93±0.02	$3.12^{+0.41}_{-0.50}$	69±9	0	-
SPT-CL J2242−5150	340.6446	−51.8453	4.58	0.50	0.75±0.03	$2.27^{+0.37}_{-0.50}$	24±6	0	-
SPT-CL J2243−5158	340.7582	−51.9818	4.42	0.50	0.47±0.02	$2.46^{+0.42}_{-0.54}$	36±6	0	LOS
SPT-CL J2243−5335	340.7780	−53.5881	6.52	0.75	0.44±0.01	$3.29^{+0.48}_{-0.57}$	67±8	0	-
SPT-CL J2243−5821	340.9549	−58.3610	7.48	0.75	1.13±0.06	$2.87^{+0.39}_{-0.45}$	59±5	1	-
SPT-CL J2244−5908	341.1715	−59.1403	4.22	0.25	0.88±0.03	$2.08^{+0.34}_{-0.45}$	40±7	0	LOS
SPT-CL J2244−6420	341.2154	−64.3362	4.03	0.25	-	-	-	0	-
SPT-CL J2245−5711	341.2580	−57.1960	4.19	0.25	0.48±0.01	$2.39^{+0.38}_{-0.52}$	43±7	0	-
SPT-CL J2245−6207	341.2584	−62.1178	18.70	0.50	0.586	$6.18^{+0.67}_{-0.81}$	112±11	0	RC
SPT-CL J2245−5023	341.2681	−50.3950	4.21	1.50	-	-	-	0	-
SPT-CL J2245−5723	341.3018	−57.3899	6.67	0.25	0.50±0.02	$3.28^{+0.47}_{-0.56}$	29±6	0	-
SPT-CL J2245−5358	341.3774	−53.9734	5.36	0.25	0.92±0.03	$2.39^{+0.45}_{-0.47}$	45±8	0	-
SPT-CL J2245−5354	341.3798	−53.9158	4.97	0.25	0.95±0.03	$2.24^{+0.40}_{-0.47}$	34±6	0	-
SPT-CL J2245−6458	341.3929	−64.9787	5.52	0.25	1.47±0.07	$2.03^{+0.34}_{-0.40}$	30±4	1	-
SPT-CL J2245−6009	341.4516	−60.1568	4.73	0.25	1.47±0.07	$1.80^{+0.30}_{-0.40}$	20±3	1	-
SPT-CL J2245−5254	341.4637	−52.9109	5.42	0.25	0.46±0.01	$2.85^{+0.47}_{-0.55}$	40±7	0	-
SPT-CL J2245−6113	341.4864	−61.2316	4.59	0.25	0.77±0.02	$2.26^{+0.39}_{-0.49}$	35±7	0	-
SPT-CL J2246−5243	341.5638	−52.7302	8.41	2.25	0.102±0.003	$4.38^{+0.55}_{-0.67}$	96±10	0	RC
SPT-CL J2246−5308	341.5670	−53.1338	4.96	0.25	1.43±0.07	$1.89^{+0.34}_{-0.41}$	41±7	0	-
SPT-CL J2246−6046	341.5810	−60.7755	4.10	0.50	0.41±0.01	$2.40^{+0.40}_{-0.53}$	30±6	0	-
SPT-CL J2246−6234	341.5916	−62.5697	4.35	0.25	0.75±0.03	$2.21^{+0.37}_{-0.48}$	19±5	0	-
SPT-CL J2246−5130	341.6475	−51.5103	7.08	0.75	0.66±0.02	$3.25^{+0.45}_{-0.53}$	42±7	0	-
SPT-CL J2246−5925	341.7126	−59.4303	4.49	0.25	1.01±0.03	$2.05^{+0.35}_{-0.45}$	43±8	0	RC
SPT-CL J2247−5715	341.7897	−57.2546	5.21	0.50	1.28±0.07	$2.05^{+0.36}_{-0.43}$	43±4	1	-
SPT-CL J2247−5139	341.8433	−51.6533	4.36	0.25	-	-	-	0	-
SPT-CL J2247−5537	341.8992	−55.6304	7.10	0.25	0.93±0.05	$2.96^{+0.40}_{-0.48}$	13±5	0	-
SPT-CL J2248−5425	342.1721	−54.4325	4.68	0.25	0.85±0.03	$2.23^{+0.39}_{-0.48}$	33±6	0	-

BLEEM ET AL.

Table 1 — *Continued*

SPT ID	R.A. (J2000)	Decl. (J2000)	Best ξ	θ_c	Redshift	M_{500c} $(10^{14}h_{70}^{-1}M_\odot)$	λ	*Spitzer*	Notes
SPT-CL J2249−6426	342.4579	−64.4379	8.18	1.25	0.094	$4.31^{+0.56}_{-0.68}$	78±9	0	-
SPT-CL J2249−5528	342.4697	−55.4831	5.04	0.25	1.20±0.07	$2.07^{+0.37}_{-0.43}$	23±3	1	-
SPT-CL J2250−5345	342.6720	−53.7555	4.26	0.25	0.52±0.01	$2.37^{+0.39}_{-0.52}$	52±8	0	-
SPT-CL J2251−5257	342.8053	−52.9563	5.12	0.25	1.12±0.06	$2.16^{+0.39}_{-0.45}$	37±6	0	-
SPT-CL J2251−5246	342.8300	−52.7781	5.20	0.50	0.93±0.03	$2.34^{+0.40}_{-0.47}$	36±7	0	-
SPT-CL J2251−5403	342.8682	−54.0533	5.91	0.25	0.49±0.02	$3.00^{+0.47}_{-0.56}$	24±5	0	LOS
SPT-CL J2251−5049	342.9807	−50.8188	5.66	0.25	0.86±0.03	$2.54^{+0.44}_{-0.49}$	30±6	0	-
SPT-CL J2252−6011	343.0828	−60.1969	5.97	0.25	1.10±0.06	$2.45^{+0.40}_{-0.45}$	39±7	0	-
SPT-CL J2252−5720	343.1045	−57.3373	4.38	1.00	1.43±0.07	$1.74^{+0.28}_{-0.39}$	15±4	0	-
SPT-CL J2252−5737	343.1610	−57.6258	4.45	0.25	1.01±0.04	$2.05^{+0.34}_{-0.44}$	32±7	0	-
SPT-CL J2253−5247	343.3036	−52.7870	4.45	0.25	0.79±0.03	$2.21^{+0.36}_{-0.49}$	19±5	0	-
SPT-CL J2253−5408	343.3323	−54.1419	5.99	0.50	0.78±0.03	$2.77^{+0.43}_{-0.49}$	21±6	0	-
SPT-CL J2254−6314	343.5099	−63.2484	15.57	0.75	0.211	$6.22^{+0.70}_{-0.82}$	80±10	0	-
SPT-CL J2254−6142	343.5547	−61.7067	4.21	0.25	0.92±0.04	$2.04^{+0.34}_{-0.45}$	23±6	0	-
SPT-CL J2254−5804	343.5842	−58.0804	5.74	2.25	0.153	$3.27^{+0.53}_{-0.61}$	32±6	0	-
SPT-CL J2255−5747	343.8958	−57.7935	4.55	0.75	1.05±0.05	$2.04^{+0.34}_{-0.45}$	21±5	0	-
SPT-CL J2256−6149	344.0089	−61.8259	4.48	0.25	0.34±0.01	$2.58^{+0.45}_{-0.56}$	34±6	0	-
SPT-CL J2256−5821	344.1214	−58.3647	4.24	0.25	-	-	-	0	-
SPT-CL J2256−5102	344.1636	−51.0495	4.05	0.25	-	-	-	0	-
SPT-CL J2256−6246	344.1898	−62.7703	5.07	0.25	1.13±0.06	$2.13^{+0.37}_{-0.44}$	36±4	1	-
SPT-CL J2257−5111	344.4303	−51.1863	4.05	0.25	-	-	-	0	-
SPT-CL J2258−5443	344.5558	−54.7271	4.21	2.50	0.30±0.02	$2.54^{+0.40}_{-0.54}$	13±4	0	-
SPT-CL J2258−6057	344.7486	−60.9582	19.71	0.25	0.79±0.01	$5.94^{+0.62}_{-0.76}$	114±11	0	RC,LOS
SPT-CL J2259−5232	344.7604	−52.5360	4.68	0.50	0.97±0.04	$2.13^{+0.38}_{-0.47}$	19±6	0	-
SPT-CL J2259−5349	344.7875	−53.8219	5.88	0.75	0.271±0.009	$3.21^{+0.50}_{-0.59}$	47±8	0	LOS
SPT-CL J2259−5957	344.9537	−59.9554	4.10	1.50	-	-	-	0	-
SPT-CL J2259−5431	344.9798	−54.5280	9.00	0.50	0.42±0.01	$4.15^{+0.52}_{-0.63}$	39±7	0	-
SPT-CL J2300−5617	345.0042	−56.2869	8.98	0.50	0.153	$4.50^{+0.56}_{-0.67}$	56±8	0	RC
SPT-CL J2300−5331	345.1699	−53.5200	10.27	1.00	0.262	$4.77^{+0.54}_{-0.69}$	76±9	0	-
SPT-CL J2301−5316	345.3374	−53.2793	5.72	0.75	0.37±0.01	$3.05^{+0.50}_{-0.56}$	39±7	0	-
SPT-CL J2301−6055	345.4512	−60.9230	6.78	0.25	0.72±0.02	$3.08^{+0.45}_{-0.52}$	68±8	0	-
SPT-CL J2301−5546	345.4595	−55.7786	5.68	0.50	0.748	$2.69^{+0.43}_{-0.50}$	55±8	0	RC
SPT-CL J2302−5117	345.6072	−51.2907	4.19	1.00	-	-	-	0	-
SPT-CL J2302−5405	345.6581	−54.0881	4.17	0.25	0.76±0.03	$2.16^{+0.35}_{-0.48}$	24±6	0	-
SPT-CL J2303−6335	345.9664	−63.5889	4.39	0.50	0.72±0.03	$2.24^{+0.38}_{-0.49}$	29±6	0	-
SPT-CL J2303−5600	345.9695	−56.0053	4.22	0.75	-	-	-	0	-
SPT-CL J2303−5006	345.9992	−50.1107	6.08	0.50	0.64±0.02	$2.92^{+0.46}_{-0.53}$	36±7	0	-
SPT-CL J2304−5149	346.0677	−51.8328	4.02	0.25	1.52±0.08	$1.63^{+0.25}_{-0.35}$	14±3	1	-
SPT-CL J2304−5718	346.0967	−57.3094	5.71	0.25	0.92±0.03	$2.52^{+0.42}_{-0.47}$	30±7	0	-
SPT-CL J2305−6524	346.3119	−65.4084	4.26	0.50	-	-	-	0	-
SPT-CL J2305−5130	346.4023	−51.5099	4.42	0.25	0.66±0.02	$2.30^{+0.39}_{-0.50}$	36±7	0	LOS
SPT-CL J2306−5120	346.6130	−51.3421	7.56	0.25	1.17±0.07	$2.86^{+0.36}_{-0.45}$	36±4	1	-
SPT-CL J2306−6505	346.7210	−65.0939	13.66	0.75	0.530	$5.21^{+0.58}_{-0.71}$	121±11	0	-
SPT-CL J2307−5440	346.7911	−54.6689	5.01	0.50	0.70±0.02	$2.46^{+0.43}_{-0.51}$	51±8	0	LOS
SPT-CL J2307−6521	346.8902	−65.3591	4.33	0.50	0.53±0.01	$2.39^{+0.38}_{-0.53}$	53±12	0	-
SPT-CL J2307−5412	346.9352	−54.2038	4.30	0.25	0.76±0.03	$2.19^{+0.36}_{-0.48}$	26±6	0	-
SPT-CL J2308−5133	347.0677	−51.5547	4.17	0.25	-	-	-	0	-
SPT-CL J2308−5413	347.1451	−54.2220	4.41	0.75	0.66±0.02	$2.30^{+0.38}_{-0.51}$	58±8	0	-
SPT-CL J2308−5710	347.2451	−57.1794	5.34	0.50	0.40±0.02	$2.88^{+0.47}_{-0.55}$	23±5	0	-
SPT-CL J2309−5301	347.3109	−53.0172	4.98	0.75	-	-	-	0	-
SPT-CL J2309−5532	347.3208	−55.5467	4.01	3.00	-	-	-	0	-
SPT-CL J2309−6048	347.3955	−60.8018	4.53	0.25	-	-	-	0	-
SPT-CL J2310−4951	347.5532	−49.8563	4.96	0.50	0.57±0.02	$2.56^{+0.45}_{-0.53}$	25±6	0	-
SPT-CL J2310−5919	347.5604	−59.3194	5.73	0.50	0.75±0.02	$2.69^{+0.44}_{-0.50}$	42±7	0	-
SPT-CL J2311−6225	347.7535	−62.4243	5.23	0.25	0.77±0.02	$2.47^{+0.43}_{-0.50}$	37±7	0	-
SPT-CL J2311−5549	347.8682	−55.8172	4.02	1.00	0.57±0.02	$2.25^{+0.35}_{-0.50}$	34±6	0	LOS
SPT-CL J2311−5522	347.8924	−55.3691	6.81	0.75	0.203±0.008	$3.68^{+0.52}_{-0.62}$	38±6	0	-
SPT-CL J2311−5411	347.9754	−54.1902	4.03	1.75	-	-	-	0	-
SPT-CL J2311−5820	347.9979	−58.3402	4.49	0.25	0.84±0.03	$2.18^{+0.35}_{-0.48}$	39±6	0	-
SPT-CL J2312−6117	348.1590	−61.2917	4.55	0.25	0.81±0.03	$2.22^{+0.36}_{-0.48}$	30±6	0	-
SPT-CL J2313−6102	348.3466	−61.0381	5.84	0.25	1.09±0.03	$2.40^{+0.42}_{-0.43}$	37±7	0	-

Table 1 — *Continued*

SPT ID	R.A. (J2000)	Decl. (J2000)	ξ	θ_c	Redshift	M_{500c} $(10^{14}h_{70}^{-1}M_\odot)$	λ	*Spitzer*	Notes
SPT-CL J2313−6224	348.4324	−62.4107	4.18	0.25	-	-	-	0	-
SPT-CL J2313−6428	348.4898	−64.4746	4.06	1.25	-	-	-	0	-
SPT-CL J2314−5747	348.5009	−57.7929	4.41	0.25	0.87±0.03	$2.14^{+0.35}_{-0.46}$	25±6	0	-
SPT-CL J2314−6036	348.5118	−60.6158	4.11	0.75	-	-	-	0	-
SPT-CL J2314−5553	348.5243	−55.8984	4.90	0.25	0.71±0.04	$2.42^{+0.41}_{-0.51}$	13±4	0	-
SPT-CL J2314−5245	348.5572	−52.7514	4.53	0.25	1.07±0.05	$2.02^{+0.34}_{-0.45}$	20±6	0	-
SPT-CL J2316−5535	349.0204	−55.5974	4.17	0.75	0.22±0.01	$2.58^{+0.42}_{-0.57}$	20±5	0	-
SPT-CL J2316−5534	349.1689	−55.5684	4.26	0.75	-	-	-	0	-
SPT-CL J2316−5907	349.1772	−59.1173	6.67	0.50	0.84±0.03	$2.92^{+0.42}_{-0.50}$	29±6	0	-
SPT-CL J2316−5027	349.1901	−50.4517	5.44	0.50	1.28±0.07	$2.14^{+0.37}_{-0.42}$	26±4	1	-
SPT-CL J2316−5454	349.2141	−54.9028	10.16	0.75	0.37±0.01	$4.55^{+0.54}_{-0.67}$	52±7	0	-
SPT-CL J2316−5822	349.2216	−58.3675	4.19	0.50	-	-	-	0	-
SPT-CL J2317−4959	349.3195	−49.9977	5.02	0.50	1.05±0.03	$2.17^{+0.39}_{-0.46}$	41±8	0	LOS
SPT-CL J2317−5852	349.4413	−58.8799	4.40	0.50	0.58±0.02	$2.36^{+0.39}_{-0.51}$	32±6	0	-
SPT-CL J2318−5058	349.5349	−50.9796	4.52	0.75	0.37±0.02	$2.58^{+0.43}_{-0.55}$	18±5	0	-
SPT-CL J2318−5617	349.7071	−56.2862	6.47	0.25	0.55±0.01	$3.15^{+0.45}_{-0.55}$	54±8	0	-
SPT-CL J2319−5404	349.8139	−54.0784	4.10	0.25	0.276±0.009	$2.52^{+0.39}_{-0.55}$	47±7	0	-
SPT-CL J2319−6404	349.8674	−64.0730	4.17	0.25	-	-	-	0	-
SPT-CL J2319−5842	349.8745	−58.7103	7.11	0.50	0.30±0.01	$3.67^{+0.50}_{-0.61}$	28±6	0	-
SPT-CL J2320−6430	350.0423	−64.5146	5.24	0.25	0.88±0.05	$2.39^{+0.42}_{-0.48}$	12±5	0	-
SPT-CL J2320−5823	350.0509	−58.3987	4.05	0.25	-	-	-	0	-
SPT-CL J2320−6443	350.0567	−64.7285	4.88	0.25	0.80±0.03	$2.33^{+0.41}_{-0.50}$	32±7	0	LOS
SPT-CL J2320−5808	350.0755	−58.1337	6.98	0.50	0.54±0.02	$3.34^{+0.46}_{-0.56}$	35±7	0	-
SPT-CL J2320−5233	350.1251	−52.5614	6.53	0.25	0.76±0.02	$2.94^{+0.45}_{-0.50}$	66±8	0	-
SPT-CL J2321−5120	350.2922	−51.3484	4.77	0.50	0.62±0.02	$2.44^{+0.42}_{-0.52}$	42±7	0	-
SPT-CL J2321−5419	350.4100	−54.3229	4.08	0.25	0.80±0.04	$2.10^{+0.34}_{-0.46}$	14±5	0	-
SPT-CL J2321−5558	350.4379	−55.9800	4.32	1.00	0.72±0.02	$2.23^{+0.38}_{-0.48}$	34±6	0	-
SPT-CL J2322−5708	350.5600	−57.1426	4.06	0.25	-	-	-	0	-
SPT-CL J2323−5752	350.8837	−57.8770	5.99	0.25	1.20±0.07	$2.38^{+0.38}_{-0.43}$	27±4	1	-
SPT-CL J2323−5657	350.8988	−56.9593	4.03	0.25	0.41±0.01	$2.41^{+0.38}_{-0.52}$	43±7	0	-
SPT-CL J2323−6529	350.9346	−65.4885	4.28	0.25	0.88±0.03	$2.11^{+0.33}_{-0.45}$	33±7	0	-
SPT-CL J2323−5126	350.9521	−51.4432	4.36	0.25	0.71±0.03	$2.25^{+0.37}_{-0.49}$	16±5	0	-
SPT-CL J2323−5453	350.9582	−54.8953	4.01	0.25	0.83±0.02	$2.06^{+0.33}_{-0.46}$	45±7	0	-
SPT-CL J2324−6354	351.2028	−63.9152	4.47	0.25	0.88±0.03	$2.15^{+0.36}_{-0.47}$	23±6	0	-
SPT-CL J2325−5129	351.3398	−51.4984	4.28	3.00	-	-	-	0	-
SPT-CL J2325−5815	351.3437	−58.2548	4.88	0.25	0.56±0.02	$2.54^{+0.43}_{-0.53}$	48±8	0	-
SPT-CL J2325−6215	351.3732	−62.2548	4.58	1.00	0.55±0.02	$2.44^{+0.41}_{-0.53}$	36±7	0	-
SPT-CL J2325−5116	351.3875	−51.2821	4.50	0.25	0.87±0.03	$2.16^{+0.36}_{-0.48}$	22±5	0	-
SPT-CL J2325−5316	351.4227	−53.2811	5.13	0.25	0.37±0.01	$2.80^{+0.48}_{-0.56}$	32±6	0	LOS
SPT-CL J2326−5027	351.5127	−50.4534	4.28	1.25	-	-	-	0	-
SPT-CL J2326−5949	351.7325	−59.8215	4.09	0.25	-	-	-	0	-
SPT-CL J2327−5137	351.7831	−51.6244	5.03	1.00	0.36±0.01	$2.78^{+0.48}_{-0.57}$	50±7	0	-
SPT-CL J2327−6225	351.9144	−62.4196	6.11	0.75	0.190±0.007	$3.39^{+0.52}_{-0.61}$	56±8	0	LOS
SPT-CL J2327−5800	351.9221	−58.0158	4.15	0.75	-	-	-	0	-
SPT-CL J2328−5456	352.0115	−54.9349	4.47	0.25	1.02±0.06	$2.04^{+0.34}_{-0.45}$	19±3	1	-
SPT-CL J2328−5533	352.1774	−55.5602	8.84	0.25	0.81±0.02	$3.59^{+0.44}_{-0.55}$	49±7	0	-
SPT-CL J2329−5630	352.2591	−56.5072	4.14	1.00	1.09±0.04	$1.91^{+0.30}_{-0.42}$	27±6	0	-
SPT-CL J2329−5849	352.2920	−58.8313	4.15	0.75	-	-	-	0	-
SPT-CL J2329−5230	352.3115	−52.5014	4.32	0.25	0.70±0.02	$2.25^{+0.36}_{-0.49}$	45±8	0	-
SPT-CL J2329−5831	352.4743	−58.5267	11.75	0.25	0.80±0.02	$4.32^{+0.50}_{-0.61}$	80±10	0	LOS
SPT-CL J2329−5958	352.4795	−59.9741	4.11	1.25	-	-	-	0	-
SPT-CL J2329−5030	352.4943	−50.5052	5.12	0.25	-	-	-	0	-
SPT-CL J2330−5035	352.6022	−50.5884	4.21	0.25	1.07±0.06	$1.94^{+0.30}_{-0.43}$	22±4	1	LOS
SPT-CL J2330−5129	352.6727	−51.4974	4.19	0.25	0.55±0.02	$2.31^{+0.37}_{-0.51}$	33±7	0	-
SPT-CL J2331−5737	352.8963	−57.6175	7.65	0.50	1.57±0.08	$2.53^{+0.33}_{-0.39}$	20±3	1	LOS
SPT-CL J2331−5131	352.9506	−51.5182	4.28	0.50	-	-	-	0	-
SPT-CL J2331−5052	352.9713	−50.8707	19.91	0.50	0.576	$6.42^{+0.68}_{-0.84}$	126±12	0	-
SPT-CL J2332−5358	353.1092	−53.9761	18.08	1.25	0.402	$6.43^{+0.70}_{-0.83}$	83±10	0	-
SPT-CL J2332−5220	353.1376	−52.3389	4.23	0.75	0.45±0.01	$2.42^{+0.38}_{-0.54}$	46±7	0	LOS
SPT-CL J2332−6112	353.1431	−61.2127	5.12	0.25	1.04±0.06	$2.21^{+0.39}_{-0.46}$	35±4	1	-
SPT-CL J2333−6501	353.4703	−65.0234	7.35	0.25	0.57±0.02	$3.44^{+0.44}_{-0.56}$	54±8	0	-
SPT-CL J2334−5308	353.5206	−53.1403	5.20	0.25	1.17±0.07	$2.14^{+0.37}_{-0.44}$	39±4	1	-

Bleem et al.

Table 1 — *Continued*

SPT ID	R.A. (J2000)	Decl. (J2000)	Best ξ	θ_c	Redshift	M_{500c} $(10^{14}h_{70}^{-1}M_\odot)$	λ	*Spitzer*	Notes
SPT-CL J2334−5131	353.5897	−51.5236	4.18	0.25	0.68±0.02	$2.22^{+0.35}_{-0.48}$	39±7	0	-
SPT-CL J2334−5939	353.6880	−59.6503	6.70	0.25	0.39±0.01	$3.42^{+0.48}_{-0.58}$	32±6	0	-
SPT-CL J2335−6135	353.7724	−61.5859	4.24	0.75	0.35±0.01	$2.50^{+0.41}_{-0.54}$	39±6	0	-
SPT-CL J2335−5434	353.8726	−54.5789	5.27	0.25	1.03±0.04	$2.27^{+0.40}_{-0.45}$	28±6	0	-
SPT-CL J2336−5352	354.0267	−53.8779	6.05	0.25	0.51±0.01	$3.04^{+0.46}_{-0.54}$	67±9	0	-
SPT-CL J2336−5252	354.0842	−52.8714	5.88	0.25	1.24±0.07	$2.30^{+0.38}_{-0.43}$	22±3	1	-
SPT-CL J2337−5942	354.3517	−59.7066	40.30	0.25	0.775	$8.98^{+0.96}_{-1.12}$	165±14	0	-
SPT-CL J2337−5912	354.3998	−59.2052	5.79	0.75	0.60±0.02	$2.85^{+0.46}_{-0.52}$	49±7	0	-
SPT-CL J2338−6246	354.5253	−62.7783	5.26	0.25	1.13±0.06	$2.19^{+0.39}_{-0.44}$	25±4	1	-
SPT-CL J2338−6527	354.5501	−65.4620	4.28	1.00	-	-	-	0	-
SPT-CL J2338−6311	354.6854	−63.1970	4.10	0.25	0.73±0.03	$2.15^{+0.34}_{-0.47}$	31±6	0	LOS
SPT-CL J2339−5550	354.8613	−55.8347	5.08	0.25	0.39±0.01	$2.76^{+0.46}_{-0.58}$	37±6	0	-
SPT-CL J2339−5008	354.9460	−50.1387	4.56	0.50	0.98±0.04	$2.09^{+0.36}_{-0.46}$	22±6	0	-
SPT-CL J2339−6332	354.9715	−63.5348	7.18	0.25	0.71±0.02	$3.21^{+0.45}_{-0.53}$	70±9	0	-
SPT-CL J2340−5719	355.0673	−57.3314	4.05	0.25	0.82±0.03	$2.07^{+0.32}_{-0.46}$	20±6	0	-
SPT-CL J2340−5251	355.1293	−52.8618	4.02	0.25	1.60±0.08	$1.58^{+0.24}_{-0.34}$	14±3	1	LL
SPT-CL J2340−6045	355.2486	−60.7505	4.12	0.75	0.50±0.02	$2.35^{+0.38}_{-0.51}$	22±5	0	-
SPT-CL J2341−5716	355.2636	−57.2719	5.95	1.00	0.44±0.01	$3.07^{+0.49}_{-0.56}$	60±8	0	LOS
SPT-CL J2341−5141	355.2955	−51.6939	4.63	0.25	-	-	-	0	-
SPT-CL J2341−5119	355.3000	−51.3306	20.01	0.25	1.003	$5.57^{+0.61}_{-0.73}$	51±0	0	-
SPT-CL J2341−5221	355.3005	−52.3619	4.09	0.25	0.83±0.04	$2.09^{+0.32}_{-0.46}$	18±5	0	-
SPT-CL J2341−5724	355.3506	−57.4156	14.32	0.50	1.259	$4.18^{+0.47}_{-0.57}$	53±0	0	-
SPT-CL J2341−5639	355.4417	−56.6655	4.08	0.75	0.48±0.02	$2.36^{+0.37}_{-0.51}$	38±6	0	RC
SPT-CL J2341−5138	355.4460	−51.6389	4.71	0.25	0.55±0.02	$2.49^{+0.44}_{-0.54}$	36±6	0	-
SPT-CL J2341−5308	355.4778	−53.1371	5.34	0.75	0.54±0.01	$2.74^{+0.46}_{-0.54}$	59±8	0	RC
SPT-CL J2342−6030	355.5051	−60.5084	4.66	0.25	0.82±0.03	$2.24^{+0.39}_{-0.49}$	25±6	0	-
SPT-CL J2342−5621	355.6175	−56.3593	4.11	1.00	0.42±0.01	$2.40^{+0.39}_{-0.53}$	44±7	0	-
SPT-CL J2342−5715	355.6404	−57.2509	5.49	0.50	0.83±0.03	$2.52^{+0.43}_{-0.48}$	27±6	0	-
SPT-CL J2342−6041	355.6921	−60.6995	5.10	0.25	0.80±0.03	$2.42^{+0.41}_{-0.49}$	31±7	0	-
SPT-CL J2342−5411	355.6928	−54.1864	12.54	0.25	1.075	$4.12^{+0.45}_{-0.57}$	32±0	0	-
SPT-CL J2342−5522	355.7060	−55.3771	4.58	2.50	-	-	-	0	-
SPT-CL J2343−5158	355.8285	−51.9801	4.22	0.50	-	-	-	0	-
SPT-CL J2343−5023	355.8355	−50.3999	6.43	0.25	0.89±0.03	$2.78^{+0.44}_{-0.49}$	36±7	0	-
SPT-CL J2344−6251	356.0183	−62.8611	4.09	0.25	1.49±0.07	$1.65^{+0.25}_{-0.36}$	27±6	0	-
SPT-CL J2344−6000	356.0720	−60.0131	4.10	0.25	0.50±0.01	$2.34^{+0.37}_{-0.51}$	50±7	0	-
SPT-CL J2344−5656	356.0758	−56.9349	4.06	0.50	1.60±0.08	$1.58^{+0.23}_{-0.34}$	13±3	1	LOS,LL
SPT-CL J2344−5233	356.0879	−52.5562	4.12	1.25	-	-	-	0	-
SPT-CL J2344−6004	356.2391	−60.0740	4.58	0.25	1.31±0.07	$1.86^{+0.31}_{-0.41}$	16±5	0	-
SPT-CL J2345−6405	356.2500	−64.0991	20.43	0.25	1.01±0.02	$5.63^{+0.59}_{-0.72}$	97±11	0	LOS
SPT-CL J2345−6218	356.3397	−62.3035	4.52	1.75	-	-	-	0	-
SPT-CL J2346−5740	356.6714	−57.6774	4.72	0.25	1.17±0.07	$2.00^{+0.35}_{-0.44}$	23±3	1	LOS
SPT-CL J2347−6008	356.8653	−60.1489	4.03	0.50	-	-	-	0	-
SPT-CL J2347−5532	356.8878	−55.5455	4.24	0.25	0.37±0.02	$2.48^{+0.40}_{-0.54}$	22±5	0	-
SPT-CL J2347−6120	356.8988	−61.3361	4.19	0.50	0.50±0.02	$2.36^{+0.38}_{-0.52}$	27±6	0	-
SPT-CL J2347−5128	356.9049	−51.4828	4.84	0.75	0.55±0.02	$2.54^{+0.44}_{-0.53}$	20±5	0	-
SPT-CL J2347−6530	356.9071	−65.5137	4.53	0.25	-	-	-	0	-
SPT-CL J2347−5158	356.9431	−51.9802	4.23	0.25	0.84±0.03	$2.10^{+0.33}_{-0.46}$	38±7	0	-
SPT-CL J2348−5601	357.0260	−56.0316	4.18	0.50	0.42±0.01	$2.44^{+0.39}_{-0.54}$	39±7	0	-
SPT-CL J2348−5715	357.1200	−57.2629	4.40	0.25	0.60±0.02	$2.33^{+0.40}_{-0.51}$	28±6	0	LOS
SPT-CL J2349−5113	357.3861	−51.2285	5.60	0.75	0.42±0.01	$2.94^{+0.50}_{-0.57}$	58±9	0	LOS
SPT-CL J2349−6506	357.4426	−65.1067	4.77	0.25	0.57±0.02	$2.50^{+0.44}_{-0.52}$	35±6	0	-
SPT-CL J2349−5710	357.4939	−57.1692	4.66	0.50	0.51±0.02	$2.51^{+0.42}_{-0.54}$	19±5	0	-
SPT-CL J2350−5635	357.6085	−56.5973	4.79	0.25	1.33±0.07	$1.90^{+0.35}_{-0.42}$	13±3	1	-
SPT-CL J2350−5434	357.6180	−54.5812	4.11	0.25	0.55±0.02	$2.29^{+0.37}_{-0.51}$	27±5	0	-
SPT-CL J2350−5301	357.7247	−53.0222	11.42	0.50	0.54±0.01	$4.64^{+0.52}_{-0.66}$	68±9	0	-
SPT-CL J2351−5240	357.8173	−52.6769	4.36	0.25	-	-	-	0	-
SPT-CL J2351−5005	357.8295	−50.0952	5.03	0.25	0.56±0.02	$2.59^{+0.45}_{-0.54}$	22±6	0	LOS
SPT-CL J2351−5452	357.9053	−54.8827	12.33	0.50	0.384	$5.14^{+0.58}_{-0.71}$	102±10	0	RC
SPT-CL J2352−5755	358.1347	−57.9245	4.28	0.75	-	-	-	0	-
SPT-CL J2352−6122	358.1420	−61.3692	4.04	0.25	1.26±0.07	$1.77^{+0.27}_{-0.39}$	18±5	0	-

Table 1 — *Continued*

SPT ID	R.A. (J2000)	Decl. (J2000)	Best ξ	θ_c	Redshift	M_{500c} $(10^{14} h_{70}^{-1} M_\odot)$	λ	*Spitzer*	Notes
SPT-CL J2352−6134	358.1941	−61.5687	11.81	0.25	0.92±0.02	$4.18^{+0.48}_{-0.57}$	72±9	0	-
SPT-CL J2352−6249	358.2094	−62.8287	4.55	0.25	0.93±0.04	$2.11^{+0.37}_{-0.47}$	24±6	0	LOS
SPT-CL J2352−5251	358.2117	−52.8648	4.19	1.00	0.48±0.02	$2.38^{+0.40}_{-0.53}$	38±7	0	-
SPT-CL J2353−6517	358.3013	−65.2921	4.91	0.25	0.68±0.02	$2.43^{+0.43}_{-0.52}$	40±8	0	-
SPT-CL J2354−5106	358.5422	−51.1048	6.62	0.50	0.33±0.01	$3.46^{+0.50}_{-0.59}$	29±6	0	-
SPT-CL J2354−6518	358.5952	−65.3084	4.16	1.00	-	-	-	0	-
SPT-CL J2354−5633	358.7207	−56.5514	9.76	0.50	0.56±0.01	$4.18^{+0.50}_{-0.62}$	90±11	0	-
SPT-CL J2355−5156	358.8514	−51.9483	8.43	0.25	0.75±0.02	$3.55^{+0.44}_{-0.55}$	48±7	0	LOS
SPT-CL J2355−5029	358.8681	−50.4945	4.22	0.25	0.93±0.04	$2.05^{+0.31}_{-0.45}$	24±5	0	-
SPT-CL J2355−5515	358.8715	−55.2539	4.06	0.25	1.24±0.07	$1.79^{+0.28}_{-0.40}$	26±4	1	-
SPT-CL J2355−5259	358.9368	−52.9843	6.31	0.25	0.77±0.02	$2.87^{+0.45}_{-0.50}$	58±8	0	-
SPT-CL J2355−5055	358.9492	−50.9297	10.36	0.75	0.320	$4.70^{+0.54}_{-0.67}$	85±10	0	-
SPT-CL J2356−4957	359.0792	−49.9554	4.00	1.50	-	-	-	0	-
SPT-CL J2357−5421	359.2628	−54.3604	6.28	0.25	0.89±0.03	$2.74^{+0.45}_{-0.45}$	25±6	0	LOS
SPT-CL J2358−5229	359.5293	−52.4846	7.15	0.25	0.67±0.01	$3.25^{+0.45}_{-0.53}$	79±9	0	LOS
SPT-CL J2358−6129	359.7146	−61.4950	11.97	0.50	0.405±0.010	$5.00^{+0.59}_{-0.70}$	67±8	0	-
SPT-CL J2359−5023	359.7829	−50.3958	4.26	0.50	1.33±0.07	$1.78^{+0.29}_{-0.40}$	11±3	1	-
SPT-CL J2359−5010	359.9318	−50.1703	10.86	0.50	0.775	$4.14^{+0.50}_{-0.60}$	72±9	0	-

Note. — Galaxy cluster candidates detected at $\xi > 4$ in the SPTpol 500d survey. We first report properties derived solely from the SPT data, namely the candidate names, positions, detection-significances (ξ) and corresponding β-model core-radii at which the candidates were detected. Next, using the optical/IR confirmation processes discussed in Section 5, we provide redshifts of associated galaxy counterparts to the SZ detections for systems with $f_{\rm cont} < 0.2$. These redshifts are combined with the ξ values to estimate cluster masses (Section 6) for systems with optical/IR contamination fractions such that the overall sample is expected to be 94% pure. We provide the optical richness (λ) and mark whether these quantities were derived with our MCMF or *Spitzer* analysis. Finally we flag **LL** confirmed clusters with redshift lower-limits of $z = 1.6$ (see Section 5.2), **RC** clusters in which potentially $\Delta\xi > 2$ is filled in by synchrotron emission (see Section 7) or **LOS** for which a secondary optical structure along the line-of-sight met our confirmation criteria. The richnesses, redshifts, and contamination fractions of both primary and secondary systems are reported in the online version of the cluster sample. We also provide in the online file information on line-of-sight structures for unconfirmed clusters.

This paper was built using the Open Journal of Astrophysics LaTeX template. The OJA is a journal which provides fast and easy peer review for new papers in the astro-ph section of the arXiv, making the reviewing process simpler for authors and referees alike. Learn more at http://astro.theoj.org.